

Some pages of this thesis may have been removed for copyright restrictions.

If you have discovered material in Aston Research Explorer which is unlawful e.g. breaches copyright, (either yours or that of a third party) or any other law, including but not limited to those relating to patent, trademark, confidentiality, data protection, obscenity, defamation, libel, then please read our [Takedown policy](#) and contact the service immediately (openaccess@aston.ac.uk)



Low dimensional carbon enhanced semiconductor nanomaterials for photocatalytic applications

Kassam Iqbal Ahmed

Doctor of Philosophy

Aston University

October 2019

Kassam Iqbal Ahmed asserts his moral right to be identified as the author of this thesis. This copy of the thesis has been supplied on condition that anyone who consults it is understood to recognise that its copyright belongs to its author and that no quotation from the thesis and no information derived from it may be published without appropriate permission or acknowledgement.

Aston University

Low dimensional carbon enhanced semiconductor nanomaterials for
photocatalytic applications

Kassam Iqbal Ahmed

Doctor of Philosophy

October 2019

Summary

The environmental consequences of burning fossil fuels and the global demand for energy has generated interest in renewable and clean energy sources. Solar water splitting to produce hydrogen using semiconductors is an attractive process as no emissions are generated, using water and sunlight only.

Low dimensional carbon nanostructures unique structural, optical and electronic properties have led to more research in photocatalysis. TiO_2 has a high band gap of 3.2 eV resulting in strong absorbance in the UV region of the electromagnetic spectrum but constitutes only 4% of the solar spectrum. Initially, there was research in synthesising 0D carbon quantum dots to improve visible light activity in TiO_2 -A NF/CQDs. However, UV-Vis Spectroscopy showed absorbance of CQDs below 435 nm, which illustrated minimal absorbance in the visible light region.

Nanocomposites provide more efficient separation of electron-hole pairs as it is difficult for a single semiconductor to obtain a narrow band gap for absorbing photons in visible light and appropriate band positions for efficient charge transfer. The photocurrent response in C-NW/ TiO_2 NF/ Cu_2O showed a sharp increase compared to bare TiO_2 and Cu_2O , which indicated higher interparticle charge transfer between 1D TiO_2 NF and Cu_2O nanocubes. Carbon nanowires were used as a short electron pathway between both semiconductors, as suggested by the proposed schematic.

Cu_2O has favourable band energy positions for water splitting but is prone to photocorrosion as reduction and oxidation potentials of Cu_2O lie within the band gap. Thus, rGO is used as a versatile catalyst support because it has a high surface area, electron mobility and rGO surfaces have a variety of oxygen functionalities. The synthesised $\text{Cu}_2\text{O}/\text{rGO}$ offered higher photocatalytic activity ($31 \mu\text{mol.g}^{-1}.\text{h}^{-1}$) and rate of 4-chlorophenol decomposition (95% after 60 minutes) than previous reports.

H_2 evolution using BiVO_4 has not been consistently reported in literature because the conduction band (CB) position of BiVO_4 is near the reduction potential of water. QD- BiVO_4/rGO exhibited higher photocatalytic activity than BiVO_4 and QD- BiVO_4 in visible light towards BPA photodecomposition and H_2 evolution, which was indicative of the nanocomposite's high surface area and enhanced light absorption. QD- BiVO_4/rGO has excellent photostability after testing in several photodecomposition and transient photocurrent cycles.

Keywords

Visible light photocatalysis, carbon nanowires, Cu_2O , graphene, BiVO_4 .

Acknowledgements

I would like to thank Dr Wei Li, my supervisor, for the continuous support and guidance over the last few years. Even though there were many hiccoughs along the way, he made sure I was steering along the right path. I would also like to thank my co-supervisor Professor Paul Topham for the countless talks and help alleviating any issues I had.

I am eternally grateful to Dr Karthik Sekar, who was the most helpful post-doc one could ask for. Your work ethic and drive to push is what makes you an inspiring researcher to all those around you, so I thank you for teaching me many aspects of research. I would also like to thank Khalid for listening whenever I knocked on the window; it was greatly appreciated.

The earlier parts of my research when I was active with ERA, I enjoyed my time with a lot of you guys – Aries, Catalonia, Barton, Joe and of course the cool guys from EBRI – Jorge, Tom, Mohammed and Filipe. I wanted to just say thank you for allowing me to share my troubles with you and just enjoying a good time together.

A huge mention must go out to the people in MB 111 and Michael, thank you so much for the fun experiences – Sainab, Kinana, Manuela, Sian, Helena, Paddy, George, Taylor, Sim, Christian and Jakob. It was an absolute blast, and I wish you guys the very best.

To my siblings; Sarah, Hannah and Haseeb, this would not be possible if it wouldn't have been you guys continuously listening to my troubles whenever I was stressed out.

Finally, to my Jannat-al-Firdos, my Mother. I would like to say thank you for pushing me continuously, without your sacrifices I would not have written this.

Publications

1. Sekar, K.; Ahmed, K.; Lee, A.; Wilson, K.; Sasaki, K.; Li, W. Pompon Dahlia-like $\text{Cu}_2\text{O}/\text{rGO}$ nanostructures for visible light photocatalytic H_2 production and 4-chlorophenol degradation. *ChemCatChem*. **2020**, *12*.
2. Ahmed, K.; Sekar, K.; Li, W. Carbon nanowires enhanced $\text{TiO}_2/\text{Cu}_2\text{O}$ nanocomposite for photoelectrochemical water splitting. Manuscript in preparation for *ACS Appl. Mat. & Interfaces*.
3. Sekar, K.; Ahmed, K.; Lee, A.; Wilson, K.; Sasaki, K.; Li, W. BiVO_4/rGO visible-light photocatalyst for hydrogen evolution and bisphenol A degradation. Manuscript in preparation for *ChemCatChem*.

Contents

Acknowledgements.....	3
Publications.....	4
Contents.....	5
List of figures.....	9
List of tables.....	12
List of abbreviations.....	13
Chapter 1 Introduction.....	15
1.1. Photocatalysis.....	18
1.1.1. Photocatalytic water splitting.....	19
1.1.2. Photoelectrochemistry.....	21
1.1.3. Photocatalyst requirements.....	23
1.1.4. Photodecomposition of pollutants.....	25
1.2. Low dimensional carbon materials.....	26
1.2.1. Zero-dimensional carbon.....	27
1.2.2. One-dimensional carbon.....	31
1.2.3. Two-dimensional carbon.....	34
1.3. Thesis outline.....	37
1.4. References.....	39
Chapter 2 Methodology.....	42
2.1. Characterisation methods.....	42
2.1.1. X-ray Diffraction (XRD).....	42
2.1.2. X-ray Photoelectron Spectroscopy (XPS).....	44
2.1.3. Brunauer-Emmett-Teller (BET) analysis.....	45
2.1.4. Diffuse Reflectance UV-Visible Spectroscopy (DRUVS).....	46
2.1.5. Thermogravimetric Analysis (TGA).....	47
2.1.6. Gas Chromatography (GC).....	47
2.1.7. Scanning Electron Microscopy (SEM).....	48
2.1.8. Transmission Electron Microscopy (TEM).....	49
2.1.9. Raman Spectroscopy.....	50
2.2. Photoelectrochemical analysis.....	51
2.2.1. PEC measurements.....	52

2.2.2.	Electrochemical Impedance Spectroscopy (EIS).....	53
2.3.	Reactor setup.....	55
2.3.1.	Photodecomposition of pollutants.....	55
2.3.2.	Hydrogen evolution	56
2.3.3.	Photoelectrochemical cell (PEC).....	57
2.4.	Apparent Quantum Efficiency (AQE).....	58
2.5.	References.....	60
Chapter 3	Zero-dimensional carbon enhanced visible light activity of TiO ₂	61
3.1.	Introduction.....	61
3.2.	Catalyst synthesis	62
3.2.1.	TiO ₂ -A nanofibers (NF).....	62
3.2.2.	TiO ₂ -B nanofibers (NF).....	63
3.2.3.	TiO ₂ -B microparticles (MP).....	63
3.2.4.	TiO ₂ /CQDs.....	64
3.3.	Characterisation.....	64
3.3.1.	TiO ₂ -A NF.....	64
3.3.2.	TiO ₂ -B NF.....	65
3.3.3.	TiO ₂ -B MP	67
3.3.4.	General characterisation.....	68
3.4.	Photodecomposition of methylene blue dye	70
3.4.1.	TiO ₂ -A nanoparticles (NP).....	70
3.4.2.	TiO ₂ -A NF.....	71
3.4.3.	TiO ₂ -B NF.....	72
3.4.4.	TiO ₂ -B MP	73
3.4.5.	Carbon loading	74
3.5.	Transient photocurrent analysis.....	75
3.5.1.	TiO ₂ -A NP.....	75
3.5.2.	TiO ₂ -A NF.....	76
3.5.3.	TiO ₂ -B NF.....	77
3.5.4.	TiO ₂ -B MP	78
3.5.5.	Carbon loading	79
3.6.	Conclusions.....	80
3.7.	References.....	82
Chapter 4	One-dimensional carbon enhanced interparticle charge transfer of TiO ₂	83

4.1.	Introduction.....	83
4.2.	Catalyst Synthesis.....	85
4.2.1.	C-NW/TiO ₂ NF.....	85
4.2.2.	C-NW/TiO ₂ NF/Cu ₂ O	85
4.3.	Characterisation.....	86
4.3.1.	Microscopy studies	86
4.3.2.	Photophysical properties	88
4.4.	Photoelectrochemical analysis	92
4.5.	Conclusions.....	98
4.6.	References.....	99
Chapter 5 Two-dimensional carbon enhanced chemical stability of Cu ₂ O.....		101
5.1.	Introduction.....	101
5.2.	Catalyst synthesis	102
5.3.	Characterisation.....	103
5.3.1.	Microscopy studies	103
5.3.2.	Photophysical properties	105
5.3.3.	XPS analysis.....	107
5.4.	Hydrogen evolution.....	111
5.5.	Photodecomposition of 4-chlorophenol.....	113
5.5.1.	Photocatalytic stability.....	114
5.6.	Photoelectrochemical analysis	115
5.6.1.	Photoelectrochemical stability.....	117
5.7.	Conclusions.....	118
5.8.	References.....	119
Chapter 6 Two-dimensional carbon enhanced structural stability of BiVO ₄		121
6.1.	Introduction.....	121
6.2.	Catalyst synthesis	122
6.3.	Characterisation.....	123
6.3.1.	Microscopy studies	123
6.3.2.	Photophysical properties	125
6.3.3.	XPS analysis.....	128
6.4.	Hydrogen evolution.....	130
6.5.	Photodecomposition of Bisphenol A.....	132
6.5.1.	Photocatalytic stability.....	134

6.6.	Photoelectrochemical analysis	135
6.6.1.	Photoelectrochemical stability.....	137
6.7.	Conclusions.....	138
6.8.	References.....	140
Chapter 7	Conclusions and future work.....	142
7.1.	Conclusions.....	142
7.2.	Future work.....	144

List of figures

Figure 1.1 Principles of photocatalytic water splitting.....	19
Figure 1.2 The main processes in photocatalytic water splitting, adapted from reference ²⁴	21
Figure 1.3 PEC system for photoelectrochemistry with an applied bias, adapted from reference ²⁶	22
Figure 1.4 Band bending in a semiconductor-electrolyte interface after equilibrium.....	23
Figure 1.5 Conduction and valence band edges of semiconductors in an electrolyte at pH = 0, retrieved from reference ²⁸	24
Figure 1.6 Schematic of the photodecomposition of organic pollutants, retrieved from reference ³⁶	26
Figure 1.7 Different dimensional carbon nanostructures retrieved from reference ³⁸	27
Figure 1.8 Upconverted PL properties of CQDs, retrieved from reference ⁴¹	28
Figure 1.9 Proposed mechanism for TiO ₂ /CQDs under visible light, retrieved from reference ⁴¹	29
Figure 1.10 More recent mechanism of CQDs in TiO ₂ /CQD hybrid nanomaterial, retrieved from reference ²⁶	30
Figure 1.11 Conceptual idea of SWNTs by folding graphene sheet along lattice vectors, retrieved from reference ⁵³	32
Figure 1.12 3D CAD rendering of graphene layers stacked as cups in a CNF, inset including TEM of orientation of graphene layers along the structure, retrieved from reference ⁵⁸	33
Figure 1.13 Charge transfer in a carbon nanotube hybrid electrode, retrieved from reference ⁶¹	34
Figure 1.14 GO sheet improves exciton separation and electron transport, retrieved from reference ⁶⁷	35
Figure 1.15 Schematic of rGO extracting photogenerated electron from Cu ₂ O, retrieved from reference ⁷²	36
Figure 2.1 Schematic demonstration of Bragg's law.	43
Figure 2.2 Mechanism of energy transfer from x-ray photon irradiation to core level electrons in XPS.	44
Figure 2.3 Diagram of the vibrational modes with Rayleigh, Stokes and Anti-stokes Raman scattering in a system.	51
Figure 2.4 Chopped illumination of chronoamperometric measurement, where i_0 is the initial photoexcitation current and i_e is the photocurrent at equilibrium. (A) is an ideal photocurrent response, (B) requires exponential decay over time, (C) requires time to reach equilibrium.	52
Figure 2.5 Picture of the reactor vessel used for photodecomposition of pollutants.	56
Figure 2.6 Picture of the PEC cell, where RE is Hg/Hg ₂ SO ₄ , WE is the photocatalyst drop casted onto glassy carbon electrode, CE is Platinum wire and the light source is 200 W Hg-Xe lamp.	58
Figure 3.1 Structure of CQDs, retrieved from reference ¹²	62
Figure 3.2 SEM images of TiO ₂ -A NF.	64
Figure 3.3 XRD pattern of TiO ₂ -A NF.	65

Figure 3.4 SEM images of TiO ₂ -B NF.....	66
Figure 3.5 XRD pattern of TiO ₂ -B NF.....	66
Figure 3.6 SEM images of TiO ₂ -B MP.....	67
Figure 3.7 XRD pattern of TiO ₂ -B MP.....	67
Figure 3.8 Raman spectra of TiO ₂ -Anatase NF, TiO ₂ -B NF and TiO ₂ -B MP.....	68
Figure 3.9 Thermogravimetric analysis (TGA) of TiO ₂ -A NF/CQDs.....	69
Figure 3.10 UV-Vis spectra of carbon quantum dots (CQDs).	69
Figure 3.11 Photodecomposition of MB dye using TiO ₂ -A NP.....	71
Figure 3.12 Photodecomposition of MB dye using TiO ₂ -A NF.....	72
Figure 3.13 Photodecomposition of MB dye using TiO ₂ -B NF.....	73
Figure 3.14 Photodecomposition of MB dye using TiO ₂ -B MP.....	74
Figure 3.15 Visible light photodecomposition of MB dye using different carbon loading.	75
Figure 3.16 Transient photocurrent of TiO ₂ -A NP at 0 V vs. RHE.....	76
Figure 3.17 Transient photocurrent of TiO ₂ -A NF at 0 V vs. RHE.....	77
Figure 3.18 Transient photocurrent of TiO ₂ -B NF at 0 V vs. RHE.....	78
Figure 3.19 Transient photocurrent of TiO ₂ -B MP at 0 V vs. RHE.....	79
Figure 3.20 Visible light transient photocurrent with different carbon loading at 0 V vs. RHE.....	80
Figure 4.1 TEM images of (a) TiO ₂ NF, (b) Cu ₂ O nanocubes, (c) C-NW/TiO ₂ NF/Cu ₂ O, (d) C-NWs.....	86
Figure 4.2 SEM image of C-NW/TiO ₂ NF/Cu ₂ O.....	87
Figure 5.1 Schematic of the synthesis procedure of Pompom Dahlia Cu ₂ O/rGO.....	103
Figure 5.2 (a-d) TEM images of Pompom Dahlia hierarchical Cu ₂ O. Insets of (a) and (b) show particle size distribution of aggregated Cu ₂ O and individual Cu ₂ O nanospheres. Insets of (c) show the SEM image of aggregates.....	104
Figure 5.3 TEM images of Cu ₂ O/rGO. Insets of (a) and (c) show particle size distribution of aggregates and individual Cu ₂ O particles respectively, (b) SEM image and (d) HRTEM image of aggregates.....	105
Figure 5.4 (a) XRD patterns, (b) DRUV spectra and (c) Tauc plots, and (d) N ₂ adsorption- desorption isotherms of Pompom Dahlia-like hierarchical Cu ₂ O and Cu ₂ O/rGO nanocomposite.....	107
Figure 5.5 (a) Cu 2p and (b) corresponding C 1s XP spectra of Pompom Dahlia-like hierarchical Cu ₂ O and Cu ₂ O/rGO nanocomposite.....	108
Figure 5.6 O 1s XP spectra of Pompom Dahlia-like hierarchical Cu ₂ O and Cu ₂ O/rGO nanocomposite.....	109
Figure 5.7 Valence band XPS of Pompom Dahlia-like hierarchical Cu ₂ O and Cu ₂ O/rGO nanocomposite.....	110
Figure 5.8 Visible light photocatalytic H ₂ production over Pompom Dahlia-like hierarchical Cu ₂ O and Cu ₂ O/rGO nanocomposite with (a) 1 vol.% and (b) 10 vol.% methanol (in water) as a sacrificial hole scavenger. Reaction conditions: 0.02 g catalyst, 200 W Hg-Xe ($\lambda > 420$ nm).....	112
Figure 5.9 Visible light photocatalytic 4-CP degradation over Pompom Dahlia-like hierarchical Cu ₂ O and Cu ₂ O/rGO nanocomposite. (a) initial rates of 4-CP removal and (b) corresponding apparent quantum efficiencies after 15 minutes reaction; and (c) 4-CP removal efficiency.....	113

Figure 5.10 Recycles during visible light photocatalytic 4-CP degradation using a) Pompom Dahlia-like hierarchical Cu ₂ O/rGO nanocomposite and b) Cu ₂ O.....	114
Figure 5.11 (a) Transient photocurrent, (b) EIS (Nyquist) plot at 0 V vs. RHE under illumination, (c) Mott-Schottky plot of Cu ₂ O and Cu ₂ O/rGO using 200 W Hg-Xe arc lamp, 0.5 M Na ₂ SO ₄ electrolyte, (d) proposed charge transfer schematic mechanism of Cu ₂ O/rGO.....	117
Figure 5.12 Photoelectrochemical stability of Cu ₂ O and Cu ₂ O/rGO at 1 V vs. RHE with chopped illumination cycles of 20 minutes.	118
Figure 6.1 TEM images of QD-BiVO ₄ /rGO at various magnifications and (b,e) insets corresponding to particle size distributions.	123
Figure 6.2 a-b) TEM images of BiVO ₄ , c) TEM image of QD-BiVO ₄ , d) corresponding particles size distributions.	124
Figure 6.3 a) XRD pattern, b) N ₂ adsorption-desorption isotherm of synthesised BiVO ₄ , QD-BiVO ₄ and QD-BiVO ₄ /rGO.....	125
Figure 6.4 (a) DRUVS Absorption spectra, (b-d) corresponding Tauc plot of BiVO ₄ and QD-BiVO ₄ with QD-BiVO ₄ /rGO.	126
Figure 6.5 (a) DRUVS Tauc plot, (b) valence band XPS of BiVO ₄ , QD-BiVO ₄ and QD-BiVO ₄ /rGO.....	127
Figure 6.6 (a) Bi4f XPS, (b) V2p XPS offset for clarity.....	128
Figure 6.7 Core-level C 1s XPS of BiVO ₄ and QD-BiVO ₄ with QD-BiVO ₄ /rGO.....	129
Figure 6.8 Schematic band positions of BiVO ₄ , QD-BiVO ₄ and QD-BiVO ₄ /rGO.....	130
Figure 6.9 Photocatalytic hydrogen evolution under visible light over BiVO ₄ , QD-BiVO ₄ and QD-BiVO ₄ /rGO (experimental conditions: 50 mg of catalyst with pure water containing 50 ml of 0.5 M Na ₂ SO ₃ (hole scavenger) under visible irradiation by a 200 W Hg-Xe arc lamp.	131
Figure 6.10 (a) Initial rates of Bisphenol A removal, and (b) surface area normalised initial rates of BPA removal over BiVO ₄ , QD-BiVO ₄ and QD-BiVO ₄ /rGO (Experimental conditions: 50 ml BPA of 4.2 ×10 ⁻² mM, 20 mg catalyst, 200 W Hg-Xe arc lamp with UV cut-off filter).	132
Figure 6.11 Recycles during visible light MB dye degradation over a) BiVO ₄ /rGO nanocomposite and b) BiVO ₄	135
Figure 6.12 (a) Transient photocurrent, (b) Electrochemical Impedance Spectroscopy (EIS) of BiVO ₄ , QD-BiVO ₄ , QD-BiVO ₄ /rGO using 200 W Hg-Xe arc lamp and 0.5 M Na ₂ SO ₄ electrolyte under visible light illumination ($\lambda > 420$ nm).....	136
Figure 6.13 Mott Schottky plot of BiVO ₄ and QD-BiVO ₄ with QD-BiVO ₄ /rGO.....	137
Figure 6.14 Photoelectrochemical stability of BiVO ₄ and QD-BiVO ₄ /rGO at 1 V vs. RHE with chopped illumination cycles of 20 minutes.	138

List of tables

Table 1.1 Potential power output of renewable technologies. Adapted from reference ⁹ .	16
Table 1.2 Energy properties of fuels retrieved from reference ¹⁸ .	17
Table 4.1 Photophysical properties of TiO ₂ NF, Cu ₂ O, TiO ₂ NF/Cu ₂ O and C-NW/TiO ₂ NF/Cu ₂ O.	91
Table 5.1 Fitted C 2p XP spectra of Pompom Dahlia-like hierarchical Cu ₂ O and Cu ₂ O/rGO nanocomposite.	108
Table 5.2 Fitted C 1s XP spectra of Pompom Dahlia-like hierarchical Cu ₂ O and Cu ₂ O/rGO nanocomposite.	109
Table 5.3 Photophysical properties of Pompom Dahlia-like hierarchical Cu ₂ O and Cu ₂ O/rGO nanocomposite.	110
Table 5.4 Visible light photocatalytic hydrogen evolution of Cu ₂ O photocatalysts.	112
Table 6.1 Physicochemical properties of BiVO ₄ , QD-BiVO ₄ and QD-BiVO ₄ /rGO.	129
Table 6.2 Photocatalytic pollutant decomposition using nanostructured BiVO ₄ photocatalysts under visible light irradiation.	133

List of abbreviations

Acronyms

0D	Zero dimensional
1D	One dimensional
2D	Two dimensional
AC	Alternate current
AQE	Apparent quantum efficiency
BET	Brunauer, Emmett and Teller
BPA	Bisphenol A
CB	Conduction band
CNF	Carbon nanofibers
CNT	Carbon nanotubes
C-NW	Carbon nanowires
CQD	Carbon quantum dots
CVD	Chemical vapour deposition
DC	Direct current
DSSC	Dye sensitised solar cells
e ⁻	Electron
EIS	Electrochemical Impedance Spectroscopy
G	Gelatine
GC	Gas Chromatography
h ⁺	Hole
MB	Methylene Blue
MO	Methyl Orange
MWNT	Multi Wall Nano Tubes
NHE	Normal Hydrogen Electrode
NP	Nano Particles
OPV	Organic Photo Voltaic
PEC	Photo Electrochemical Cell
PL	Photo Luminescence
RHE	Reversible Hydrogen Electrode
SEM	Scanning Electron Microscopy
SWNT	Single Wall Nano Tube
TEM	Transmission Electron Microscopy
TGA	Thermo Gravimetric Analysis
TW	Tera Watts
UV	Ultra Violet
VB	Valence Band
VC	Vitamin C
XRD	X-Ray Diffraction
XPS	X-ray Photoelectron Spectroscopy

Symbols

a	Mass of the adsorbent
α	absorption coefficient
β	Line broadening at half maximum intensity
c	Capacitance (F)
c_B	BET constant
C	Proportionality constant
d	atomic spacing
E_B	Binding energy of the electron
E_{BG}	Band gap (eV)
e	electron charge (C)
ε	Permittivity of free space (F/m)
ε_0	Dielectric constant
E_{fb}	Flat-band potential (V)
$E\gamma$	Energy of the x-ray photon
$E_{Hg_2SO_4}$	Potential versus Hg/Hg ₂ SO ₄
$E^0_{Hg_2SO_4}$	Standard potential versus Hg/Hg ₂ SO ₄
E_K	Kinetic energy
E_{RHE}	Potential versus RHE
h	Planck's constant
K	Scherrer constant
k_B	Boltzmann's constant
N	Avogadro's constant
N_A	Majority carrier density
N_E	Mole incident photons per unit time
N_P	Number of incident photons per unit time
ρ	partial vapour pressure (torr)
ρ_0	Saturation pressure
R	Reflectance
φ	Work function
s	Adsorption cross section of the adsorbent
τ	Mean crystallite size
θ	Angle
v	Volume of adsorbed gas
v_m	Volume of adsorbed gas to produce a monolayer
V	Applied potential
V_A	Molar volume of adsorbed gas

Chapter 1

Introduction

The earth receives enough solar energy from the sun in one hour to supply the global energy demand for a year¹. Concerns over global warming have led to an effort to minimise one of the major contributors, namely CO₂ emissions. Solar energy conversion technologies are emerging to combat global warming converting sunlight to energy using semiconductors. Semiconductors are important materials used in light-harvesting technologies, as they can absorb sunlight and convert it to energy which is either stored or used in applications such as solar water splitting or CO₂ reduction².

Since 1998, the United Nations framework convention decided to stabilise greenhouse gas emissions to tackle climate change. Their aims were to generate 10 TW (Tera Watts) of carbon-free power per year by 2050, which was equal to the total power demand in 1998³. In recent studies, the total power consumption is predicted to increase twice-fold to 35 TW by 2050. Using non-renewable sources such as fossil fuels to generate energy have proven to damage the environment, as CO₂ emissions were recorded as the highest on earth in over 400,000 years⁴.

Global agreements such as the Paris agreement⁵, Kyoto Protocol⁶ and Climate Change Act of 2008⁷ have motivated a change in future energy generation, with renewable energy a key contender as the leading energy source of the future. Renewable energy is projected as one of the most popular electricity generation sources by 2035, as it is anticipated to provide over 40% of global electricity demand⁸. Furthermore, the potential of renewable energy has been reviewed by investigating the power generation capacity of different technologies. These range from hydroelectric resources, geothermal activity on land, global wind power and solar power. Most renewable technologies have a potential power capacity of below 12 TW, however solar power has an overwhelming potential of 120,000 TW, as shown in Table 1.1. The potential power output of these technologies is relevant today, although, the solar power converted is currently less than 0.01% of the total power demand⁹.

Consequently, the energy industry in the UK has invested approximately £40 billion in low carbon electricity generation since 2010¹⁰ to meet the legally binding renewable energy target for 2020¹¹. As the country is aiming to minimise coal-based fuel by 2025, this is an

important opportunity for greener fuels, such as hydrogen, to make an impact in the UK energy sector¹². Emerging technologies which convert sunlight into electricity were commercialised over the last decade in the form of solar cells. Photovoltaic (PV) solar cells contribute 3.9% of total energy generation in the UK¹³, although the most successful commercialised technologies are crystalline silicon solar cells. Silicon solar PV cells operate at efficiencies above 25%¹⁴ but have expensive manufacturing conditions which are aided by government tariffs. Hence, this technology struggles to compete with other conventional energy sources, meaning research in other solar energy technologies is necessary.

Table 1.1 Potential power output of renewable technologies. Adapted from reference⁹.

Renewable energy	Potential power output (TW)
Hydro	0.5
Tidal and ocean currents	2
Geothermal	12
Wind	2-4
Solar	120,000

Alternative technologies such as dye sensitised solar cells (DSSCs) and organic photovoltaic cells (OPVs) are cheaper alternatives with efficiencies up to 12%¹⁵. However, slow progress in efficient solar PV systems and stability issues have proven that this method has scale-up difficulties into larger PV systems. These systems may have a prospect in smaller portable solar panels, such as watches and phone chargers where durability is not an important factor.

Another, and possibly more important, element to this conundrum is energy storage. This is especially significant for solar energy conversion because there is not a continuous supply of energy, so reliance on sunlight makes it impossible to generate electricity in the night. Thus, it is important to compare the electricity storage potential of different fuels. Ever since Fujishima and Honda studied water photolysis using TiO_2 in 1972¹⁶, photocatalytic water splitting has become an attractive means to convert solar energy into

hydrogen fuel¹⁷. Hydrogen should be an important fuel of the future, mainly because the only product from the combustion of hydrogen is water. This means that it has a carbon-free energy cycle, hence it will not contribute towards greenhouse gas emissions and global warming. Moreover, as shown in Table 1.2, hydrogen has lower density by volume, so the potential for energy storage is much greater than other fuels¹⁸.

Electrolysis of water (also called water splitting) is a well-researched procedure that requires high amount of energy (50 kW.h) to produce 1 kilogram of hydrogen. Thus, research in solar energy conversion is useful to overcome this huge energy requirement. There are three main methods to split water using solar energy. The first method uses photovoltaic cells to split water, which currently has high manufacturing costs, such as solar panels, inverter and batteries. Furthermore, using solar PV requires a lot of space so this method may have scale-up issues. The second method is called thermolysis, which thermally decomposes water at high temperatures and requires thermostable materials. This method is more efficient than electrolysis at ambient temperatures as most of the energy is supplied as heat (between 100 °C and 850°C)¹⁹, which is cheaper than electricity. The third method is called water photolysis, which is defined as the interaction of photogenerated charge carriers from a range of wavelengths in a semiconductor and enables water splitting through a potential bias. This method is cheaper than the previous two as the main manufacturing cost is the semiconductor, which is usually cheap.

Table 1.2 Energy properties of fuels retrieved from reference¹⁸.

Fuel	Density (g/l)	Lower heating value (MJ/kg)	Carbon percentage (%)
Crude oil	845	42.8	85
Natural gas	0.654	50.1	75
Petrol	737	43.7	85.5
Diesel	856	41.8	87
Hydrogen	0.0818	121	0

Initial reports of photoelectrochemical water splitting were demonstrated by Fujishima et al.¹⁶ using TiO₂ as the anode and Pt as the cathode under (ultraviolet) UV radiation which constitutes only 4% of incoming solar energy from the sun. Over the decades, much research has gone onto investigating visible light photocatalysts, as the visible light region consists of 46% of incoming solar energy from the sun. In addition, charge transfer kinetics and catalyst stability are essential factors in designing a feasible photocatalytic system. Hundreds of materials have been tested in photocatalysis, with a wide range of synthesis processes²⁰. Extensive studies have occurred using organic supports with semiconductors such as carbon-based nanomaterials in photocatalysis. Various types of carbon such as carbon quantum dots, carbon nanotubes and graphene have shown respective unique photoluminescence (PL) properties, ease and low-cost of manufacture, low toxicity and high chemical stability²¹.

Two types of photocatalyst systems were used to analyse the photocatalyst in the thesis. The first method tested the semiconductor activity by direct contact of the semiconductor in water and recorded hydrogen and oxygen evolution using gas chromatography. The second method used a photoelectrochemical cell with a potential bias (usually applied with a potentiostat) to drive photoelectrons around a circuit, creating a photocurrent. The photocurrent was recorded, and many semiconductor properties were analysed, such as stability and conductivity between semiconductor and electrolyte.

1.1. Photocatalysis

The definition of photocatalysis is the acceleration of a reaction using a catalyst under illumination. Semiconductors are used as catalysts in photocatalysis to absorb light because they possess a band gap which is the difference between the valence band and conduction band. This is elaborated in Section 1.1.2. The thesis will focus on three aspects of photocatalysis; photocatalytic water splitting, photoelectrochemistry and photodecomposition of pollutants.

The difference in terminology between “photoelectrochemistry” and “photocatalytic water splitting” must be stated for easier understanding throughout the thesis. “Photoelectrochemistry” uses an external bias to drive the reaction in a two or three-

electrode photoelectrochemical cell under irradiation. An electrode is fabricated for the photocatalyst as a photocathode or anode and is immersed in an electrolyte solution. “Photocatalytic water splitting” is used to describe direct contact between powdered photocatalyst and electrolyte solution under sunlight, forming a suspension with no external bias²². In this reaction, water splitting usually occurs on the surface of the photocatalyst.

1.1.1. Photocatalytic water splitting

Photocatalytic water splitting has drawn attention as it is an ideal solution to alleviate non-renewable resource depletion by generating hydrogen. Water splitting is an attractive process which converts solar energy into renewable hydrogen fuel¹. No external bias is used in photocatalytic water splitting, so particles act as both anode and cathode. This method analyses the photocatalytic activity of the semiconductor, as shown by hydrogen and oxygen evolution.

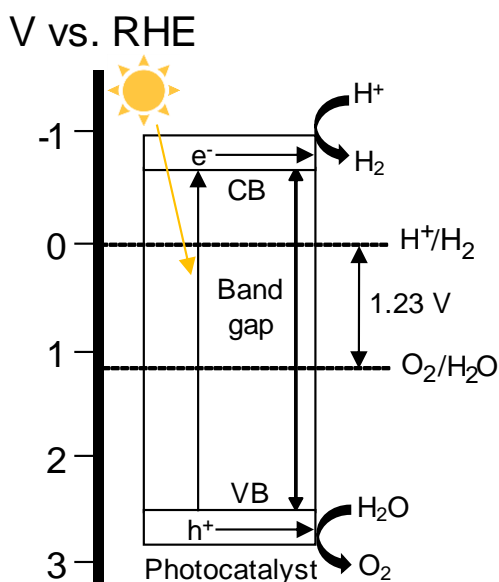
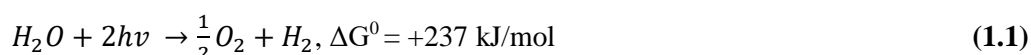


Figure 1.1 Principles of photocatalytic water splitting.

In water splitting, the semiconductor acts as the photocatalyst, as it absorbs photons from sunlight and electrons in the valence band (VB) are excited to the conduction band, if the photons have an energy greater than the band gap of the semiconductor. The band gap is the difference in energy between the top of the valence band and the bottom of the conduction band (CB), as shown in Figure 1.1. Therefore, the photons must have equal or more energy than the band gap energy to effectively excite the electrons in the VB. These photoexcited electrons are promoted from the top of the VB to the bottom of the CB, leaving behind a positive hole in the VB. The electrons in the CB and holes in the VB are driven into water reduction and oxidation reactions, producing hydrogen and oxygen respectively.

Thermodynamically, photocatalytic water splitting is an uphill reaction, which means the reaction is the standard Gibbs free energy change $\Delta G^0=237$ kJ/mol (or 1.23 eV) to occur, as shown in Equation 1.1.



The band gap and potentials of the CB and VB are important properties in the reduction and oxidation of H₂O by photogenerated electrons and holes. The bottom of the CB must be more negative than the reduction potential of H⁺/H₂ (0 V vs. RHE) and the top of the VB must be more positive than the oxidation potential of VB (1.23 V vs. RHE), as illustrated by the photocatalyst in Figure 1.1.

The charge generation and separation processes in the photocatalyst are important in photocatalytic water splitting. Initially, the photocatalyst absorbs light with energy greater or equal to the band gap energy, creating photogenerated electrons and holes. The two processes in the photocatalyst that affect the charge efficiency of the reaction are recombination and separation processes. Recombination of electrons and holes is a deactivation process on the surface or bulk of the photocatalyst, which reduces the photogenerated charges by emitting light²⁰. Therefore, efficient charge separation and migration to the surface, while avoiding recombination, is essential in photocatalytic water splitting.

The main processes for photocatalytic water splitting, as illustrated in Figure 1.2, occur in the following steps.

- A. Generation of photogenerated electrons (e^-) and holes (h^+) by light irradiation.
- B. Separation of photogenerated electrons (e^-) and holes (h^+) and their migration to the surface without recombination. Alternatively, the electron-hole pairs combine in bulk or on the surface.
- C. The reduction and oxidation of water by photogenerated electrons and holes to produce H_2 and O_2 respectively²³.

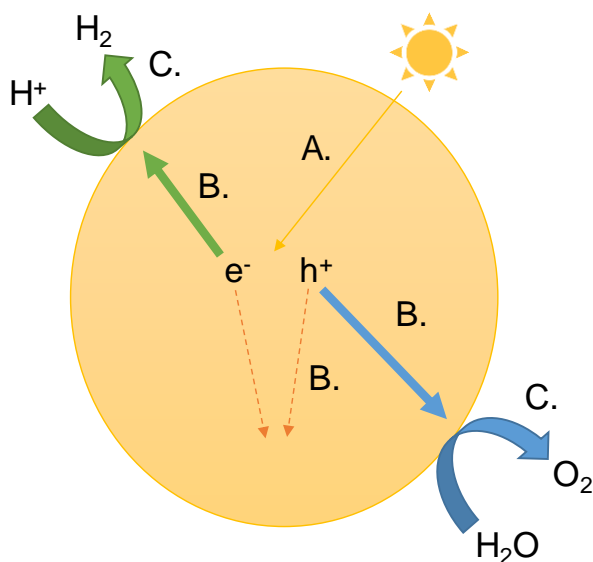


Figure 1.2 The main processes in photocatalytic water splitting, adapted from reference²⁴.

1.1.2. Photoelectrochemistry

The first implementation of a photoelectrochemical cell (PEC) was demonstrated by Fujishima and Honda using a rutile TiO_2 anode and Pt cathode driven by a potential bias¹⁶. The PEC was fabricated for the photodissociation of water into hydrogen and oxygen. Upon light irradiation, oxygen evolution occurred at the rutile TiO_2 anode and hydrogen

evolution occurred at the Pt cathode. This demonstration in 1972 led the way to using PECs with semiconductor electrodes for photoelectrochemical water splitting.

Photoelectrochemical cells usually consist of a three-electrode setup, with a counter electrode, reference electrode and the photocatalyst as the working electrode. The counter electrode is used to transfer electrons from the conduction band via an external bias. The electrons are then transferred to the electrolyte generating H_2 , while the photogenerated holes oxidise water to produce O_2 , as shown in Figure 1.3. Platinum is the most used counter electrode as it has high conductivity and excellent electrocatalytic properties to keep a high concentration of reducing agent in the electrolyte²⁵. There are many reference electrodes that are used in photoelectrochemistry, which are used as a standard versus the normal or reversible hydrogen electrode (NHE or RHE).

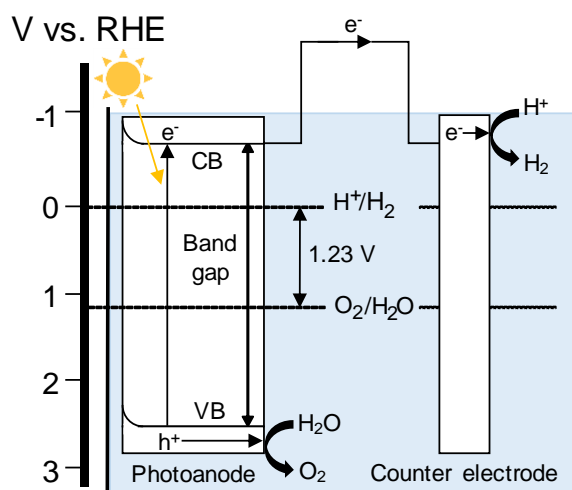


Figure 1.3 PEC system for photoelectrochemistry with an applied bias, adapted from reference²⁶.

The interface between the working electrode (containing the photocatalyst) and the electrolyte is very important in PECs; resulting in an equilibrium due to the difference in Fermi level between the semiconductor and electrolyte, which causes a flow of charge to form a Helmholtz layer²⁷. A space charge region (Δ_{sc}) is also formed as the semiconductor charge carrier density is small compared to the Debye length. The space charge region

illustrates the potential difference between semiconductor and electrolyte, which causes band bending of CB and VB, as shown in Figure 1.4. The space charge region (Δ_{sc}) is directed upwards in an n-type semiconductor and directed downwards in a p-type semiconductor. The band bending occurs as the Fermi level of the semiconductor is lower than the redox potential of the electrolyte, which causes a flow of electrons into the electrolyte and a higher concentration of holes on the semiconductor surface.

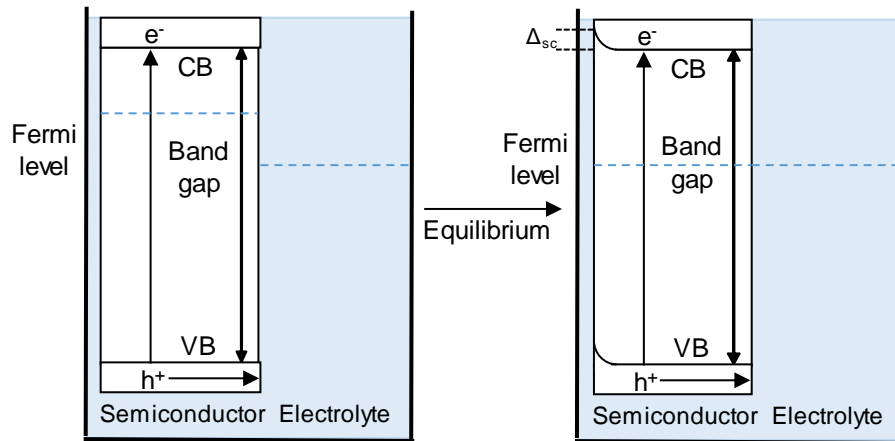


Figure 1.4 Band bending in a semiconductor-electrolyte interface after equilibrium.

1.1.3. Photocatalyst requirements

In photocatalysis, the role of the photocatalyst is significant for efficient hydrogen evolution. The most important properties of a photocatalyst in PECs are discussed further.

- i. The positioning of the conduction and valence band edge of a semiconductor is important because the band gap must straddle the oxidation and reduction potentials of water for water splitting to occur. Many semiconductors have various band gaps and band edges which do not straddle the oxidation and reduction potentials, as shown in Figure 1.5, thus the PEC requires additional potential to drive the water splitting reaction under illumination.

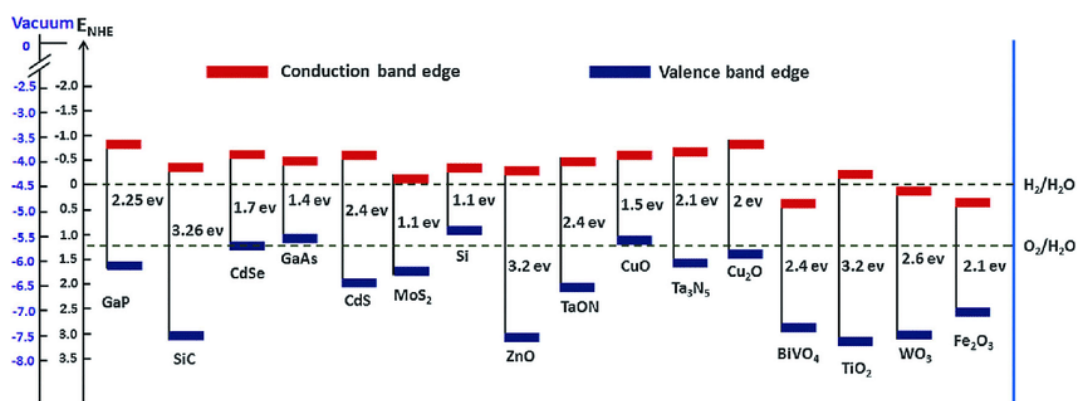


Figure 1.5 Conduction and valence band edges of semiconductors in an electrolyte at pH = 0, retrieved from reference²⁸.

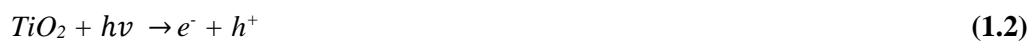
- ii. The crystallinity, structure and particle size greatly influence the separation and recombination of photogenerated charge carriers. The quality of crystallinity in a photocatalyst is affected by the number of defects in the structure, which act as trapping and recombination centres between photogenerated electrons and holes. This decreases photocatalytic activity, so it is necessary to maintain a high-quality crystalline structure to decrease the number of defects. The particle size of the semiconductor affects photocatalytic activity because recombination decreases with smaller particle size as there is a shorter pathway for photogenerated electrons and holes to migrate to the surface.
- iii. As 46% of the solar energy received from the sun is in the visible light region, there is emerging research on visible-light photocatalysts, which usually requires a band gap of lower than 3.0 eV ($\lambda > 400$ nm) to maximise the absorption of visible light. There are many methods to enhance photocatalytic activity of high band gap semiconductors in the visible light region, such as band gap engineering, doping and heterojunctions²⁹.
- iv. The electrical properties of the photocatalyst are important because photogenerated charge carriers must be transported efficiently upon illumination. Sodergren et al.³⁰ suggested that charge transport of photogenerated charge carriers in a nanostructured semiconductor occurs by diffusion. The diffusion lengths were introduced for

photogenerated charge carriers which are dependent on recombination losses. This means there is a higher chance of recombination with shorter diffusion lengths of electrons and holes. Therefore, nanostructured semiconductors can be modified for more efficient charge transfer, because lower recombination rates are achieved when the particle size of a nanostructured semiconductor is smaller than the diffusion length of electrons and holes.

- v. Chemical and structural stability of the photocatalyst is essential in practical applications for water splitting. When photogenerated charge carriers are generated upon illumination, electrons and holes can oxidise or reduce the semiconductor if they are not transported to the electrolyte. A popular catalyst that has photostability issues is Cu_2O , as it is easily oxidised into CuO under illumination³¹.

1.1.4. Photodecomposition of pollutants

Advanced oxidation technologies use sunlight to decompose organic pollutants such as hydrocarbons, aromatic compounds and dyes. The term advanced oxidation was defined after Glaze et al.³² proposed the generation of OH radicals in high quantity to affect water purification. The mechanism of photodecomposition is proposed to be driven forming reactive radical species, such as hydroxyl radical, through trapping the hydroxide ion at the valence band of a semiconductor photocatalyst³³. Oxygen is an important element required to decompose pollutants, as shown below³⁴.



The processes in the above equations³⁵ for the photodecomposition of organic pollutants using TiO_2 as the semiconductor are illustrated in Figure 1.6. Upon illumination, TiO_2 absorbs light with equal to or more energy than the band gap to promote an electron in the conduction band, while forming a positive hole in the valence band³⁶. The hole in the valence band is a powerful oxidising agent, which can oxidise organic compounds by reacting with H_2O to produce hydroxyl radicals ($\cdot\text{OH}$). The hydroxyl radical has a strong oxidation potential, so it can oxidise many organic molecules, eventually converting them into CO_2 and H_2O . Alternatively, O_2 can react with electrons in the conduction band forming an anion radical superoxide ($\text{O}_2^{\cdot-}$). Further reactions can lead to the formation of hydrogen peroxide, which also leads to the formation of $\cdot\text{OH}$. Dissolved oxygen is essential in the photodecomposition of pollutants because it increases the difficulty of electron-hole recombination. The reduction of O_2 and oxidation of organic pollutants must occur simultaneously to avoid the accumulation of electrons in the conduction band, thus reducing the chance of recombination.



Figure 1.6 Schematic of the photodecomposition of organic pollutants, retrieved from reference³⁶.

1.2. Low dimensional carbon materials

Carbon is present in all forms of living organisms, from very hard materials such as diamonds (used for drilling) to very soft materials such as graphite (used as lubricant in

skin care)³⁷. Carbon nanomaterials exhibit extraordinary electrical, thermal, chemical and mechanical properties³⁸. Zero, one, two and three-dimensional materials are basic forms of carbon nanomaterials illustrated in Figure 1.7, which includes carbon dots, carbon nanotubes or wires, graphene and graphene oxide.

Zero dimensional

One dimensional



Two dimensional

Figure 1.7 Different dimensional carbon nanostructures retrieved from reference³⁸.

1.2.1. Zero-dimensional carbon

The reason carbon modifications on photocatalysts is an attractive research area is because there is a demand on utilising a higher component of solar energy, visible light, as it consists of 46% of the solar spectrum. The emerging research of carbon quantum dots (CQDs) has demonstrated the ability to utilise visible light with unique optical, physiochemical, electronic, electrochemical properties³⁹. Xu et al. were the first group to discover CQDs⁴⁰, which was formed by single-walled carbon nanotubes (SWNTs) from crude soot. They found fluorescent components within the carbon nanotube fragments, which with the help of AFM, were identified as smaller than 20 nm. CQDs are comprised of graphitic or turbostratic carbon (sp^2 carbon) fused by sp^3 hybridised carbon and their physical size (less

than 20 nm) is smaller than distance of the photogenerated electrons and holes (known as an exciton Bohr radius) due to the quantum confinement effect. The quantum confinement effect occurs when the particle size of CQDs is so small that it is of the same order as an exciton Bohr radius, which causes the band of energies to turn into discrete energy levels.

It is commonly known that TiO₂ has a major drawback in photocatalysis, such as high band gap, which means it is only active in UV light. Therefore, CQDs emerged in research for photocatalysis as a form of band gap engineering. Li et al.³⁶ synthesised TiO₂/CQDs via an electrochemical synthesis route, and they learned CQDs exhibit strong photostability while retaining their photoluminescence (PL) properties. The TiO₂/CQDs were tested by photo-oxidation of dyes such as Methyl Blue (MB), of which nearly all was degraded in 25 minutes. This was compared to bare CQDs and TiO₂, which degraded a negligible amount in comparison. Figure 1.8 showed the PL spectra of CQDs excited by light at higher wavelengths (between 500 – 1000 nm) with upconverted emissions between 325 to 425 nm. Upconversion describes the mechanism where CQDs absorb longer wavelength photons (visible light) and then relax by emitting shorter wavelength UV photons, which induces TiO₂ photoexcitation.



Figure 1.8 Upconverted PL properties of CQDs, retrieved from reference⁴¹.

This understanding was used to propose a mechanism of TiO₂/CQDs under visible light, as shown in Figure 1.9. Upon illumination, TiO₂/CQDs absorb visible light and then emit light of shorter wavelength (between 325 to 425 nm) by upconversion, which excites TiO₂ to form electron-hole pairs⁴². The electron-hole pairs then react with the adsorbed oxidants/reducers (usually O₂/OH⁻) to produce active oxygen radicals (e.g. •O²⁻, •OH), which degrades the dye. These results suggest that CQDs may be used as a powerful energy-transfer component in photocatalysis. Consequently, when combining CQDs with a semiconductor such as TiO₂, carbon can utilise the full solar spectrum (based on upconversion PL properties of CQDs).



Figure 1.9 Proposed mechanism for TiO₂/CQDs under visible light, retrieved from reference⁴¹.

In a recent paper, Hazarika et al.⁴³ investigated the degradation of phenol using a TiO₂/CQD hybrid nanomaterial compared to bare TiO₂ nanoparticles. Along with other researchers, they verified that CQDs also possess excellent upconversion fluorescence by excitation at wavelengths between 650 to 800 nm, with upconversion between 420 to 525 nm. They recorded 93% degradation of phenol in 6.5 hours by TiO₂/CQD, whereas bare TiO₂ exhibited only slight photocatalytic activity for phenol degradation after 8 hours.

Yu et al.²⁶ manufactured CQD/TiO₂ P25 composites for efficient photocatalytic H₂ production via hydrothermal treatment. CQD/TiO₂ P25 exhibited improved photocatalytic activity under UV-Vis and visible light irradiation compared to pure P25 by superior transient photocurrent responses. The photocurrent response was enhanced over fivefold in the UV region and over six times in visible light irradiation. Yu's group proposed a more up-to-date mechanism for photocatalytic H₂ evolution using CQDs (demonstrated in Figure 1.10); where the CQDs played two crucial roles for enhancing the photocatalytic activity of TiO₂.

1. CQDs acted as an electron reservoir, which helped trap electrons being emitted from TiO₂ nanoparticles by light irradiation, this hindered recombination rate of electron-hole pairs.
2. In addition, CQDs acted as a dispersing support to control the morphology of TiO₂ in TiO₂/CQD hybrid nanomaterial, so it prevented agglomeration of TiO₂ nanoparticles.



Figure 1.10 More recent mechanism of CQDs in TiO₂/CQD hybrid nanomaterial, retrieved from reference²⁶.

Furthermore, Bian's group⁴⁴ investigated charge transfer properties of CQDs/TiO₂ nanorods through photoelectrochemical studies under visible light irradiation. The photocurrent density is enhanced with increased CQDs loading, which showed that CQDs are good sensitizers for TiO₂. The group concluded that the right loading of CQDs is needed to get a balance between charge transport and collection with increasing length of TiO₂ nanorods. They proposed that CQDs also facilitate electron transfer from TiO₂ and electrons are freely shuttled along the conducting paths of the CQDs. This allows more efficient charge separation and hindered recombination of electron-hole pairs by creating long-lived holes on the TiO₂ surface⁴⁵. However, the stability of CQDs needs further improvement because an increase in CQD concentration decreased the photocurrent, which may be caused by surface aggregation of CQDs or due to lower concentration of TiO₂. There is also extensive research on other metal oxide/CQD hybrids such as Fe₂O₃, ZnO, Cu₂O and SiO₂-CQD⁴⁶, which all successfully utilised visible light in their respective photocatalytic studies.

1.2.2. One-dimensional carbon

One-dimensional (1D) carbon nanomaterials are important nanostructures with high tensile strength⁴⁷, thermal and electrical conductivity⁴⁸, reported by Iijima in the form of carbon nanotubes (CNTs)⁴⁹. Iijima's group fabricated CNTs on the negative carbon electrode via an arc-discharge method. They concluded that 1D quantum effects enhanced electronic and mechanical properties of CNTs, which can potentially be used for various applications, such as mechanics, resins and tissue engineering^{50,51}. CNTs also possess unique optical properties, which is due to 1D confinement of electronic and phonon states, resulting in van Hove singularities in density of states⁵².

Carbon nanotubes (CNTs) are referred to as either single-wall carbon nanotubes (SWNTs) or multi-wall carbon nanotubes (MWNTs). SWNTs are the simplest form of CNTs as they are thought of as rolling a sheet of graphene into a cylinder along a lattice vector in the graphene plane, as proposed in Figure 1.11. There has been a wide range of nanotube synthesis over the years, with arc-discharge, laser ablation and chemical vapor deposition (CVD) the three main methods for CNT synthesis⁵⁴. However, these techniques are

expensive and have difficulty scaling up in industry. In the case of CVD, higher volumes of CNTs can be fabricated, but the carbon nanomaterials have a higher defect density⁵⁵. MWNTs are a form of CNTs where multiple SWNTs are nested inside one another.



Figure 1.11 Conceptual idea of SWNTs by folding graphene sheet along lattice vectors, retrieved from reference⁵³.

Another form of 1D carbon nanomaterials, called carbon nanofibers (CNFs), are classified as linear sp^2 based filaments, with an aspect ratio above 100⁵⁶. CNFs are composed of stacked graphene layers in a 1D structure⁴⁸, shown in Figure 1.12. They exhibit great physical properties in metal hybrids, as they contain strong thermal properties. CNFs are synthesised via various methods such as vapor growth, catalytic combustion, ultrasonic spray pyrolysis and many others⁵⁷.

1D carbon nanomaterials have emerged in photoelectrochemistry because they can improve charge transport of photogenerated electrons and holes. SWNTs were found to improve charge transfer in nanocomposite assemblies, as studied by Sheeney-Haj-Ichia and co-workers⁵⁹, where they fabricated CdS-SWNT nanocomposites. They analysed photocurrent responses under visible light irradiation and found very high efficiencies, which was related to the deactivation of excited CdS on the SWNT surface. Further studies showed the improved photocurrent was mainly due to the length of CNTs and the defects in the CNF promote charge separation, which was followed by the photoexcitation of CdS. This supported the idea that electrons were transferred from CdS through an electron-collecting network formed by SWNTs⁵⁹.



Figure 1.12 3D CAD rendering of graphene layers stacked as cups in a CNF, inset including TEM of orientation of graphene layers along the structure, retrieved from reference⁵⁸.

Furthermore, Kamat et al.⁶⁰ studied SWNTs for electron transportation in a photoelectrochemical cell. SWNTs can accept electrons and transfer them to electron acceptors, which show the mediating role of CNTs in the charge transfer process. CNTs are known to have unique electronic properties, as they can be synthesised to exhibit metallic conductivity due to their high electron storage (one electron per 32 carbon atoms), so CNTs can accept photogenerated electrons in nanocomposites, which hinders recombination.

In addition, it is reported that CNT-TiO₂ forms a Schottky barrier (common in semiconductor-metal junctions), which would also hinder recombination of photogenerated electrons and holes. Kamat⁶¹ also investigated the efficiency in harvesting solar light energy using CNTs. The report suggested CNTs were used to anchor the semiconductor particles to provide an easier way to capture photogenerated electrons and holes and transport them to the electrode surface, as shown in Figure 1.13.



Figure 1.13 Charge transfer in a carbon nanotube hybrid electrode, retrieved from reference⁶¹.

1.2.3. Two-dimensional carbon

Graphene is a two-dimensional (2D) carbon nanomaterial experimentally discovered by Novoselov et al.⁶² Graphene has gained popularity due to its unique structure, large surface area, thermal conductivity and excellent electronic mobility ($200,000 \text{ cm}^2\text{V}^{-1}\text{s}^{-1}$)⁶³. Graphene is a flat monolayer of sp^2 bonded carbon atoms that are arranged densely in a 2D hexagonal honeycomb crystal lattice⁶⁴.

Graphene has been coupled with semiconductors to enhance photocatalytic performance, as Zhang's group fabricated P25/graphene via hydrothermal treatment⁶⁵. P25/graphene showed 15 times higher transient photocurrent response and 70% more methylene blue (MB) dye degraded after 5 hours compared to pure P25. Additional studies of charge transfer between TiO_2 and graphene showed the electron-hole pair lifetime significantly increase from 10^{-7}s to 10^{-5}s . This was the result of more efficient electron-hole separation through electron injection from conduction band (CB) of TiO_2 into graphene, which reduced the recombination rate of electron-hole pairs⁶⁶.

Graphite can be oxidised to form graphene oxide (GO), which contains carboxyl groups at the edge, hydroxide and epoxide groups with carbon sp^2 domains⁶⁸. GO was incorporated in semiconductors, such as TiO_2 , for photoresponses under visible light irradiation as GO

could suppress charge recombination with their 2D profile⁶⁷. The 2D structure of GO has a high surface area and π -conjugated basal plane, which acts as an electron sink for semiconductors to facilitate charge separation and transport, as shown in Figure 1.14. GO/BiVO₄ was fabricated to test their photocurrent in a photoelectrochemical cell. GO/BiVO₄ exhibited a photocurrent of 65 $\mu\text{A}/\text{cm}^2$ compared to pure BiVO₄ of 8 $\mu\text{A}/\text{cm}^2$. This was due to the GO sheets facilitating electron transfer between the semiconductors to prevent recombination⁶⁹.



Figure 1.14 GO sheet improves exciton separation and electron transport, retrieved from reference⁶⁷.

Reduced graphene oxide (rGO) has more defects, lower conductivity and mechanical strength compared to graphene sheets, but their excellent scalability, physical properties and stability make it an appealing material⁷⁰. Fan and co-workers⁷¹ studied the difference using 2D and 1D carbon for photocatalytic activities and found P25-rGO was more effective than P25-CNTs for hydrogen evolution by evolving over 10 times more H₂.



Figure 1.15 Schematic of rGO extracting photogenerated electron from Cu_2O , retrieved from reference⁷².

rGO is used to increase photocatalytic activity and stability of unstable semiconductors, such as Cu_2O . In $\text{Cu}_2\text{O}/\text{rGO}$, rGO acts as an electron acceptor to extract photogenerated electrons from Cu_2O . This would increase charge separation efficiency and limit reduction of Cu_2O . Tran's group⁷² tested photostability by showing stable photocurrent over a one-hour period. Moreover, they learned that when Cu_2O was grown in situ on graphene sheets, graphene acted as a stabiliser to ensure effective dispersion of Cu_2O nanoparticles that resulted in good electron transport between Cu_2O and rGO. In addition, they proposed a schematic of rGO extracting photogenerated electrons from Cu_2O , as shown in Figure 1.15. The photostability of $\text{Cu}_2\text{O}/\text{rGO}$ showed stable a photocurrent response over an hour under illumination in 5 minute chopped light cycles.

Bell's group⁷³ fabricated TiO_2/rGO , which possessed enhanced charge transfer properties due to being 5 to 10 times more conductive than bare TiO_2 . The electron lifetimes of TiO_2/rGO was four times longer than TiO_2 , as rGO acted as highly conducting intra particle charge transport network. The stability of rGO was also investigated as an electron mediator, and the hydrogen evolution cycles over the second and third cycle was almost the same, indicating a stable system.

1.3. Thesis outline

After analysing the different carbon nanomaterials, it has verified the difficulty to fabricate a semiconductor that meets the necessary optical, electrical, physical and thermodynamic requirements for solar water splitting. However, certain aspects of the research were unanimous in recognising the importance of factors such as utilising visible light of the solar spectrum because UV light is an insignificant portion of solar energy. As there is extensive research on UV active materials with favourable characteristics for photocatalysis, modifying these to make a commercially viable system is a goal that may be achieved soon.

After investigating photocatalysts with different dimensional carbon, their strengths and weaknesses have been identified. Therefore, the thesis will focus on the design and fabrication of metal oxide/low dimensional carbon hybrids, and develop them with superior optical properties, enhanced charge transfer and increased stability compared to bare semiconductors to pave the way for next generation photocatalysts. This research will have a few objectives; the first objective will be the fabrication of visible light active nanocomposites using low dimensional carbon nanomaterials, after identifying existing photocatalysts in research. The second objective will be to achieve efficient electron-hole charge transfer within the photocatalyst using 1D carbon nanowires to improve photocatalytic activity compared to bare semiconductors. The final objective will be to analyse and modify unstable semiconductors using rGO for practical applications with an emphasis on catalyst photostability while maintaining high photocatalytic activity.

The outline of the Chapters are as follows; Chapter 2 examines the techniques used for the studies done in the thesis. The theories of the techniques were explained with fundamental equations to understand the reasons why the techniques were implemented. The reactor setup and methodology were described for photodecomposition studies, hydrogen evolution studies and photoelectrochemical analysis.

Chapter 3 explores the synthesis of carbon modifications using carbon quantum dots (CQDs) on 1D TiO₂ photocatalysts by hydrothermal treatment. The photodecomposition of pollutant and transient photocurrent responses are investigated to study the activity of the photocatalysts.

Chapter 4 examines the modification of $\text{TiO}_2/\text{Cu}_2\text{O}$ using carbon nanowires (C-NWs) via hydrothermal and subsequent solution phase chemistry. The C-NWs are prepared using gelatine as the carbon precursor. The catalyst interfacial studies and electrochemical impedance spectra are used to determine the energy band structures of the nanocomposite.

Chapter 5 describes the synthesis of hierarchical Cu_2O nanospheres and fabrication of $\text{Cu}_2\text{O}/\text{rGO}$. The photocatalysts are characterised and the photocatalytic activity are examined by photoelectrochemical analysis, hydrogen evolution in visible light and photodecomposition of 4-chlorophenol (4-CP).

Chapter 6 studies quantum dot BiVO_4 on reduced graphene oxide (QD- BiVO_4/rGO). QD-photocatalytic activity of QD- BiVO_4/rGO activity are tested by hydrogen evolution in visible light, photodecomposition of Bisphenol-A and photoelectrochemical analysis.

Chapter 7 concludes all the key results obtained from the studies and suggests further work that would give greater understanding in photocatalytic mechanisms.

1.4. References

1. Tsao, J.; Lewis, N.; Crabtree, G. Solar FAQs; *U.S. Department of Energy* **2006**, 1.
2. Sullivan, I.; Zoellner, B.; Maggard, P.A. *Chem. Mater.* **2016**, *28*, 5999.
3. Hoffert, M.I.; Caldeira, K.; Jain, A.K.; Haites, E.F.; Danny Harvey, L.D.; Potter, S.D.; Schlesinger, M.E.; Schneider, S.H.; Watts, R.G.; Wigley, T.M.L.; Wuebbles, D.J. *Nature*. **1998**, *381*, 395.
4. Petit, J.R.; Jouzel, J.; Raynaud, D.; Barkov, N.I.; Barnola, J.-M.; Basile, I.; Benders, M.; Chappellaz, J.; Davis, M.; Delaygue, G.; Delmotte, M.; Kotlyakov, V.M.; Legrand, M.; Lipenkov, V.Y.; Lorius, C.; Pepin, L.; Ritz, C.; Saltzman, E.; Stievenard, M. *Nature*. **1999**, *399*, 399.
5. International action on climate change, *European Commission* **2015**. Available at: https://ec.europa.eu/clima/policies/international/negotiations/paris_en.
6. Framework convention on climate change, *United Nations* **2014**. Available at: http://unfccc.int/kyoto_protocol/items/3145.php.
7. Climate Change Act **2008**. Available at: http://www.legislation.gov.uk/ukpga/2008/27/pdfs/ukpga_20080027_en.pdf.
8. Updated energy and emissions projections, *Department of Energy & Climate Change* **2015**. Available at: <https://www.gov.uk/government/publications/updated-energy-and-emissions-projections-2015>.
9. Kamat, P.V. *J. Phys. Chem. C*. **2007**, *111*, 2834.
10. Government pledges boost for low emission vehicles, *UK Government* **2016**. Available at: <https://www.gov.uk/government/news/government-pledges-290-million-boost-for-low-emission-vehicles>.
11. Government's clean energy drive, *UK Government* **2017**. Available at: <https://www.gov.uk/government/news/governments-clean-energy-drive-invests-35-million-in-innovative-projects>.
12. Esswein, A.J.; Nocera, D.G. *Chem. Rev.* **2007**, *107*, 4022.
13. UK Renewables report **2019**. Available at: https://assets.publishing.service.gov.uk/government/uploads/system/uploads/attachment_data/file/835114/Renewables_September_2019.pdf
14. Photovoltaics Report **2019**. Available at: <http://www.ise.fraunhofer.de/en/downloads-englisch/pdf-files-englisch/photovoltaics-report-slides.pdf>
15. Feifei, G.; Wang, Y.; Zhang, J.; Shi, D.; Wang, M.; Humphry-Baker, R.; Wang, P.; Zakeeruddin, S.M.; Gratzel, M. *Chem. Comm.* **2008**, *23*, 2635.
16. Fujishima, A.; Honda, K. *Nature*. **1972**, *238*, 37.
17. Ahmad, H.; Kamarudin, S.K.; Minggu, L.J.; Kassim, M. *Ren. & Sus. Energy Rev.* **2015**, *9*, 43.
18. Granovskii, M.; Dincer, I.; Rosen, M.A. *Int. J. Hyd. Energy* **2006**, *31*, 337.
19. Badwal, S.; Giddey, S.; Munnings, C. *Wires En. & Environ.* **2013**, *2*, 5.
20. Chen, X.; Shen, S.; Guo, L.; Mao, S.S. *Chem. Rev.* **2010**, *110*, 11.
21. Zaytseva, O.; Neumann, G. *Chem. Biol. Technol. Agric.* **2016**, *3*, 17.
22. Rajeshwar, K. *Journ. App. Elect.* **2007**, *37*, 765.
23. Abe, R. *J. Photochem. & Photobio. C*. **2010**, *12*, 2780.
24. Rahimi, N.; Pax, R.A.; Gray, E.M. *Prog. Solid State Chem.* **2016**, *44*, 86.
25. Peng, H.; Fang, X. *Polymer Materials for Energy and Electronic Applications*. **2017**.
26. Yu, H.J.; Zhao, H.F.; Zhou, C.; Shang L.; Peng Y.; Cao Y.H.; Wu, L.Z.; Tung, C.H.; Zhang, T.R. *J. Mat. Chem. A*. **2014**, *2*, 3344.
27. Green, M. *J. Chem. Phys.* **1959**, *31*, 200.

28. Tamirat, A.G.; Rick, J.; Dubale, A.A.; Su, W-N.; Hwang, B-J. *Nanoscale Horiz.* **2016**, *1*, 4.
29. Kudo, A.; Miseki, Y. *Chem. Soc. Rev.* **2009**, *38*, 253.
30. Södergren, S.; Hagfeldt, A.; Olsson, J.; Lindquist, S-E. *J. Phys. Chem.* **1994**, *98*, 5552.
31. Toe, C.Y.; Zhaoke, Z; Wu, H; Scott, J; Amal, R; Y.H, Ng. *Angew. Chem.* **2018**, *130*, 13801.
32. Glaze, W.H.; Kang, J-W.; Chapin, D.H. *J. Inter. Ozone Assoc.* **1987**, *9*, 4.
33. Yu, Y.; Yu, J.C.; Chan, C.-Y.; Che, Y.-K.; Zhao, J.-C.; Ding, L.; Ge, W.-K.; Wong, P.-K. *Appl. Cat. B: Environ.* **2005**, *1*, 61.
34. Hoffmann, M.R.; Martin, S.T.; Choi, W.; Bahnemann, D.W. *Chem. Rev.* **1995**, *69*, 95.
35. Umar, M.; Aziz, H.A. Organic Pollutants -Monitoring, Risk and Treatment. **2012**.
36. Mills, A.; Le Hunte, S. *Journ. Photochem. & Photobio. A: Chem.* **1997**, *108*, 1.
37. Fink, J. Petroleum Engineer's Guide to Oil Field Chemicals and Fluids, 2nd edition. **2015**.
38. Han, X.; Li, S; Peng, Z.; Al-Yuobi, A.O.; Bashammakh, A.S.O.; El-Shahawi, M.S.; Leblanc, R.M. *J. Oleo. Sci.* **2016**, *65*, 1.
39. Karfa, P.; Sharma, P.K. Comprehensive Nanoscience and Nanotechnology, 2nd edition. **2019**.
40. Xu, X.; Ray, R.; Gu, Y.; Ploehn, H.J.; Gearheart, L.; Raker, K.; Scrivens, W.A. *J. Am. Chem. Soc.* **2004**, *126*, 40.
41. Li, H.; He, X.; Kang, Z.; Huang, H.; Liu, Y.; Liu, J. et al. *Ange. Chemie Int. Ed.* **2010**, *4430*, 49.
42. Kang, Z.H.; Liu, Y.; Tsang, C.H.; Ma, D.D.; Fan, X.; Wong, N.B. *Adv. Mater.* **2009**, *21*, 661.
43. Hazarika, D.; Karak, N. *Appl. Sur. Sci.* **2016**, *276*, 376.
44. Bian, J; Huang, C; Wang, Li; Hung, T; Daoud, W.A.; Zhang, R. *Appl. Mater. Interfaces.* **2014**, *6*, 7.
45. Yao, Y.; Li, G.H.; Ciston, S.; Lueptow, R.M.; Gray, K.A. *Environ. Sci. Technol.* **2008**, *42*, 4952.
46. Lim, S.Y.; Shen, W; Gao, Z. *Chem. Soc. Rev.* **2014**, *44*, 362.
47. Yu, M-F.; Lourie, O.; Dyer, M.; Moloni, K.; Kelly, T.F.; Ruoff, R.S. *Science.* **2000**, *287*, 5453.
48. Kim, P.; Shi, L.; Majumdar, A.; McEuen, P.L. *Phys. Rev. Lett.* **2001**, *87*, 215502.
49. Iijima, S. *Nature.* **1991**, *344*, 56.
50. Dresselhaus, M.S.; Dresselhaus, G.; Avouris, P. Springer-Verlag, Berlin. Carbon Nanotubes: Synthesis, Structure, Properties and Applications. **2001**.
51. Zanello, L.P.; Zhao, B.; Hu, H. Haddon, R.C. *Nano Lett.* **2006**, *6*, 3.
52. Dresselhaus, M.S.; Dresselhaus, G.; Saito, R.; Jorio, A. *Physics Reports* **2005**, *2*, 47.
53. Dai, H. *Acc. Chem. Res.* **2002**, *35*, 12.
54. Dai, H. Nanotube Growth and Characterization. Carbon Nanotubes, Springer: Berlin, **2001**, 29.
55. Hammel, E.; Tang, X; Trampert, M.; Schmitt, T.; Mauthner, K.; Eder, A; Potschke, P. *Carbon.* **2004**, *42*, 1153.
56. Kim, Y.A.; Hayashi, T.; Endo, M.; Dresselhaus, M.S. Springer handbook of nanomaterials. **2013**.
57. Mostofizadeh, A.; Li, Y.; Song, B.; Huang, Y. *Journ. Of. Nano.* **2011**, *1*.
58. Poveda, R.L.; Gupta, N. Carbon Nanofibers: Structure and Fabrication. **2015**.
59. Sheeney-Haj-Ichia, L.; Basnar, B.; Willner, I. *Angew. Chem. Int. Ed.*, **2004**, *44*, 78.
60. Kongkanand, A.; Kamat, P.V. *ACS Nano.* **2007**, *1*,13.
61. Kamat, P.V. *Nano today.* **2006**, *4*, 1.

62. Novoselov, K.S.; Geim, A.K.; Morozov, S.V.; Jiang, D.; Zhang, Y.; Dubonos, S.V.; Grigorieva, I.V.; Firsov, A.A. *Science*. **2004**, *306*, 5696.
63. Du, X.; Skachko, I.; Barker, A.; Andrei, E.Y. *Nat. Nanotechnol.* **2008**, *3*, 8.
64. Novoselov, K.S.; Geim, A.K. *Nat. Mater.* **2007**, *6*, 183.
65. Zhang, Y.; Pan, C. *J. Mater. Sci.* **2011**, *46*, 2622.
66. Wang, P.; Zhai, Y.; Wang, D.; Dong, S. *Nanoscale*. **2011**, *3*, 1640.
67. Yeh, T-F.; Cihlar, J.; Chang, C-Y.; Cheng, C.; Teng, Hsisheng. *Mat. Today*. **2013**, *16*, 3.
68. Hontoria-Lucas, C.; Lopez-Peinado, A.L.; Lopez-Gonzalez, J.D.D.; Rojas-Cervantes, M.L.; Martin-Aranda, R.M. *Carbon*, **1995**, *33*, 1585–1592.
69. Ng, Y.H.; Iwase, A.; Kudo, A.; Amal, R. *J. Phys. Chem. Lett.* **2010**, *1*, 17.
70. Compton, O.C.; Nguyen, S.T. *Small*. **2010**, *6*, 6.
71. Fan, W.; Lai, Q.; Zhang, Q.; Wang, Y. *J. Phys. Chem. C*. **2011**, *115*, 10694.
72. Tran, P.D.; Batabyal, S.K.; Pramana, S.S.; Barber, J.; Wong, L.H.; Loo, S-C-J. *Nanoscale*. **2012**, *13*, 1.
73. Bell, N.J.; Ng, Y.H.; Du, A.; Coster, H.; Smith, S.C.; Amal, R. *J. Phys. Chem.* **2011**, *115*, 13.

Chapter 2

Methodology

The fabricated photocatalysts can be categorised using an array of characterisation methods, which are essential in engineering new and improved catalysts. The synthesis of photocatalysts will be described in their respective chapters. A methodology is proposed for the major aspects of the thesis.

- i. Characterisation methods
- ii. Photoelectrochemical analysis
- iii. Reactor setup

2.1. Characterisation methods

Characterisation of photocatalysts are necessary to understand their structural and optical properties, which can then be compared with literature. The different characterisation techniques show the inner studies of a photocatalyst.

2.1.1. X-ray Diffraction (XRD)

XRD uses electromagnetic radiation to identify the molecular structure of a photocatalyst. The x-rays are fired onto the photocatalyst and cause Rayleigh scattering. Figure 2.1 shows the diffraction of x-rays by crystal planes, which enables the derivation of lattice spacing by Bragg's law¹.

$$2d\sin \theta = n\lambda \quad (2.1)$$

Where d is the atomic spacing, θ is the scattering angle, n is the integer and λ is the wavelength of electromagnetic radiation. The moving particles have a wavelength called

the de Broglie wavelength. Strong peaks known as Bragg peaks are obtained in the diffraction pattern at points where the scattering angles satisfy Bragg's law. This technique is used to determine the crystallinity, composition and physical properties of the photocatalysts.

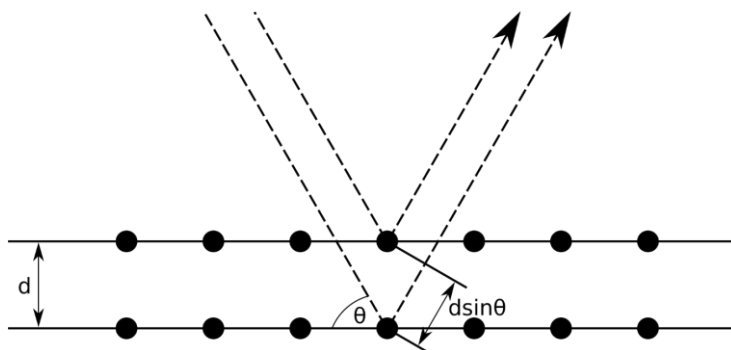


Figure 2.1 Schematic demonstration of Bragg's law.

More in-depth analysis shows crystallite size and average distance between molecules in the photocatalyst. The average particle or crystallite size is calculated (τ) by Scherrer's equation².

$$\tau = \frac{K\lambda}{\beta \cos \theta} \quad (2.2)$$

Where τ is the mean crystallite size, K is the shape factor (or Scherrer constant) which depends on the geometry of the scattering objects, λ is the x-ray wavelength, β is the line broadening at half maximum intensity, θ is Bragg's angle. Scherrer's equation only applies to nanoparticles, limited to a grain size of 0.1 μm . As shown in Equation 2.2, larger crystallite size (τ) indicates a smaller β , which means larger crystallite size of a photocatalyst has sharper peaks in XRD.

XRD was carried out using a Bruker-AXS D8 ADVANCE diffractometer operated at 40 kV and 40 mA and Cu $K\alpha$ radiation ($\lambda = 0.15418 \text{ nm}$) between 2θ 10-80° at a scan rate of 1°/min.

2.1.2. X-ray Photoelectron Spectroscopy (XPS)

XPS is used to analyse emitted photoelectron energy distribution of photocatalysts when a sample is bombarded by x-ray photons. The energy of the x-ray photons identifies samples by measuring elemental composition, electronic structure and chemical state of elements. When a sample is irradiated by x-ray photons (Figure 2.2), the energy is transferred from the photon to the core level electrons, emitting a photoelectron, which is detected by an electron energy analyser³. The energy of the photoelectron is a characteristic of the atomic and molecular structure from where it was emitted.

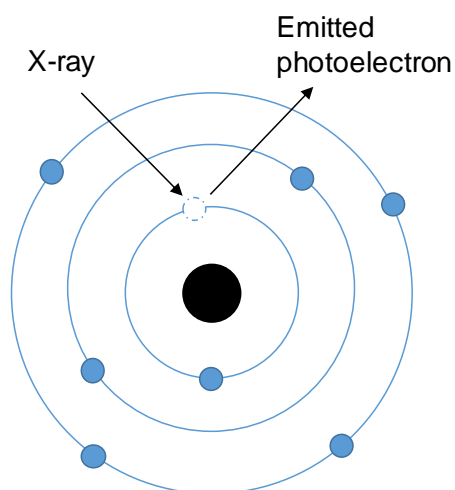


Figure 2.2 Mechanism of energy transfer from x-ray photon irradiation to core level electrons in XPS.

A photoelectron is emitted by absorption of the x-ray photon, which gains kinetic energy as shown in the conversion of energy equation.

$$E_B = E_\gamma - E_K - \varphi \quad (2.3)$$

Where E_B is the binding energy of the electron, $E\gamma$ is the energy of the x-ray photon, E_K is the kinetic energy of the electron and φ is the work function of the instrument. From Equation 2.3, as the photoemitted electrons hit the detector, the electron intensity and core level binding energy are recorded as a peak. The core level binding energy is unique to each element, which identifies the element and electron orbital.

XPS was undertaken on a Kratos Axis HSi spectrometer with monochromated Al K α X-ray source operated at 90 W and normal emission, with magnetic focusing and a charge neutraliser. Spectra were fitted using CasaXPS version 2.3.16, with energy referencing to adventitious carbon at 284.6 eV, and surface compositions derived through applying appropriate instrumental response factors.

2.1.3. Brunauer-Emmett-Teller (BET) analysis

The BET theory⁴ is related to the physisorption of gas molecules on a solid surface from Van der Waals forces. This method can be used to measure specific surface area of photocatalysts, because a larger surface area leads to more active sites per unit area which increases photocatalytic activity. The BET theory is an extension of the Langmuir theory⁵, which describes monolayer gas absorption, for multilayer absorption.

$$\frac{1}{v\left[\left(\frac{\rho_0}{\rho}\right)-1\right]} = \frac{c_B-1}{v_m c_B} \left(\frac{\rho}{\rho_0}\right) + \frac{1}{v_m c_B} \quad (2.4)$$

Where v is the volume of adsorbed gas, ρ_0 and ρ are the saturation pressure of physisorbed gas and partial vapour pressure, c_B is the BET constant, v_m is the volume of adsorbed gas to produce a monolayer.

This method is used to calculate specific surface area of photocatalysts (S_{BET}) by physisorption of gas.

$$S_{BET} = \frac{a(v_m N s)}{V_A} \quad (2.5)$$

Where a is the mass of the adsorbent, v_m is the volume of adsorbed gas to produce a monolayer, N is Avogadro's constant, s is the adsorption cross section of the adsorbent and V_A is the molar volume of adsorbed gas.

BET surface areas were obtained by N_2 physisorption at 77 K using a Quantachrome NOVA 4000e porosimeter on samples degassed at 120 °C for 4 h. Surface areas were calculated over the relative pressure range 0.01-0.2.

2.1.4. Diffuse Reflectance UV-Visible Spectroscopy (DRUVS)

DRUVS is an essential technique used to calculate the absorption spectra of photocatalysts, which illustrates the absorbance intensity and wavelength range of a materials absorbance. The wavelength range of which a material absorbs is known as the optical range, which covers UV, visible and infrared regions. At these wavelengths, molecules undergo electron transitions as semiconductors have discrete energy levels based on electron states. This can determine the size of the band gap, using a Tauc plot⁶, which identifies the optical absorption spectrum of amorphous materials.

$$\alpha h\nu = C(h\nu - E_{BG})^n \quad (2.6)$$

Where α is the absorption coefficient, $h\nu$ is the energy of light, C is the proportionality constant based on electrons and holes masses, E_{BG} is the band gap of the photocatalyst and n depends on band gap transition type.

The absorption coefficient is calculated using Kubelka-Munk formula⁷, who proposed a model to describe the behaviour of light travelling through a light-scattering specimen.

$$\alpha = \frac{(1-R)^2}{2R} \quad (2.7)$$

Where α is the absorption coefficient and R is the reflectance.

If the wavelength at maximum absorbance is identified from UV-Vis spectroscopy, the band gap of a semiconductor can be estimated by the energy equation.

$$E_{BG} = \frac{hc}{\lambda} \rightarrow \frac{1240.8}{\lambda} \quad (2.8)$$

Where E_{BG} is the band gap energy of a semiconductor, h is Planck's constant, c is the speed of light and λ is the wavelength at maximum absorbance.

DRUVS was recorded on a Thermo Scientific Evo220 spectrometer using an integrating sphere, and KBr was used as a standard, with band gaps determined between 200-800 nm. The UV-Visible spectrophotometer used for absorbance spectra was Perkin Elmer Lambda 35.

2.1.5. Thermogravimetric Analysis (TGA)

Thermogravimetric analysis is used for material characterisation through decomposition analysis, where the mass of a sample is measured against time or temperature. TGA is conducted on a thermogravimetric analyser, which measures the mass of the sample as temperature changes over time. A thermogravimetric analyser consists of a weighing balance with a pan located in a furnace with programmable temperature control. Temperature can be ramped at different rates in different atmospheres and pressures. TGA is recorded as a plot of mass or % mass versus either temperature or time. 10 mg samples were prepared on alumina crucibles and heated from 25 to 800 °C, at 10 °C/min with a flow rate of 20 ml/min of N₂ over a two-hour period.

2.1.6. Gas Chromatography (GC)

GC is a useful way to analyse the concentration and amounts of materials in the gas phase, which is essential in water splitting as hydrogen and oxygen evolution is prevalent. As the

gaseous sample is injected into the GC, the components of the gaseous sample are separated due to the difference between the mobile phase of the gaseous sample and stationary phase of the chromatographic column.

GC's are usually fit with a thermal conductivity detector (TCD), which detects the changes in thermal conductivity produced by sample carrier gas flow. The usual carrier gases are nitrogen, helium and argon. Data is displayed in a graph as retention time (x-axis) versus detector response (y-axis). The retention time is the time required to elute each component from the stationary phase and the detector response is dependent on thermal conductivity and amount of each component. The chromatographic data shows a spectrum of peaks separated by time, and the area under the peak shows the amount of substance present. When a calibration curve is used, the amount of substance present can be determined as well as identifying the element by the unique retention time.

The GC used was a Shimadzu Tracera GC-2010 Plus fitted with a Carboxen1010 capillary column (30 m×0.53 mm×0.1 μm), TCD (using a He carrier) for gas analysis, heated injector and electronic pressure control hardware.

2.1.7. Scanning Electron Microscopy (SEM)

SEM produces images of a sample by scanning the surface with a focussed beam of electrons. The electrons interact with atoms in the sample, containing information on surface topography and composition of the sample. The interaction between the electron beam and sample produces an image that provide information of the surface sample, such as composition (elements and compounds present), morphology (shape and size of particles) and crystallography (arrangement of atoms).

The signals used by SEM to produce an image result from interactions of the electron beam with atoms at various depths in the sample. After the electron beam interacts with the surface of the sample, the sample emits electrons such as secondary electrons and back-scattered electrons which are recorded by secondary electron detectors and turned into an image. Narrow electron beams cause SEMs to have a large depth image to understand the surface structure of the sample.

SEM sample preparation must be small enough to fit on the specimen and needs careful preparation to increase electrical conductivity and stability, so they can withstand high vacuum and high energy beams. The samples were prepared by mounting on a stub using a conductive adhesive. It is important the samples are electrically conductive and grounded to prevent accumulation of electrostatic charge. Non-conductive samples are coated with thin coating of electrically conducting materials.

The SEM samples were prepared as described and given to a technician to produce SEM images.

2.1.8. Transmission Electron Microscopy (TEM)

TEM is a powerful technique which requires a high energy electron beam to interact with the sample, and the interactions between the electrons and atoms are used to observe the crystal structure of the sample. The electron beam is focussed into a small beam by using a condenser lens. Some of the electron beam that illuminates the sample is transmitted, which is dependent on thickness and electron transparency of the sample. The transmitted electron is focussed by the objective lens into an image. Optimal objective apertures can be used to enhance the contrast by blocking high angle diffracted electrons. The image is passed down the column through the intermediate and projector lenses, enlarged all the way.

The sample is prepared as a very thin sample as electrons must be transmitted to form an image. The intensity of the electron beam results in different contrasts in the image. There are dark and light zones within the sample image, which is related to the number of electrons transmitted because dark zones have fewer transmitted electrons and light zones have more. Thus, lower intensity of the electron beam corresponds to darker zones and higher intensity of the electron beam corresponds to lighter zones. This is associated with the scattering power of the atoms, as heavier atoms scatter more than lighter atoms. Also, it is important to understand the amount of scattering in a thick area of a sample will occur more frequently than in a thin area of the sample. Therefore, the dark zones link to heavier atoms or thicker areas of the sample and light zones link to lighter atoms or thin areas of the sample. Furthermore, TEM can examine non-conductive sampling and identify

diffraction zones which show the crystalline nature of the sample. If the instrument parameter is known, the diffraction size shows the d-spacing of the crystal structure.

TEM was performed on a JEM-2100Plus microscope operated at 200 kV (Warwick University, UK); samples were dispersed in ethanol and ultrasonicated for 5 minute and then drop casted on Cu grid coated with carbon film.

2.1.9. Raman Spectroscopy

Raman spectroscopy is used to detect vibrational, rotational and other low frequency modes in a system⁸. In Raman spectroscopy, the vibrational modes are observed by inelastic scattering of monochromatic light, which is used to illuminate the sample. This means the frequency of photons in monochromatic light changes when interacting with the sample. The photons are absorbed by the sample and reemitted, and the frequency of the reemitted photons is shifted up or down in comparison with the original monochromatic frequency.

Raman spectroscopy is based on molecular deformations in an electric field determined by the scale of polarisability. Elastic (Rayleigh) scattering occurs when photon excites a ground vibrational state (g_0) to a virtual state and returns to the same energy ground state. Raman scattering is split into Stokes and Anti-Stokes scattering; Stokes scattering occurs when a photon excites ground vibrational state to a virtual state and is reemitted with lower energy. The difference in photon energy is the difference between the vibrational energy. Anti-stokes scattering occurs when the photon excites a higher energy vibrational state (g_1) to a higher virtual state, and then returns to the ground vibrational state, as shown in Figure 2.3.

Raman spectroscopy requires minimal preparation, as the sample is simply placed in the laser beam direction. Monochromatic light is Raman scattered by the sample and focussed onto a detector. The Rayleigh scattered photons have no energy change, so it is rejected using an edge filter. The Raman shift is calculated by the difference between initial laser wavelength and Raman scattered wavelength. The plot is a function of Raman shift (cm^{-1}) versus intensity and shows the vibrational states in a sample. In photocatalysis, Raman spectroscopy is used to detect impurities on the surface of the photocatalyst, which can affect photocatalytic activity⁹. Alternatively, the change in Raman shift can show the

different energy states of bonds at specific wavelengths. The different bond energy can show a difference in photocatalytic activity too.

Raman measurements were performed using Renishaw InVia Raman microscope at a wavenumber range between 100-2000 cm^{-1} , Ar laser was set at 10mW but varied with the sample.

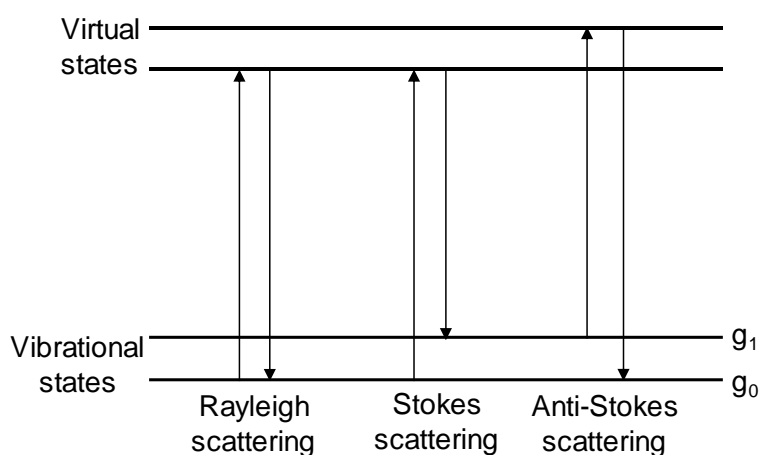


Figure 2.3 Diagram of the vibrational modes with Rayleigh, Stokes and Anti-stokes Raman scattering in a system.

2.2. Photoelectrochemical analysis

Photoelectrochemistry is an essential way to study and regulate the photocurrent activity of photocatalysts. The photocurrent is generated when the photocatalyst is connected to a counter electrode (CE) in a closed circuit, so the redox reactions occur on the electrode surface. The photocurrent is recorded when the charge carriers are in the redox reaction, therefore, the photocurrent response is the measurement of the speed that photogenerated charge carriers are transferred and collected.

Photoelectrochemistry is investigated using a potentiostat, which applies a potential to the electrodes in a photoelectrochemical cell and analyses the photocurrent response to the working electrode. Photoelectrochemistry in the thesis takes place in a three-electrode system, consisting of a working electrode (WE), reference electrode (RE) and (CE), with 200 W Hg-Xe arc lamp as the light source and 0.5 M Na₂SO₄ as the electrolyte.

2.2.1. PEC measurements

Two main methods of PEC measurements were conducted in order to measure the performance of the WE; which are transient and steady state photocurrent responses. Steady state photocurrent responses were investigated by performing linear sweep voltammetry (LSV) at a scan rate of 10 mV/s. The results in LSV responses provide information on photocurrent density, onset potential, limiting photocurrent and so on.

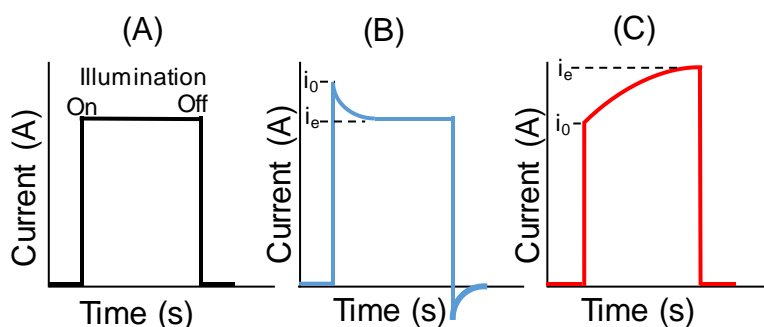


Figure 2.4 Chopped illumination of chronoamperometric measurement, where i_0 is the initial photoexcitation current and i_e is the photocurrent at equilibrium. (A) is an ideal photocurrent response, (B) requires exponential decay over time, (C) requires time to reach equilibrium.

The transient photocurrent responses were studied by chopped illumination chronoamperometry, which is an electrochemical technique where the current is monitored

over time. The relationship between current and time is recorded after applying a single potential step on the WE. The three main chronoamperometric responses in the thesis are shown in Figure 2.4, where i_0 is the photocurrent upon initial excitation by rapid charge carrier separation. Figure 2.4(A) shows an ideal photocurrent response, where there is initial photoexcitation upon illumination followed by immediate equilibrium with no charge separation. In contrast, Figure 2.4(B) indicates initial photoexcitation, but then exponential decay ensues over time due to the current difference as a result of surface recombination¹⁰. The final Figure 2.4(C) has a slow initial photocurrent response which could be the result of having a low concentration of charge carriers. Thus, equilibrium is achieved near the end of the chopped illumination as recombination is inhibited by higher internal electric fields¹¹, which occurs at lower applied bias (0V vs. RHE in this case).

2.2.2. Electrochemical Impedance Spectroscopy (EIS)

Frequency response measurements were carried out by EIS, which is used to investigate the interfacial, physicochemical and charge transport properties of a photocatalyst¹². This method is studied by applying AC signal to a PEC and the current is recorded, which is a sum of sinusoidal functions. At the semiconductor/electrolyte surface impedance is formulated as a real (Z') and imaginary (Z'') part.

$$Z(\omega) = Z'(\omega) + iZ''(\omega) \quad (2.9)$$

The semiconductor/electrolyte interface is compared to an electric circuit which uses charge transfer resistance and space charge capacity for semiconductor electrodes. The real versus imaginary part of impedance is measured using a Nyquist plot, which is used to calculate the charge transfer resistance.

Nyquist plots were recorded at 0 V vs. RHE under illumination and in the dark using 10 mV AC signal between 100 kHz to 0.1 Hz frequency.

EIS is also used to measure the capacitance of photocatalysts at the semiconductor/electrolyte interface. A Mott Schottky (MS) plot describes the reciprocal of

the capacitance squared $\left(\frac{1}{c^2}\right)$ versus the potential difference between semiconductor and electrolyte¹³. The MS plot is used to measure the changes in the semiconductor/electrolyte interface as the DC voltage is changed. A small signal AC potential excitation is applied to PEC. The impedance of the electrode interface is measured as a function of DC voltage. MS plots are linear and determine flat-band potential and donor density, given by the Mott-Schottky equation.

$$\frac{1}{c^2} = \frac{2}{\varepsilon\varepsilon_0eN_A} \left(V - E_{fb} - \frac{k_B T}{e} \right) \quad (2.10)$$

Where c is the capacitance, ε is the dielectric constant, ε_0 is the permittivity of free space, e is the electron charge, N_A is the majority carrier density, V is the applied potential, E_{fb} is the flat-band potential, k_B is the Boltzmann's constant and T is the temperature.

Furthermore, using the flat-band potential, the valence band edge (E_V), of p-type semiconductors can be calculated using Equation 2.11.

$$E_V = E_{fb} - k_B T \ln \frac{N_V}{N} \quad (2.11)$$

Where E_V is the valence band edge, E_{fb} is the flat-band potential, k_B is the Boltzmann's constant, T is the temperature and N is Avogadro's constant.

Where the effective density of states, N_V , is calculated using Equation 2.12.

$$N_V = 2 \left(\frac{2\pi m_h k_B T}{h^2} \right)^{\frac{3}{2}} \quad (2.12)$$

The effective hole mass is denoted as $m_h = X m_e$, where X is dependent on the compound, m_e is the mass of a free electron, k_B is the Boltzmann's constant, T is the temperature and h is Planck's constant

Mott Schottky plots were recorded at frequency of 1000 Hz under DC signal at potential range of -1 to 0 V with potential step of 10 mV.

2.3. Reactor setup

For reproducible photocatalytic experiments, two reactors were fabricated for different purposes. A photocatalytic reactor was manufactured for the photodecomposition of pollutants and hydrogen evolution reactions. A photoelectrochemical cell (PEC) was used to study photoelectrochemical measurements in a three-electrode system.

2.3.1. Photodecomposition of pollutants

Pollutant photodecomposition was carried out in two separate reactor setups, the first setup used a sealed 40 ml quartz reactor with 200 W Hg-Xe lamp as the light source. The photocatalyst (10 mg) was dispersed in 20 ml of 40 mg/l methylene blue (MB) dye by 7-minute ultrasonication and was stirred for 120 minutes in the dark to reach equilibrium in molecular adsorption. The photo-oxidation of dyes was carried out using a UV cut-off filter, with visible light as the target spectrum.

The second setup used a sealed quartz photoreactor (260 ml volume) with a 200 W Hg-Xe arc lamp (including UV cut-off filter) as shown in Figure 2.5, and the temperature maintained at 25 °C by a Huber Minichiller. The photocatalyst (20 mg) was dispersed in either 50 ml of 7.78×10^{-5} M aqueous 4-chlorophenol and 50 ml of 4.2×10^{-2} mM aqueous bisphenol A as the pollutant source by 7-minute ultrasonication in the dark and stirred for a subsequent 120 minutes in the dark to reach equilibrium in molecular adsorption. For both reactor setups, aliquots (1 ml) were periodically withdrawn from the reaction mixture for analysis and the UV-Visible spectrophotometer used for absorbance spectra was Perkin Elmer Lambda 35. Post-reaction catalysts were separated by centrifugation at 8000 RPM for 10 minutes, and then vacuum dried and stored in a vacuum desiccator for characterisation.

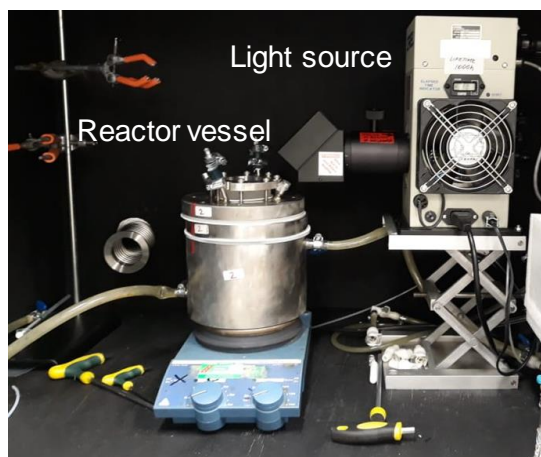


Figure 2.5 Picture of the reactor vessel used for photodecomposition of pollutants.

2.3.2. Hydrogen evolution

Photocatalytic H₂ production was performed in a sealed quartz photoreactor (384 ml volume) with a 200 W Hg-Xe arc lamp (Oriel Instruments 66002) and 420 nm cut-off filter to remove UV light; the light intensity inside the reactor was 16.7 mW.cm⁻². In Chapter 5, the photocatalyst (20 mg) was dispersed in 45 ml water with 5 ml methanol as a sacrificial hole scavenger and sonicated for 5 minutes to obtain uniform distribution. In Chapter 6, the photocatalyst (50 mg) mixed with water containing 50 ml of 0.5 M Na₂SO₃ as the hole scavenger and sonicated for 5 minutes to obtain uniform distribution. The photoreactor was then purged with He for 1 hour in the dark to remove dissolved oxygen, prior to visible light irradiation. Aliquots of gas from the reactor headspace were periodically withdrawn during irradiation using a 1 ml gas syringe and injected into a Shimadzu Tracera GC-2010 Plus gas chromatography fitted with a Carboxen1010 capillary column (30 m×0.53 mm×0.1 μm) and barrier ionisation detector (using a He carrier) for gas analysis.

2.3.3. Photoelectrochemical cell (PEC)

The PEC performance of photocatalysts was carried out in a cell, which used a three-electrode setup in a quartz reactor. The electrolyte (0.5 M Na₂SO₄) was deaerated with N₂ gas for 30 minutes, the counter electrode was a Pt wire (which has small overpotential to reduce protons to H₂) and Hg/Hg₂SO₄/H₂SO₄ (0.5M) as a reference electrode. Electrode potential was controlled using a potentiostat (Autolab, PGSTAT12) and recorded versus reversible hydrogen electrode (RHE).

$$E_{RHE} = E_{Hg_2SO_4} + E^0_{Hg_2SO_4} + 0.059 pH \quad (2.13)$$

Where E_{RHE} is the potential versus the reversible hydrogen electrode, $E_{Hg_2SO_4}$ is the potential versus Hg/Hg₂SO₄ reference electrode and $E^0_{Hg_2SO_4}$ is the standard potential of Hg/Hg₂SO₄ reference electrode (0.68 V vs. NHE at 298 K).

Glassy carbon electrode was used as the working electrode with an electrode area of 0.07 cm². The light source was a 200 W Hg-Xe arc lamp, which was kept at the same distance from the quartz reactor for all experiments to maintain 150 mWcm⁻². The working electrode was initially cleaned because it is essential to maintain a clean sample for accurate photocurrent measurements. The procedure to clean the glassy carbon electrode was simple, as an aluminium polishing powder was used with water to clean the electrode. Aluminium powder and water droplets are poured on a cloth surface and the glassy carbon electrode was rubbed against the aluminium powder and water droplets repeatedly to polish the electrode. The photocatalyst sample was prepared as a colloid and drop-casted onto the glassy carbon electrode surface. 10 mg of the photocatalyst is mixed with 0.09 ml ethanol, 0.09 ml water and 20 µL Nafion which is a conductive polymer that helps bind the colloid. Prior to any measurements, the reactor is de-aerated using nitrogen gas, to remove any dissolved oxygen.

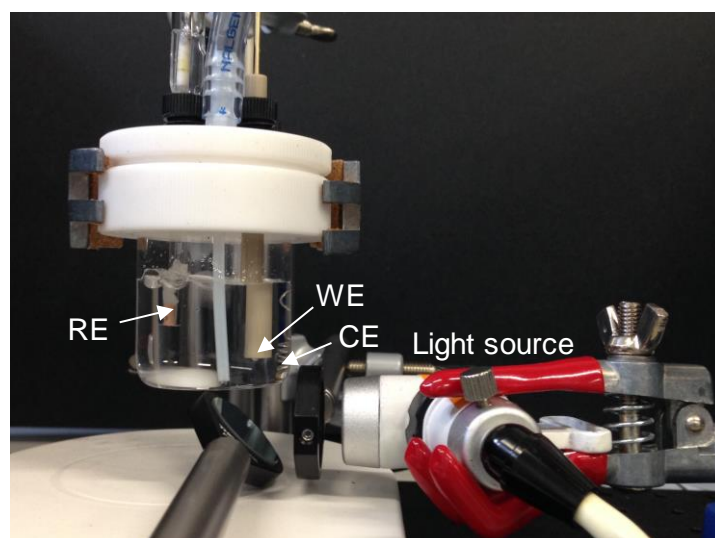


Figure 2.6 Picture of the PEC cell, where RE is Hg/Hg₂SO₄, WE is the photocatalyst drop casted onto glassy carbon electrode, CE is Platinum wire and the light source is 200 W Hg-Xe lamp.

2.4. Apparent Quantum Efficiency (AQE)

The photocatalytic activity for a catalyst is dependent on the experimental conditions, so it is difficult to compare one to another. Hence, apparent quantum efficiency (AQE) is used to compare visible light photocatalytic activity using a band pass filter at 475 nm.

$$\text{AQE (\%)} = \frac{\text{Mol. reacted electrons per unit time}}{N_E} \times 100 \quad (2.14)$$

AQE is the ratio between the percentage of reacted electrons and the number of incident photons, however N_E must be calculated using Equation 2.14.

$$N_E = \frac{N_P}{N} \quad (2.15)$$

Where N_E is the mole incident photons per unit time, N_P is the number of incident photons per unit time and N is the Avogadro's constant.

$$E_P = \frac{hc}{\lambda} = 4.18 \times 10^{-19} \text{ J} \quad (2.8)$$

The photon energy (E_P) is calculated using Equation 2.8; where h is Planck's constant, c is the speed of light and λ is the wavelength using the band-pass filter.

$$N_P = \frac{E}{E_P} = 5.99 \times 10^{16} \text{ s}^{-1} \quad (2.16)$$

N_P is calculated using Equation 2.16, and the value is substituted in Equation 2.15 to obtain N_E . Where N_P is the number of incident photons per unit time, E is the light intensity and E_P is the photon energy.

$$N_E = \frac{N_P}{N} = 9.94 \times 10^{-8} \text{ mol.s}^{-1} \quad (2.15)$$

Therefore, AQE is calculated as follows.

$$\text{AQE (\%)} = \frac{\text{Mol. reacted electrons per unit time}}{9.94 \times 10^{-8}} \times 100 \quad (2.14)$$

2.5. References

1. Bragg, W. L. *The Crystalline State: Volume I.* (New York: The Macmillan Company). **1934**.
2. Hart, M.; Azaroff, V.; Kaplow, R.; Kato, N.; Weiss, R.J.; Wilson, A.J.C.; Young, R.A. *Acta Crystal.* **1975**, *31*, 878.
3. Hollander, J. M.; Jolly, W. L. *Acc. Chem. Res.* **1970**, *3*, 6.
4. Brunauer, S.; Emmett, P.H.; Teller, E. *J. Am. Chem. Soc.* **1938**, *60*, 2.
5. Hanaor, D.A.H.; Ghadiri, M.; Chrzanowski, W.; Gan, Y. *Langmuir.* **2014**, *30*, 50.
6. Tauc, J. *Mat. Res. Bul.* **1968**, *3*, 1.
7. Kubelka, P.; Munk, F. *Zeits. f. Techn. Physik.* **1931**, 12.
8. Gardiner, D.J. *Practical Raman spectroscopy.* **1989**.
9. Yu, J.; Kudo, A. *Adv. Func. Mat.* **2006**, *16*, 16.
10. Peter, L.M. *J. Sol. State Electrochem.* **2013**, *17*, 315.
11. Li, Z.; Wang, W.; Greenham, N.C.; McNeill, C.R. *Phys. Chem. Chem. Phys.* **2014**, *16*, 25684.
12. Memming, R. *Semiconductor Electrochemistry.* (Federal Republic of Germany). **2001**.
13. Gelderman, K.; Lee, L.; Donne, S. W. *J. Chem. Educ.* **2007**, *84*, 4.

Chapter 3

Zero-dimensional carbon enhanced visible light activity of TiO₂

This chapter explores the synthesis of 0D carbon modifications on 1D TiO₂ photocatalysts by hydrothermal treatment. 1D TiO₂/0D carbon was synthesised hydrothermally and different polymorphs of TiO₂ were compared as the semiconductor and gelatine was used as the carbon precursor. The synthesis and characterisation of the photocatalysts were necessary to study their structural properties. Furthermore, the photodecomposition of methylene blue (MB) dye and transient photocurrent responses were investigated to study the activity of the photocatalysts.

3.1. Introduction

The use of semiconductors as photocatalysts have been studied extensively over the last few decades, such as TiO₂¹, ZnO², Cu₂O³, Fe₂O₃⁴ and BiVO₄⁵ but each have limitations. For example, TiO₂ has a high band gap of 3.2 eV which has strong absorbance in UV light and constitutes only 4% of the solar spectrum⁶. Many methods to improve the photocatalytic activity of TiO₂ have been studied, such as the implementation of co-catalysts, doping, heterojunctions and quantum dots^{7,8}. Semiconductor quantum dots were showing toxicological^{8,9} limitations, which caused the emergence of carbon quantum dots (CQDs)¹⁰.

CQDs were discovered by Xu et al.⁹ when they were separating SWNTs and the name ‘carbon quantum dots’ was introduced by Sun’s group¹¹. CQDs are quasi spherical nanoparticles comprised of amorphous to nanocrystalline cores with graphitic or turbostratic carbon (sp² carbon) fused by sp³ hybridised carbon¹², as shown in Figure 3.1.

CQDs were investigated as they have unique electrical, chemical and mechanical properties¹³ to enhance photocatalysts. The synthesis of low-dimensional carbon is used as a method to improve and modify bare photocatalysts, as CQDs have low cytotoxicity, high conductivity, photostability and good biocompatibility¹⁴.



Figure 3.1 Structure of CQDs, retrieved from reference¹².

As studied in the literature, Li et al.¹⁵ learned that CQDs/TiO₂ nanosheets (TNS) degraded over 90% more Rhodamine B dye than bare P25 under visible light irradiation and the photocurrent response of CQD/TNS was 2.8 $\mu\text{A}/\text{cm}^2$ compared to 0.1 $\mu\text{A}/\text{cm}^2$ of TNS. The group proposed a schematic where CQDs absorbed visible light and then emitted light with short wavelength that excites TiO₂ to form electron-hole pairs, which was a mechanism called upconversion. As TiO₂ interacted with CQD, the position of CQDs band edge promoted charge transfer from TiO₂ surface, enhancing charge separation and hindering recombination.

Recent research studied both photoelectrochemical and photo-oxidative potential of CQDs/photocatalysts which showed enhanced performance in both areas with the addition of CQDs. This was attributed to higher charge transfer and separation of electron-hole pairs in CQDs/TiO₂, as well as upconversion properties¹⁶.

3.2. Catalyst synthesis

3.2.1. TiO₂-A nanofibers (NF)

Single crystalline 1D TiO₂-A NF 810 °C for 2 hours were fabricated similarly to previous reports via topotactic transformation by ion exchange and dehydration¹⁷. Potassium

dititanate ($K_2Ti_2O_5$) was prepared by adding K_2CO_3 (reagent grade potassium carbonate) to $TiO_2 \cdot nH_2O$ and then sintered at $810\text{ }^\circ\text{C}$ for 2 hours. $K_2Ti_2O_5$ was hydrated by adding water, ion-exchange was carried out with HCl aqueous solution (0.5 mol/l) to form hydrated titanate ($H_2Ti_2O_5$). The product was filtered and washed with distilled water and dried in an oven at $60\text{ }^\circ\text{C}$ under vacuum. The residual K^+ in the final product that should be less than 0.2 wt.%. The $H_2Ti_2O_5$ was calcined in a muffle oven at $500\text{ }^\circ\text{C}$ for 2 hours to obtain anatase TiO_2 .

3.2.2. TiO_2 -B nanofibers (NF)

$K_2Ti_2O_5$ was prepared by adding K_2CO_3 (reagent grade) to $TiO_2 \cdot nH_2O$ and then sintered at $810\text{ }^\circ\text{C}$ for 2 hours. After that, 2 g of $K_2Ti_2O_5$ was mounted on a crucible with 20 ml of deionised water under the crucible, and then sealed in a Teflon-lined autoclave. It was placed in an oven at the temperature of $180\text{ }^\circ\text{C}$ to conduct steam thermal hydration treatment for a set duration of 12 hours, and then cooled to room temperature. The intermediate was obtained after ion exchange in vigorously stirred 0.1 M HCl solution until K^+ ion was completely exchanged. The intermediate was filtered and washed with distilled water and then dried in a desiccator at $80\text{ }^\circ\text{C}$, and then in a muffle oven at $500\text{ }^\circ\text{C}$ in air for 2 hours to obtain TiO_2 -B NF.

3.2.3. TiO_2 -B microparticles (MP)

2 g of $K_2Ti_2O_5$ was mounted on a crucible and then with 20 ml of deionised water under the crucible was sealed in a Teflon-lined autoclave. It was placed in an oven at the temperature of $120\text{ }^\circ\text{C}$ to carry out steam thermal hydration treatment for a set duration of 72 hours, and then cooled to room temperature. The intermediate was obtained after ion exchange in vigorously stirred 0.1 M HCl solution until K^+ ion was completely exchanged. The intermediate was filtered and washed with distilled water and then dried in desiccator at $80\text{ }^\circ\text{C}$, and then calcined in a muffle oven at $500\text{ }^\circ\text{C}$ in air for 2 hours to obtain TiO_2 -B MP.

3.2.4. TiO₂/CQDs

TiO₂/CQDs were synthesised using a hydrothermal treatment, where the reagents are placed in a Teflon-lined autoclave. The 50 ml volume autoclave consists of a Teflon liner, corrosion disc and bursting disc. The contents to fabricate TiO₂/G (1:1 ratio) (20 ml water, 40 mg catalyst and 40 mg gelatine as carbon precursor) are heated in an oven at 200°C for 3 hours, similarly to literature¹⁸. At the end of the hydrothermal treatment, the autoclave is left to cool at room temperature. The solid sample was separated by centrifugation and several washes with water were conducted at 8000 RPM for 10 minutes each and left to dry overnight. Gelatine (G) was used as the carbon precursor as it is used in literature as a coating agent with metal nanoparticles¹⁹, and different weight loadings were investigated (TiO₂: G ratios: 1:1, 5:1, 10:1, 1:5 and 1:10).

3.3. Characterisation

3.3.1. TiO₂-A NF

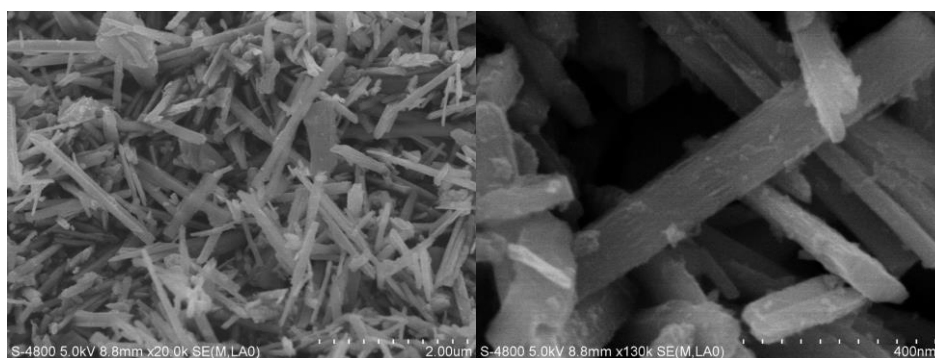


Figure 3.2 SEM images of TiO₂-A NF.

The morphology of TiO₂-A NF is shown in Figure 3.2. In the cluster of TiO₂, the diameter of TiO₂ nanofibers were approximately 100-200 nm and lengths between 2-10 µm. A

variety of TiO₂ lengths and widths show a disoriented cluster of TiO₂. There is a large polycrystalline structure of TiO₂, with many small crystallites in the form of nanofibers.

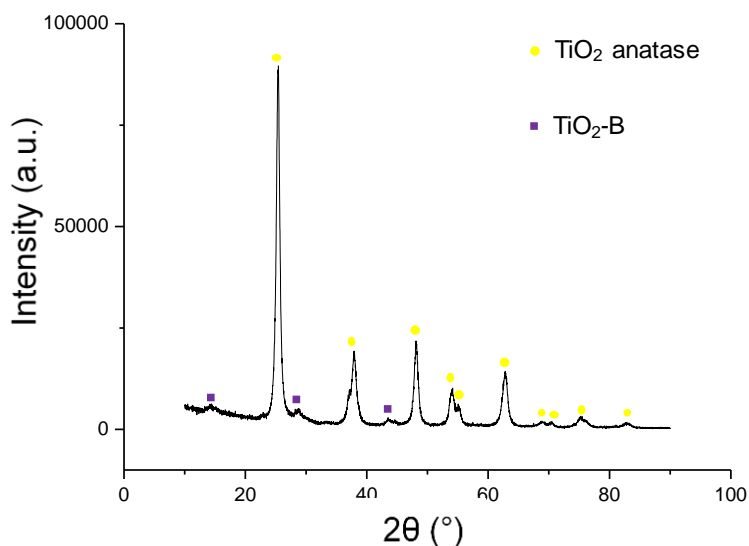


Figure 3.3 XRD pattern of TiO₂-A NF.

The XRD pattern of TiO₂-A NF is shown in Figure 3.3, where the diffraction peaks match TiO₂ anatase phase²⁰. The anatase peaks are well defined and correspond to the crystal planes (101), (004), (200), (105), (211) and (204) at $2\theta = 25^\circ$, 38° , 48° , 53° and 62° respectively. This shows that TiO₂-A NF is of anatase polymorph (tetragonal, JCPDS 21-1272)²¹, but there are also low intensity traces of TiO₂-B NF at 14° , 29° and 44° which corresponds to monoclinic TiO₂-B phase (JCPDS 35-0088)²².

3.3.2. TiO₂-B NF

SEM images of TiO₂-B NF are shown in Figure 3.4. 1D structure of TiO₂-B were successfully synthesised, with a diameter between 100 nm and length between 1-10 μm . In this structure, there is a large polycrystalline TiO₂ seed with many small TiO₂ crystallites. Furthermore, cuboid-like nanofibers are clearly illustrated.

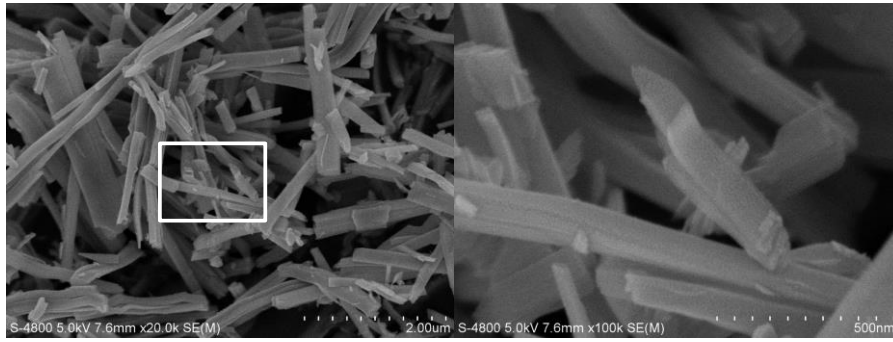


Figure 3.4 SEM images of TiO₂-B NF.

The XRD pattern of TiO₂-B NF matches well with monoclinic TiO₂-B phase, as shown by strong (001), (002), (311) and (003) peaks at $2\theta = 14^\circ$, 29° , 33° and 44° respectively (JCPDS 35-0088)²¹. The broadening of the diffraction peaks is due to the smaller nanosized TiO₂-B NF²³. There are low intensity peaks of anatase (tetragonal, JCPDS 21-1272)²² at $2\theta = 25^\circ$, 38° , 48° and 53° , of which relatively high intensity of (101) plane at 25° is notable.

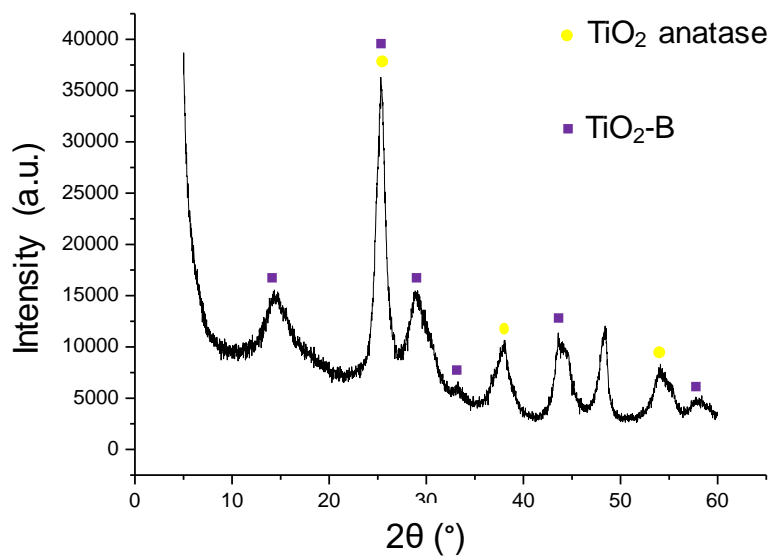


Figure 3.5 XRD pattern of TiO₂-B NF.

3.3.3. TiO₂-B MP

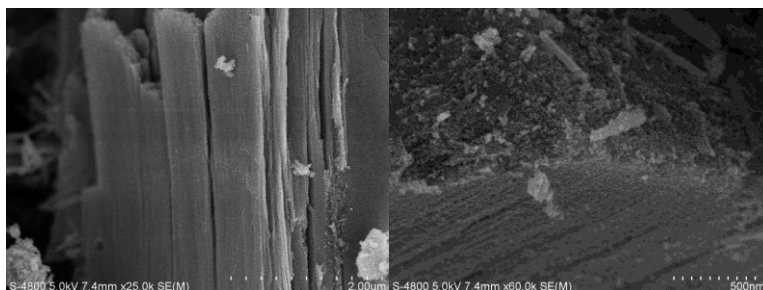


Figure 3.6 SEM images of TiO₂-B MP.

The morphology of TiO₂-B MP is shown in Figure 3.6. The length and width of this structure is in the region of 5-20 μm . Figure 3.7 shows the XRD pattern of TiO₂-B MP had a much lower intensity than the previous two catalysts, which may have contributed to a less smooth response. The diffraction peaks were dominated in the TiO₂-B phase with minor peaks in the anatase phase (tetragonal, JCPDS 21-1272)²². TiO₂ anatase peaks were identified at $2\theta = 25^\circ$ and 48° . Furthermore, the other peaks are indicative of monoclinic TiO₂-B (JCPDS 35-0088)²¹, as shown by peaks at $2\theta = 15^\circ, 25^\circ, 29^\circ$ and 44° for (001), (101), (002) and (003) planes respectively.

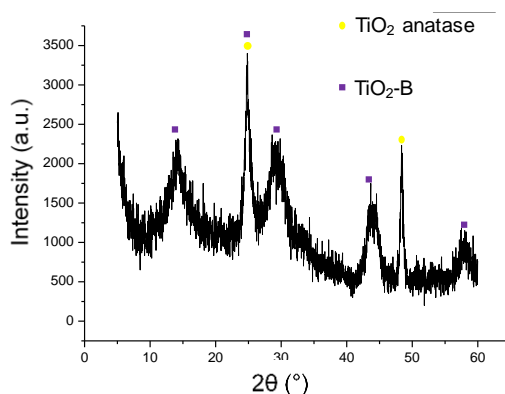


Figure 3.7 XRD pattern of TiO₂-B MP.

3.3.4. General characterisation

Raman spectroscopy was used to confirm the different polymorph of photocatalysts, as illustrated in Figure 3.8. The band positions and intensities of TiO₂-B NF and MP were comparable to literature²⁴, as several active modes for TiO₂-B are shown with major peaks at 195 cm⁻¹, 243 cm⁻¹, 470 cm⁻¹ and 640 cm⁻¹. The highest intensity peak for all three photocatalysts at 150 cm⁻¹ were attributed to anatase. In contrast, the anatase photocatalyst has narrower Raman lines with peaks at 145 cm⁻¹, 192 cm⁻¹, 395 cm⁻¹, 519 cm⁻¹ and 636 cm⁻¹, agreeable with literature²⁵, but there is a TiO₂-B peak at 243 cm⁻¹. The results here suggest that the catalysts are not pure anatase or TiO₂-B, i.e. they have mixed phases, which is consistent with the XRD patterns.

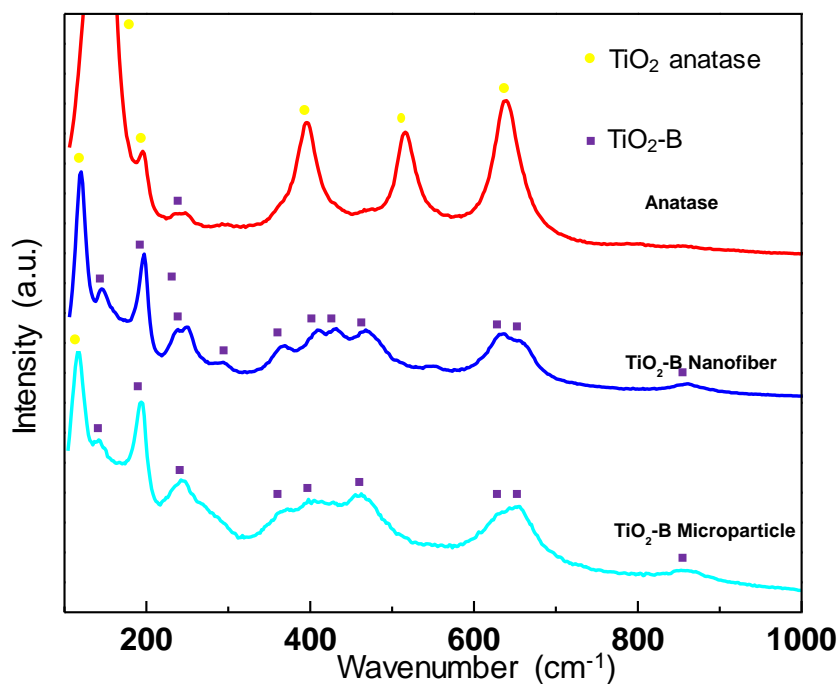


Figure 3.8 Raman spectra of TiO₂-Anatase NF, TiO₂-B NF and TiO₂-B MP.

TGA analysis is necessary to confirm if carbon has successfully integrated with TiO₂. Figure 3.9 shows the weight loss occurred in three steps: the initial step was a 0.8% weight

loss below 100 °C, which was due to adsorbed moisture. The second step occurred at 250 °C with 5.5% weight loss, which was attributed to the decomposition of gelatine polypeptide chains²⁶. A further 2.9% weight loss occurred at 380 °C due to the combustion of carbon, hence the carbon loss in TiO₂-A NF/CQDs is approximately 8.4%.

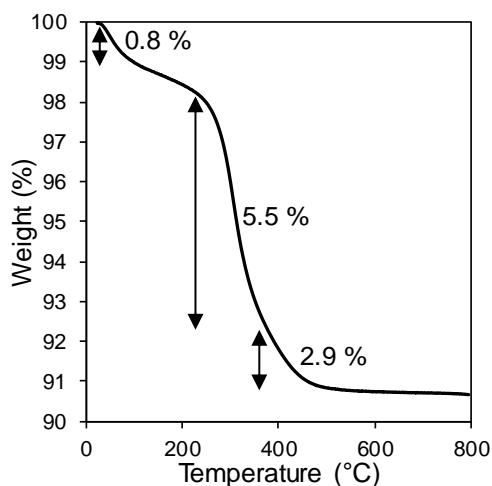


Figure 3.9 Thermogravimetric analysis (TGA) of TiO₂-A NF/CQDs.

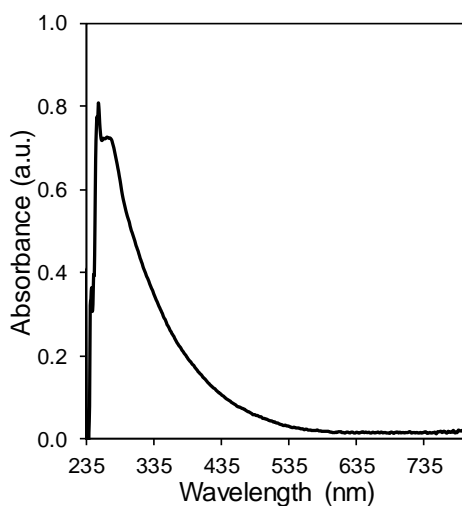


Figure 3.10 UV-Vis spectra of carbon quantum dots (CQDs).

As shown in Figure 3.10, the UV-visible spectra of CQDs is in line with literature as there is a peak at 240 nm, which is due to either aromatic π system or $n-\pi^*$ transition (C=C and carbonyl/hydroxyl groups)¹⁸. The broad absorbance peaks at $\lambda < 435$ nm suggests CQDs cannot promote visible light activity effectively. From the characterisation, carbon was identified in the photocatalyst by TGA, but UV-Vis spectra showed most of the catalysts' absorbance lies below 435 nm which means it will not efficiently capture visible light.

3.4. Photodecomposition of methylene blue dye

Each photocatalyst decomposed MB dye in a one-hour period with the full spectrum of the lamp and using a UV-cut off filter, which blocks light at $\lambda < 420$ nm (labelled as (F)). This was necessary to investigate visible light activity of the synthesised photocatalysts. A blank run was recorded before each experiment set, which means the dye was irradiated without using any photocatalysts. The reactor was set up as described in Section 2.3.1.

3.4.1. TiO₂-A nanoparticles (NP)

Commercial TiO₂ nanoparticles were used in the initial photo-oxidation reactions as a standard to compare with fabricated photocatalysts. TiO₂-A NP are in the anatase phase with an average particle size of 25 nm. The results for all the photodecomposition reactions measure the decomposition efficiency versus time. A blank run consisted of the dye and lamp in absence of the photocatalyst. A filter was used to cut-off light with $\lambda < 420$ nm to examine the visible light activity of the photocatalysts. As shown in Figure 3.11, there is a vast difference in decomposition efficiency of TiO₂-A NP with and without the cut-off filter (33%) which shows that majority of the decomposition of methylene blue dye using TiO₂-A NP occurred below 420 nm. This was also the case for TiO₂-A NP/CQD with a smaller difference of 15% decomposition efficiency, which shows that the integration of CQDs affected the visible light activity as the range in photodecomposition with and without the cut-off filter decreased by 18%.

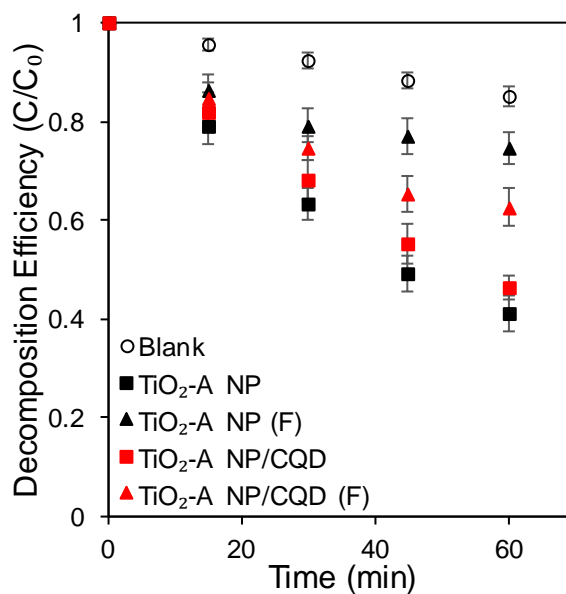


Figure 3.11 Photodecomposition of MB dye using TiO₂-A NP.

3.4.2. TiO₂-A NF

In Figure 3.12, there were contrasting results compared to TiO₂-A NP. TiO₂-A NF confirmed similar decomposition efficiencies under both full spectrum and using UV cut-off filter, with 40% and 35% decomposition respectively. This low decomposition rate of bare TiO₂-A NF suggested limited photocatalytic activity, so with CQD integration the photodecomposition of MB dye was improved greatly, as TiO₂-A NF/CQD decomposes 65% of MB dye with the UV cut-off filter and 68% under the full spectrum. This indicates that CQDs play a vital role in enhancing the photocatalytic activity of TiO₂-A NF/CQD. In addition, the increase in photocatalytic activity of TiO₂-A NF is presumed to be caused by upconversion properties, as CQDs can absorb photons with longer wavelength and emit shorter wavelength photons that can excite TiO₂-A NF to form electron-hole pairs. These electron hole pairs react with adsorbed oxygen and water to form O₂ and OH, which produces various oxygen radicals O²⁻ and •OH which causes photodecomposition of MB dye²⁷.

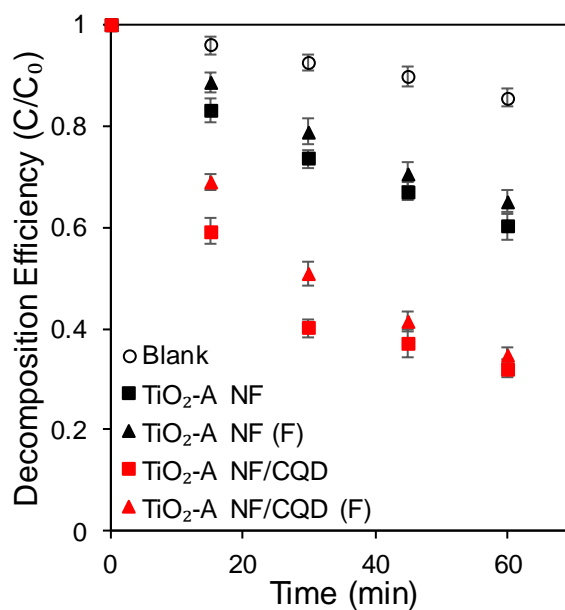


Figure 3.12 Photodecomposition of MB dye using TiO₂-A NF.

3.4.3. TiO₂-B NF

MB dye was decomposed using TiO₂-B NF under irradiation, illustrated in Figure 3.13. TiO₂-B NF decomposed 45% of MB dye under full spectrum and 40% with a UV cut-off filter, which suggests there was most activity in the visible light region of the spectrum. When hybridised with CQDs, TiO₂-B NF/CQD has superior decomposition of MB dye. 70% of MB dye is decomposed in an hour with TiO₂-B NF/CQD under full spectrum and 68% in visible light. The photodecomposition of MB dye using TiO₂-B NF/CQD shows that CQDs minimise the difference with and without the cut-off filter.

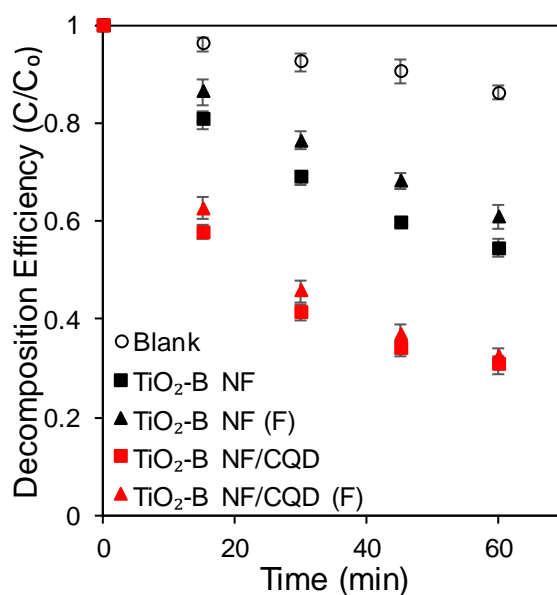


Figure 3.13 Photodecomposition of MB dye using TiO₂-B NF.

3.4.4. TiO₂-B MP

In comparison to TiO₂-A NF and TiO₂-B NF, TiO₂-B MP decomposed MB dye at a much slower rate in both full spectrum (46% decomposed) and visible light (32% decomposed), demonstrated in Figure 3.14. Large particle size and lack of structural modification illustrated low photodecomposition rates. TiO₂-B MP decomposed 46% of MB dye under full spectrum and only 32% MB dye in visible light. After the integration of CQDs, TiO₂-B MP/CQD decomposed 54% MB dye under full spectrum and 45% in visible light. Therefore, CQDs had a positive effect on TiO₂-B MP by increasing the activity in both regions of the solar spectrum.

This suggests that a larger particle size distribution (using microparticles) influences photocatalytic activity, as the other two samples contain nanosized fibers. Nanosized photocatalysts have superior electron transfer and form hydroxyl radicals much easier. This leads to an enhanced photocatalytic activity, which agrees with the literature²⁸. In addition, it was proposed that large microparticles may hinder effective CQD loading on the TiO₂ surface. So, it is evident that photocatalyst particle size also affects photocatalytic activity.

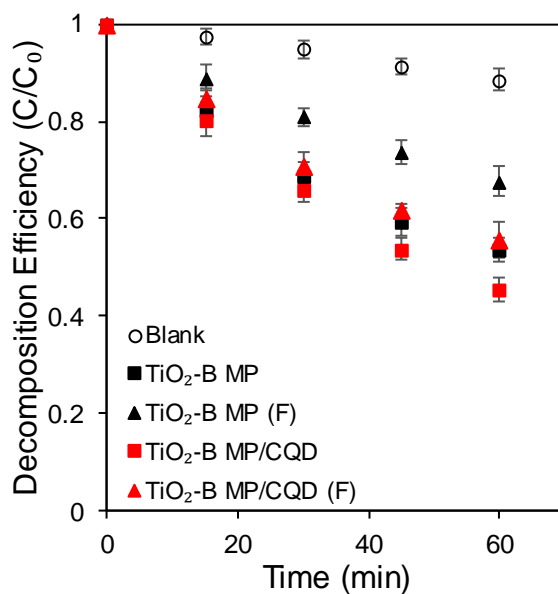


Figure 3.14 Photodecomposition of MB dye using TiO₂-B MP.

3.4.5. Carbon loading

TiO₂-B NF was used as the reference catalyst to test different carbon weight loading for CQDs, as shown in Figure 3.15. There were differences in using different carbon weight loading, as there was a difference of 20% MB dye decomposition range between the photocatalysts. Both 5:1 and 10:1 loading did not decompose dye efficiently in visible light, which is supported by the previous results as there is lack of CQDs in the catalyst. Hence, TiO₂-B/G (1:5) had superior photocatalytic activity which is due to the increased concentration of CQDs in the sample. However, TiO₂-B/G (1:10) performed worse than those with less CQD loading, which is assumed to relate to agglomeration because higher loading of CQDs results in competition for visible light absorption between graphite and MB dye so the amount of visible light decomposition decreases¹⁶.

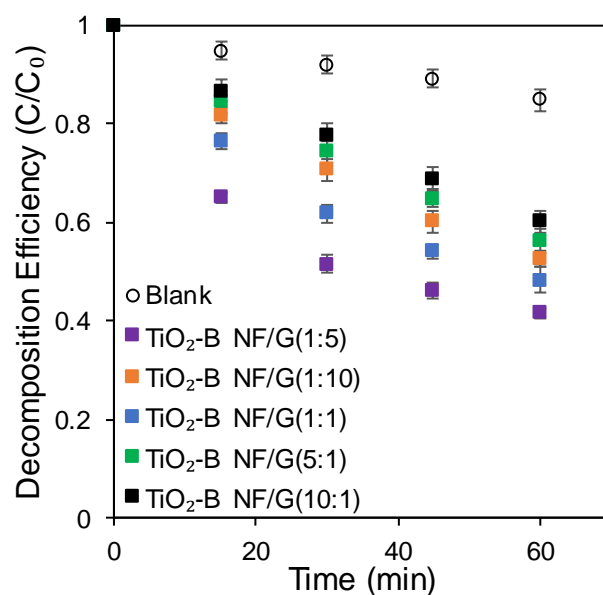


Figure 3.15 Visible light photodecomposition of MB dye using different carbon loading.

3.5. Transient photocurrent analysis

3.5.1. TiO₂-A NP

Figure 3.16 illustrates transient photocurrent measurements, which relate to the photoelectroactivity as light is pulsed onto the electrode and a photocurrent is recorded. The photocurrent quantifies the electron-hole activity in the working electrode. TiO₂-A NP had a photocurrent of 3.3 $\mu\text{A}/\text{cm}^2$ and 0.7 $\mu\text{A}/\text{cm}^2$, under full spectrum and with the UV cut-off filter. This suggests the visible light activity of bare TiO₂-A NP is very low, which is relatable with the photodecomposition results. With the integration of CQDs onto TiO₂-A NP the photocurrent increased slightly, as the photocurrent was 4.1 $\mu\text{A}/\text{cm}^2$ under full spectrum and 1.3 $\mu\text{A}/\text{cm}^2$ using the cut-off filter, which is agreeable with literature²⁹. It is important to note that the integration of CQDs increases the photocurrent response under full spectrum.

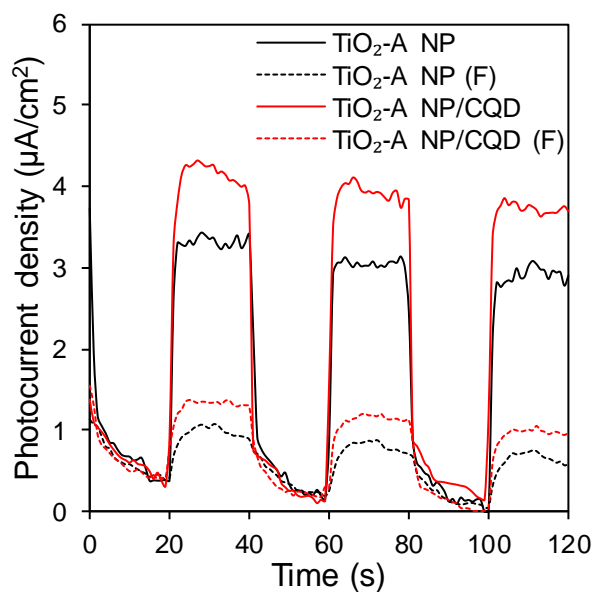


Figure 3.16 Transient photocurrent of TiO₂-A NP at 0 V vs. RHE.

3.5.2. TiO₂-A NF

Figure 3.17 shows transient photocurrent measurements of TiO₂-A NF. There was an increase in transient photocurrent response compared to TiO₂-A NP, which is attributed to 1D nanofibers. However, the photocurrent of TiO₂-A NF was lower than TiO₂-A NF/CQD, both in visible light and full spectrum. TiO₂-A NF exhibited a photocurrent of 3.2 µA/cm² and 0.7 µA/cm², under full spectrum and visible light respectively. In comparison, TiO₂-A NF/CQD exhibited a photocurrent of 5.2 µA/cm² and 1.1 µA/cm², under full spectrum and visible light respectively. These results suggest the hybridisation of CQDs effectively increased the photoresponse, with a higher photocurrent of TiO₂-A NF/CQD. This indicates TiO₂-A NF/CQDs exhibit higher transfer and separation efficiency of photogenerated electron-hole pairs¹⁶. In addition, the sharp peak of TiO₂-A NF/CQD indicates more efficient transport of photogenerated electrons into TiO₂-A NF. Similarly to the activity of TiO₂-A NP, the integration of CQDs in TiO₂-A NF increases the photocurrent response under full spectrum.

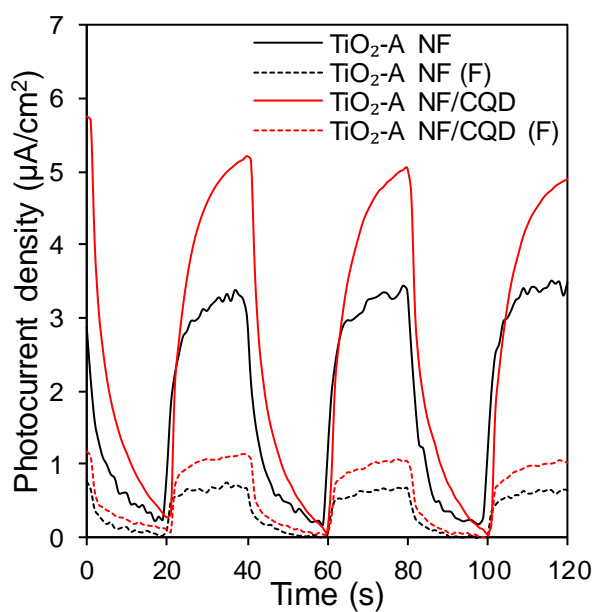


Figure 3.17 Transient photocurrent of TiO₂-A NF at 0 V vs. RHE.

3.5.3. TiO₂-B NF

The transient photocurrent of TiO₂-B NF (Figure 3.18) was 1.3 $\mu\text{A}/\text{cm}^2$ under full spectrum and 0.6 $\mu\text{A}/\text{cm}^2$ in visible light. In contrast, TiO₂-B NF/CQD had a photoresponse of 2.4 $\mu\text{A}/\text{cm}^2$ under full spectrum and 1.0 $\mu\text{A}/\text{cm}^2$. This shows that CQDs improved the visible light activity, due to enhanced photogenerated electron and hole separation. In this case, the visible light activity of TiO₂-B NF/CQD is similar to TiO₂-B NF in the full spectrum, even though the overall photocurrent density is lower than other photocatalysts.

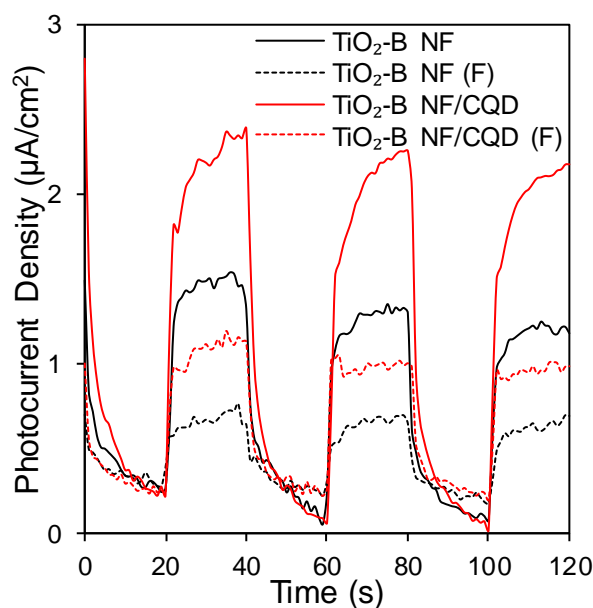


Figure 3.18 Transient photocurrent of TiO₂-B NF at 0 V vs. RHE.

3.5.4. TiO₂-B MP

TiO₂-B MP exhibited the weakest photocurrent in both full spectrum and visible light region, illustrated in Figure 3.19. There was a minor difference in pure TiO₂-B MP and TiO₂-B MP/CQD, because the difference in photocurrent between the two photocatalysts was 0.3 µA/cm² and 0.1 µA/cm², under full spectrum and visible light respectively. This suggests that CQDs had an insignificant effect on the transient photocurrent because TiO₂-B MP has a much larger particle size. In contrast to the other photocatalysts, TiO₂-B MP/CQD exhibited the highest activity under full spectrum (1.1 µA/cm²) but with the UV cut-off filter the activity was the lowest at 0.25 µA/cm². This indicates that the interaction between CQDs and microparticles improved the photocurrent response of CQDs in UV light.

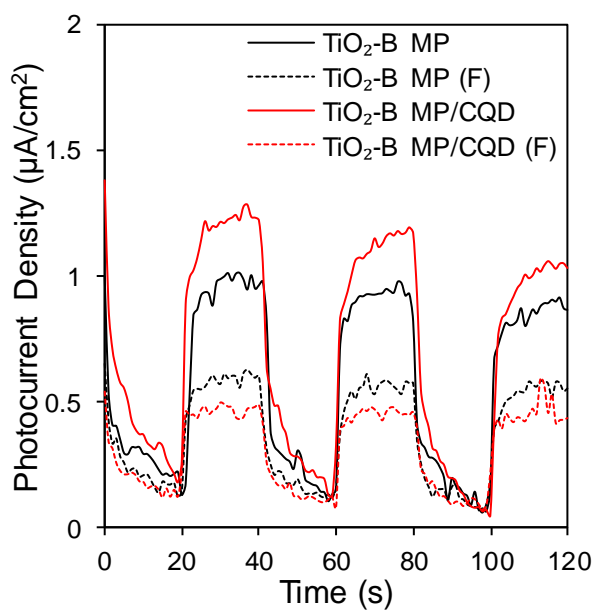


Figure 3.19 Transient photocurrent of TiO₂-B MP at 0 V vs. RHE.

3.5.5. Carbon loading

Figure 3.20 shows TiO₂-A NF as the reference catalyst used to test different carbon weight loadings to study visible light activity. Both 10:1 and 1:10 carbon weight loading demonstrated the weakest photocurrents. TiO₂-A NF/G 5:1, 1:1 and 1:5 display much higher photocurrent results (minimum 1 µA/cm²). TiO₂-A NF 5:1 and 1:1 have higher photocurrent than 1:10 and 10:1 as there is enough carbon dots in the catalyst but they are not agglomerated so there is enhanced activity (as mentioned in Section 3.4.5). TiO₂-A NF/G (1:5) exhibited the visible light photocurrent because there is efficient amount of carbon dots on the 1D nanofibers.

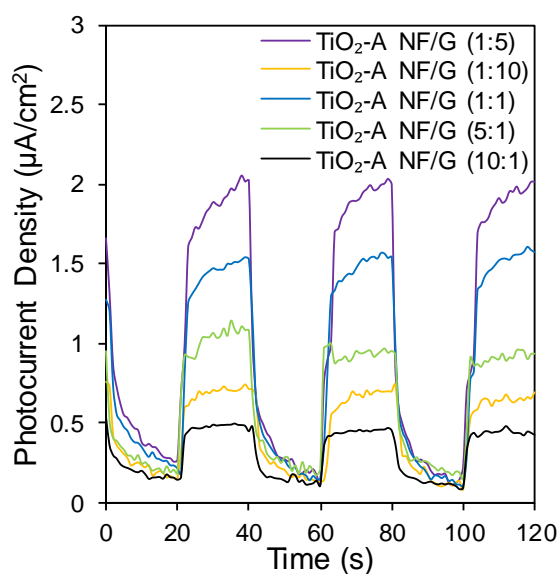


Figure 3.20 Visible light transient photocurrent with different carbon loading at 0 V vs. RHE.

3.6. Conclusions

In conclusion, TiO₂/CQDs were successfully synthesised using different polymorphs of TiO₂, which included TiO₂-A, TiO₂-B and TiO₂-MPs. The photodecomposition of MB dye and transient photocurrent responses were carried out to demonstrate enhanced photocatalytic activity of TiO₂/CQDs.

In the photodecomposition of MB dye, the interaction between 1D semiconductor and 0D carbon in TiO₂-NF/CQDs were shown to have superior photocatalytic activity. This was attributed to the large surface area of nanofibers and fast electron transfer in a 1D nanostructure, which promotes the efficient separation of electron-hole pairs. In addition, the increase in photocatalytic activity of TiO₂/CQDs was presumed to be caused by upconversion properties of CQDs, as CQDs can absorb photons with longer wavelength and emit shorter wavelength photons that can excite TiO₂ to form electron-hole pairs. These electron hole pairs react with adsorbed oxygen and water to form O₂ and OH⁻, which produces various oxygen radicals O²⁻ and •OH causing the photodecomposition of MB

dye²⁷. After analysing the effect of carbon loading on TiO₂-A NF/G, 1:5 weight ratio decomposed MB dye most efficiently at 60% degradation after 1 hour under visible light irradiation. A higher weight ratio (1:10) decomposed MB dye less efficiently (47%) in visible light irradiation, which was due to the fact graphite in CQDs can also absorb light so there is competition for visible light absorption between graphite and MB dye¹⁶.

The transient photocurrent reactions measured the transfer and separation efficiency of photogenerated electrons and holes in the working electrode. There were only slight increases in photocurrent response in the visible light spectrum, as TiO₂-B NF/CQDs exhibited the highest activity with a twice-fold increase compared to bare TiO₂-B NF. The lack of improved visible light activity with the integration of CQDs in the photodecomposition of pollutants and photocurrent responses were supported by the UV-Vis spectra showing minimal absorbance above 435 nm. This concludes that it is very difficult to promote visible light activity using the fabricated TiO₂/CQDs. As the aim of improving visible light activity could not be reached, there will be no further study on characterising the catalyst, testing hydrogen evolution or photoelectrochemistry.

3.7. References

1. Linsebigler, A.L.; Lu, G; Yates, J.T. *Chem. Rev.* **1995**, *95*, 3.
2. Özgür, Ü.; Alivov, Y.I.; Liu, C.; Alivov, Y.I.; Teke, a.; Reshchikov, M.A.; Doğanc, S.; Avrutin, V.; Cho, S.J.; Morkoç, H. *J. App. Phys.* **2005**, *98*, 4.
3. Sivula, K.; Formal, F.L.; Gratzel, M. *Chem. Sus. Chem.* **2011**, *4*, 4.
4. Kudo, A.; Omori, K.; Kato, H. *J. Am. Chem. Soc.* **1999**, *121*, 49.
5. Ni, M.; Leung, M.K.H; Leung, D.Y.C; Sumathy, K. *Renew. Sus. Ener. Rev.* **2007**, *11*, 3.
6. Fujishima, A.; Zhang, X.; Tryk, D.A. *Surf. Sci. Rep.* **2008**, *63*, 12.
7. Baker, S.N.; Baker, G.A. *Ange. Chemie Int. Ed.* **2010**, *49*, 38.
8. Zheng, X.T.; Ananthanarayanan, A.; Luo, K.Q.; Chen, P. *Small.* **2015**, *11*, 14.
9. Xu, X.; Ray, R.; Gu, Y.; Ploehn, H.J.; Gearheart, L; Raker, K; Scrivens, W.A. *J.Am. Chem. Soc.* **2004**, *126*, 40.
10. Rao, C.N.R.; Muller, A.; Cheetham, A.K. *The Chemistry of Nanomaterials: Synthesis, Properties and Applications*, Wiley, **2004**, 1.
11. Sun, Y.P.; Zhou, B.; Lin, Y.; Wang, W.; Fernando, K.A.; Pathak, P.; Mezziani, M.J.; Haruuff, B.A. et al. *J. Am. Chem. Soc.* **2006**, *128*, 7756.
12. Demchenko, P.; Dekaliuk, M.O. *Methods Appl. Fluoresc.* **2013**, *1*, 42001.
13. Yang, S-T.; Cao, L.; Luo, P.G.; Lu, F.; Wang, X.; Wang, H.; Mezziani, M.J.; Liu, Y.; Sun, Y-P. *J. Am. Chem. Soc.* **2009**, *131*, 32.
14. Li, H.; He, X.; Kang, Z.; Huang, H.; Liu, Y.; Liu, J. et al. *Ange. Chemie Int. Ed.* **2010**, *49*, 26.
15. Yu, X.; Liu, J.; Yu, Y.; Zuo, S.; Li, B. *Carbon.* **2014**, *68*.
16. Zhuang, W.; Lu, L.; Wu, X.; Jin, W.; Meng, M.; Zhu, Y.; Lu, X. *Elec. Comm.* **2013**, *27*.
17. Li, W.; Bai, Y.; Liu, W.; Liu, C.; Yang, Z.; Feng, X.; Lu, X.; Chan, K-Y. H. *J. Mat. Chem.* **2011**, *18*.
18. Yang, H. G.; Zeng, H. C. *J. Phys. Chem. B.* **2004**, *108*.
19. Cui, Q.; He, F.; Wang, X.; Xia, B.; Li, L. *ACS Appl. Mater. Interfaces.* **2013**, *5*.
20. Liu, G.; Qiao, S.Z.; Sun, C.H.; Jin, Y.G.; Smith, S.C.; Zou, J.; Cheng, H.M.; Lu, G.Q. *J. Am. Chem. Soc.* **2009**, *131*, 11.
21. Zúkalová, M.; Kalbáč, M.; Kavan, L.; Exnar, I.; Gratzel, M. *Chem. Mater.* **2005**, *17*, 5.
22. Armstrong, A.R.; Armstrong, G.; Garcia, J.C.R; Bruce, P.G. *Adv. Mater.* **2005**, *17*, 7.
23. Beuvier, T.; Richard-plouet, M.; Brohan, L. *J. Phys. Chem. C.* **2009**, *113*.
24. Ben Yahia, M.; Lemoigno, F.; Beuvier, T.; Filhol, T.S.; Richard-Plouet, M. Brohan, L.; Doublet, M.L. *J. Chem. Phys.* **2009**, *130*.
25. Zheng, F.; Wang, Z.; Chen, J.; Li, S. *RSC Adv.* **2014**, *4*.
26. Bosch, E.V.D.; Gielens, C. *Int. J. of Bio. Macro.* **2003**, *32*, 3.
27. Yu, H.; Zhang, H.; Huang, H.; Liu, Y.; Li, H.; Ming, H.; Kang, Z. *New J. Chem.* **2012**, *36*.
28. Ming, H.; Ma, Z.; Liu, Y.; Pan, K.; Yu, K.; Wang, F.; Kang, Z. *Dalton Trans.* **2012**, *41*.
29. Yen, Y.C.; Lin, C.C.; Chen, P.Y.; Ko, W.Y.; Tien, T.R.; Lin, K.J. *R. Soc. Open Sci.* **2017**, *4*.

Chapter 4

One-dimensional carbon enhanced interparticle charge transfer of TiO₂

In Chapter 4, TiO₂ NF/Cu₂O nanocubes modified by carbon nanowires (C-NWs) were fabricated via hydrothermal and subsequent solution phase chemistry. The C-NWs were prepared using gelatine as the carbon precursor. The nanocomposite with favourable morphology resulted in superior photocurrent density of C-NW/TiO₂ NF/Cu₂O; almost 4 times more than TiO₂ NF. Further results showed C-NW/TiO₂ NF/Cu₂O had enhanced charge transfer and improved photostability. The catalyst interfacial studies and impedance spectra were used to determine energy band structures of the nanocomposite. This study showed the design and preparation of a nanostructured photocatalyst with improved photocatalytic activity, charge transfer and photostability for solar water splitting.

4.1. Introduction

Utilising sunlight to produce chemical fuels with minimal effect on the environment has become an attractive idea over recent decades because it can offer a sustainable alternative to finite energy resources. Solar water splitting is a promising technology that can harvest and convert solar energy to hydrogen fuel. An important factor for improving water splitting systems is obtaining photocatalysts with suitable properties, such as optical absorbance, electron charge transfer and photostability. The use of metal oxides as photocatalysts were studied extensively over the last few decades, such as TiO₂¹, ZnO², Cu₂O³, Fe₂O₃⁴ and BiVO₄⁵, but each have limitations.

Titanium dioxide (TiO₂) is a popular stable n-type semiconductor used over the last few decades, with a large band gap of 3.2 eV¹, thus it is mainly active in the ultraviolet (UV) region, which is 4 % of the solar spectrum. Efforts have been devoted to expanding the spectral response of TiO₂ in the visible light region using various band engineering methods, such as metal doping, co-catalysts and coupling with narrow band gap semiconductors⁶. A highly attractive narrow band gap semiconductor, Cu₂O, is an

abundant, low-cost and non-toxic p-type semiconductor with a band gap between 2.0-2.2 eV⁷. However, Cu₂O is prone to photocorrosion, which is attributed to the oxidation and reduction potential of Cu₂O lying within the band gap⁸. As Cu₂O may potentially have practical issues with photostability, efforts have gone to using carbon in recent years as it is a non-toxic, highly conductive and chemically stable material.

Many properties of photocatalysts such as short charge transfer distance, large surface area, favourable morphology and crystallinity enhance photocatalytic activity. One-dimensional (1D) nanostructured photocatalysts have a large aspect ratio and specific surface area, which are attractive properties in photocatalysis. Moreover, 1D carbon nanostructures are known to have excellent mechanical properties and large specific surface area for superior electron transport⁹. However, little research was reported on 1D carbon nanostructures coupled with semiconductors in a nanocomposite. 1D TiO₂ nanotubes were reported to have distinct advantages of efficient transfer and separation of photogenerated electron-hole pairs and provides many surface reaction sites which is essential for water splitting¹⁰.

Coupling both semiconductors in a heterojunction nanocomposite is an effective method that would increase the absorbance range of TiO₂ and increase photostability of Cu₂O. In heterojunction nanocomposites, there is enhanced separation efficiency of electron-hole pairs as either semiconductor can act as an electron acceptor or donor by band bending. In contrast, it is difficult for a single semiconductor to obtain a narrow band gap and appropriate band positions. Ni et al. reported a p-n heterojunction which had Cu₂O decorated on TiO₂ nanotubes and learned electrons excited under visible light can transfer from the conduction band (CB) of Cu₂O to the CB of TiO₂ as the CB edge for Cu₂O is higher than TiO₂⁵. Therefore, recombination of photogenerated electron-hole pairs can be reduced greatly, which will increase photocatalytic activity.

In this work, we reported a two-step synthesis via topotactic transformation and subsequent hydrothermal synthesis to form C-NW/TiO₂ NF. After, Cu₂O was involved by solution phase chemistry at low temperatures to form C-NW/TiO₂ NF/Cu₂O. This synthesis procedure was simple and required inexpensive solvents and operating conditions. 1D TiO₂ NF and Cu₂O nanocubes were characterised as a nanocomposite and their photophysical properties were explored. Consequently, the photoelectrochemical (PEC) performance of the C-NW/TiO₂ NF/Cu₂O showed superior PEC activity, enhanced stability and improved charge carrier separation.

4.2. Catalyst Synthesis

4.2.1. C-NW/TiO₂ NF

Single crystalline 1D TiO₂ NF were fabricated as described in previous work via topotactic transformation by ion-exchange and dehydration¹¹. Subsequent C-NW/TiO₂ NF were prepared by hydrothermal synthesis using gelatine as the carbon precursor as it is a cheap polymer obtained from animal skin, bones and tissue¹². It is known to have strong coating interactions with metal nanoparticles¹³. Gelatine was dissolved in a mixture of TiO₂ NF in 20 ml water and stirred at 40 °C. The sample was placed in a stainless-steel autoclave and heated at 250 °C for 4 hours. After hydrothermal treatment, the sample was centrifugated at 7,000 RPM for 10 minutes with several washes of water and dried in the oven. Gelatine is abundant in amino and carboxyl groups, so it can be hydrothermally treated with only pure water, hence it is an inexpensive water-soluble polymer. An advantage to this procedure is no strong acid or surface passivation reagent or post-treatment is needed to fabricate C-NW/TiO₂ NF¹⁴.

4.2.2. C-NW/TiO₂ NF/Cu₂O

C-NW/TiO₂ NF/Cu₂O was synthesised by solution phase chemistry under ambient conditions, as described previously⁶. PEG was used as the structuring agent used to fabricate Cu₂O nanocubes and was ultrasonicated in 100 ml water for 30 minutes. C-NW/TiO₂ NF was mixed with 0.2 M CuCl₂ and 0.01 M PEG-600, before ultrasonication for 10 minutes. This mixture was heated to 50 °C, forming a blue solution. 2 M NaOH was poured into the blue solution and 0.2 M N₂H₄·H₂O was added dropwise in the stirred mixture to generate Cu (I) ions and heated for 10 minutes further. The resulting mixture was purged in N₂ to form C-NW/TiO₂ NF/Cu₂O. Centrifugation was necessary at 7000 RPM, with several washes with H₂O and ethanol to remove any residual PEG.

4.3. Characterisation

4.3.1. Microscopy studies

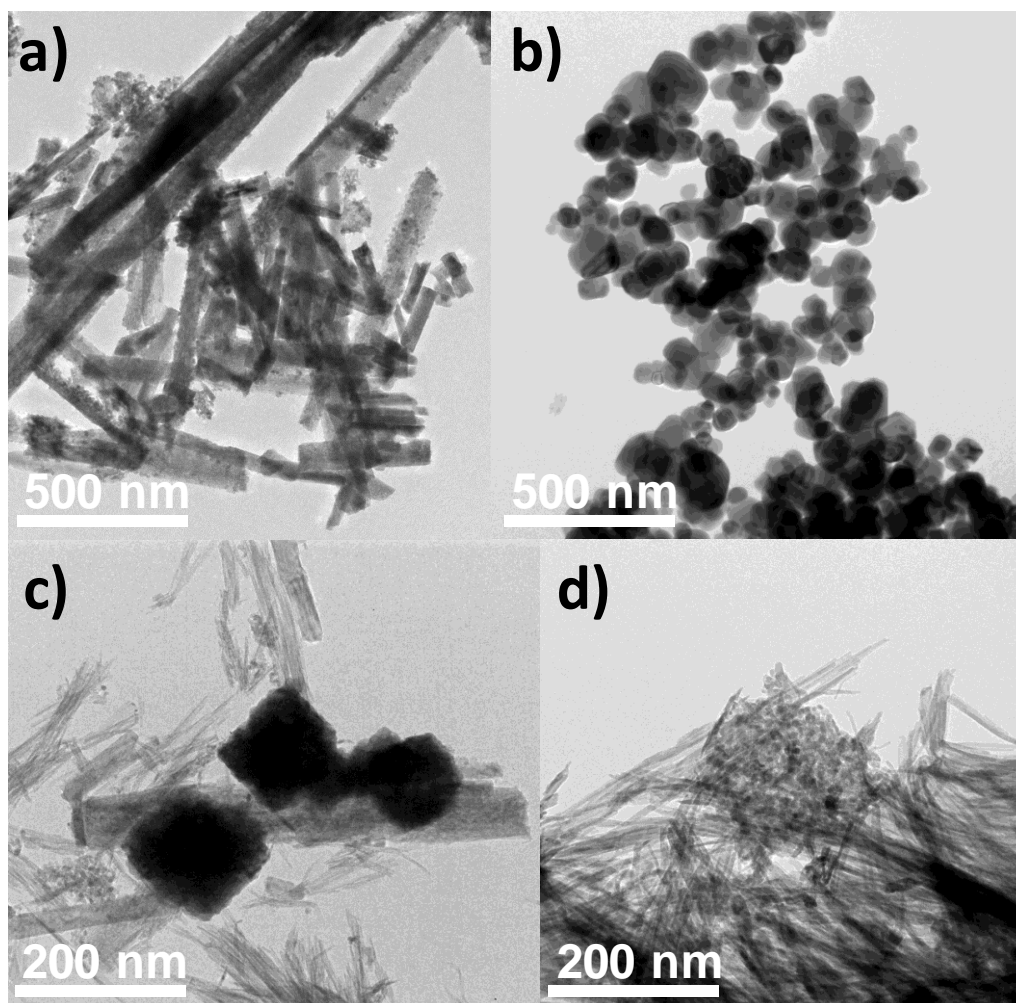


Figure 4.1 TEM images of (a) TiO_2 NF, (b) Cu_2O nanocubes, (c) C-NW/ TiO_2 NF/ Cu_2O , (d) C-NWs.

TEM images showed in-depth morphology and size of C-NW/ TiO_2 NF/ Cu_2O as a nanocomposite in Figure 4.1. Figure 4.1a confirmed the fabrication of 1D TiO_2 NF via

topotactic crystal transformation with lengths between 500 nm – 5 μm and diameters between 100 – 200 nm. Figure 4.1b. illustrated the synthesis of Cu_2O nanocubes with sizes ranging between 150 – 250 nm. After hydrothermal synthesis, a nanocomposite was formed as there was intimate contact between Cu_2O and C-NW/ TiO_2 NF as shown in Figure 4.1c. Furthermore, C-NWs were constructed by pyrolysis of gelatine to small proteins, then hydrolysed to amino acids¹⁴. Amino acids were carbonised with continued hydrothermal treatment to form 1D carbon nanowires, as shown in Figure 4.1d.

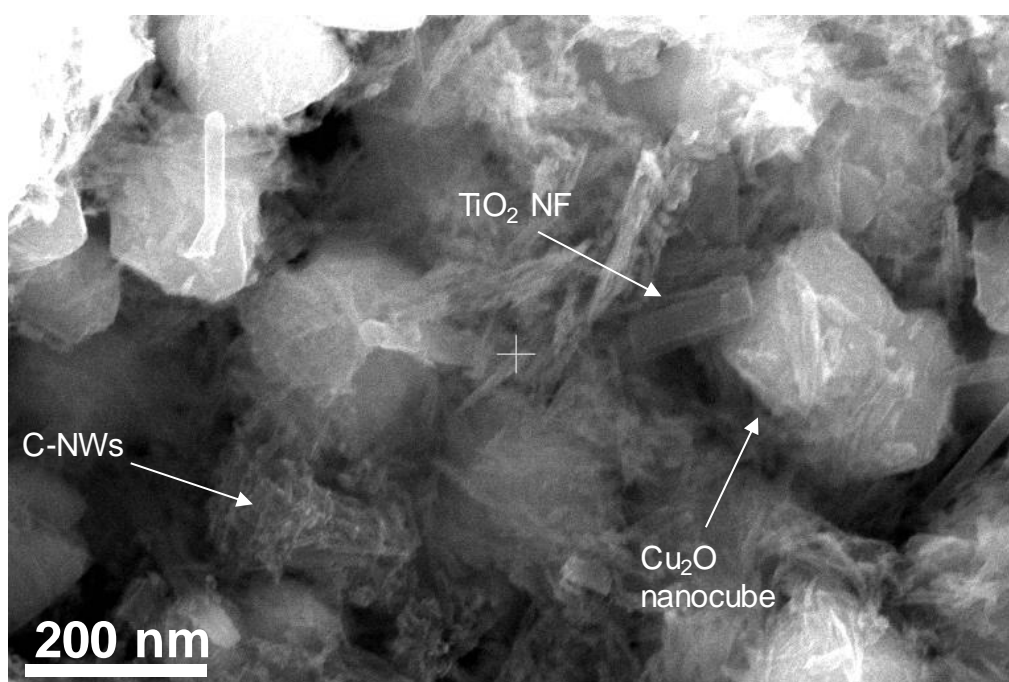


Figure 4.2 SEM image of C-NW/ TiO_2 NF/ Cu_2O .

SEM analysis illustrated the nanocomposite of 1D TiO_2 NF and Cu_2O nanocubes in Figure 4.2. TiO_2 NF were shown to have 1D nanostructured arrays and intimately in contact with Cu_2O nanocubes with sizes that support the TEM images. There is also evidence of C-NWs shown occupying the empty space within the nanocomposite. Figure 4.2 is in good agreement with TEM images of C-NW/ TiO_2 NF/ Cu_2O .

4.3.2. Photophysical properties

XRD patterns confirmed high intensity of Cu_2O peaks and low intensity of TiO_2 peaks in Figure 4.3, indicating that most of the nanocomposite consists of Cu_2O nanocubes, which is consistent with the TEM and SEM images. The diffraction peaks of TiO_2 NF are well defined and correspond to the crystal planes (101), (004), (200), (105), (211) and (204) at $2\theta = 25.3^\circ, 37.8^\circ, 48.0^\circ, 53.8^\circ$ and 62.5° respectively, which suggests anatase TiO_2 NF (tetragonal, JCPDS 21-1272)¹⁵. The XRD patterns illustrate the formation of crystalline Cu_2O by peaks at $29.6^\circ, 36.4^\circ, 42.3^\circ, 61.4^\circ, 73.5^\circ$ and 77.4° associated with characteristic (110), (111), (200), (220), (311), and (222) peaks of Cu_2O (cubic, JCPDS 73-0687)¹⁶. There are weak traces of CuO in both Cu_2O and TiO_2 NF/ Cu_2O , in agreement with JCPDS 45-0937¹⁷. There is a weak but broad pattern at 25° which may suggest either a low concentration of C-NWs or the carbon is very amorphous.

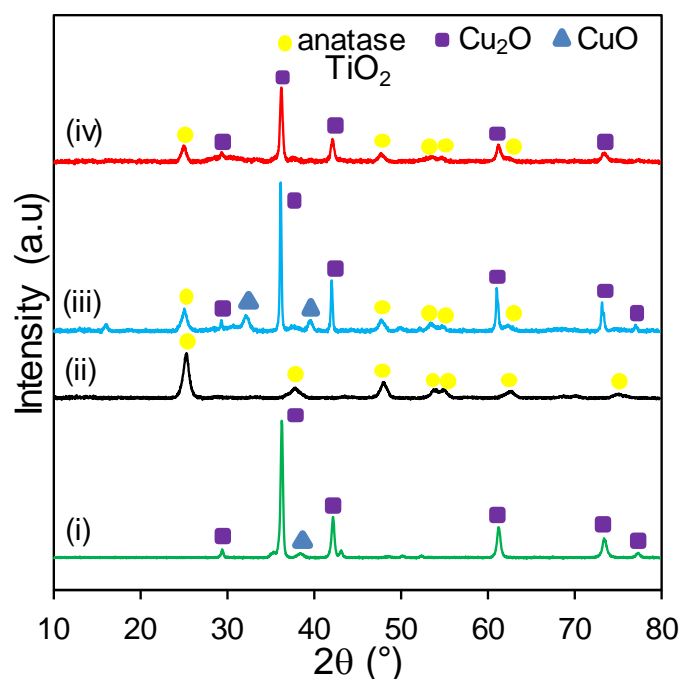


Figure 4.3 XRD patterns of i) Cu_2O , ii) TiO_2 NF, iii) TiO_2 NF/ Cu_2O and iv) C-NW/ TiO_2 NF/ Cu_2O .

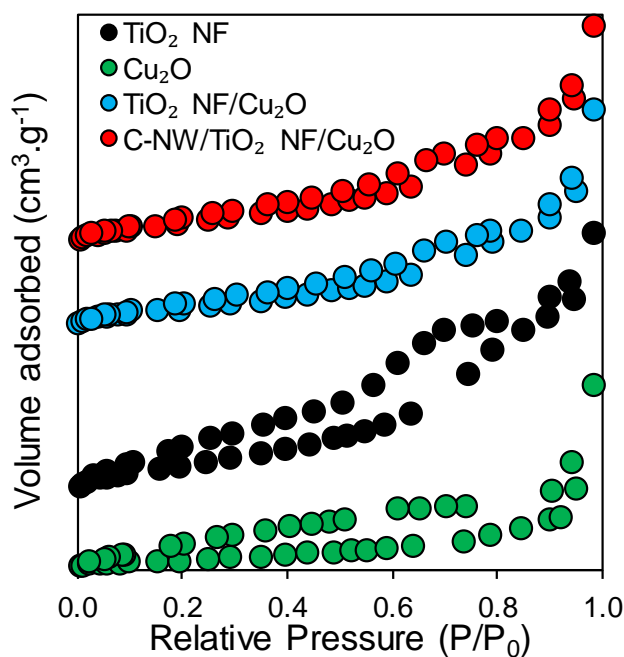


Figure 4.4 N₂ adsorption-desorption isotherms of TiO₂ NF, Cu₂O nanocubes, TiO₂ NF/Cu₂O, C-NW/TiO₂ NF/Cu₂O.

The surface area varied greatly between the photocatalysts (Figure 4.4), but Cu₂O nanocubes had the lowest BET surface area of 22.9 m². g⁻¹. This was higher than Cu₂O nanocubes (4 m². g⁻¹), but similar to hierarchical Cu₂O nanocubes (21 m². g⁻¹)¹⁸. The larger surface area was attributed to smaller particle size, as the synthesised Cu₂O nanocubes were at least 100 nm smaller than others in literature¹⁹. TiO₂ NF exhibited the highest BET surface area of 93.5 m². g⁻¹, consistent with TiO₂ NF produced by electrospinning^{20,21}. C-NW/ TiO₂ NF/Cu₂O had a higher BET surface area than TiO₂ NF/Cu₂O by 13.1 m². g⁻¹, which was due to the integration of C-NWs as it has high surface area. This may have further implications with photocatalytic activity because C-NWs may act as an electron anchor by having improved electron mobility and transportation in the nanocomposite^{22,23}.

The optical properties were analysed in Figure 4.5, where the absorbance spectra ranged from 200 – 600 nm, as previously reported²⁴.

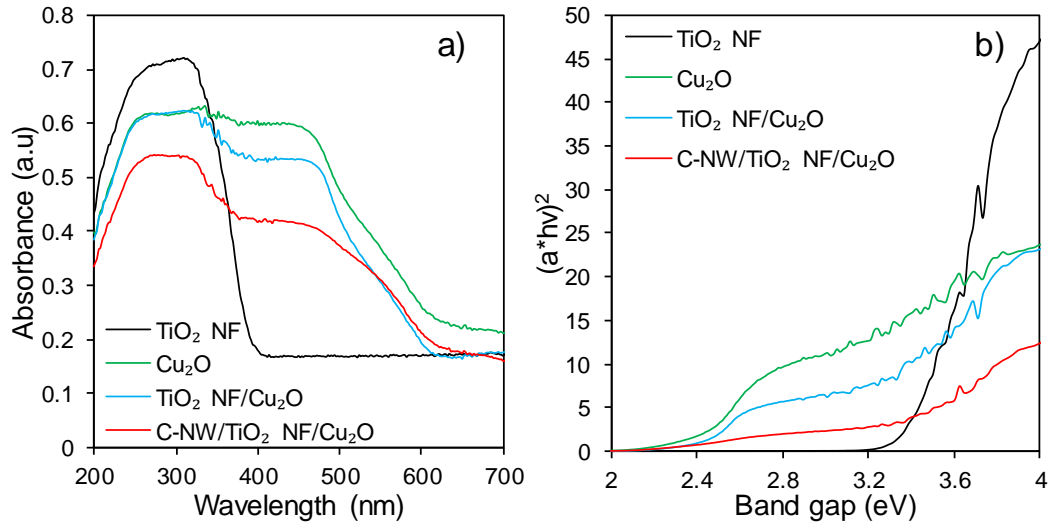


Figure 4.5 a) DRUVS and b) Tauc plots of TiO₂ NF, Cu₂O, TiO₂ NF/Cu₂O and C-NW/TiO₂ NF/Cu₂O.

The optical band gaps E_{BG} were calculated from the Tauc plots (Figure 4.5b) using Equation 2.6.

$$\alpha h\nu = C(h\nu - E_{BG})^n \quad (2.6)$$

Where C is the proportionality constant and α is the absorption coefficient determined from the Kubelka-Munk formula.

$$\alpha = \frac{(1-R)^2}{2R} \quad (2.7)$$

The direct band gaps of TiO₂ NF, Cu₂O, TiO₂ NF/Cu₂O and C-NW/TiO₂ NF/Cu₂O were 3.28, 2.36, 2.38 and 2.21, respectively. The photocatalysts containing Cu₂O absorb light in the visible region, below wavelengths of 650 nm. Two peaks are present at 300 nm and 480 nm, which means the catalyst can be excited at different wavelengths, in agreement with previous reports²⁵. C-NW/TiO₂ NF/Cu₂O showed a red shift to TiO₂ NF/Cu₂O, which indicates C-NWs has strong absorption properties. It may also suggest an increase in

interfacial contact between C-NWs and the semiconductors. The photophysical properties of TiO₂ NF, Cu₂O, TiO₂ NF/Cu₂O and C-NW/TiO₂ NF/Cu₂O were summarised in Table 4.1.

Table 4.1 Photophysical properties of TiO₂ NF, Cu₂O, TiO₂ NF/Cu₂O and C-NW/TiO₂ NF/Cu₂O.

Sample	BET surface area ^a (m ² .g ⁻¹)	Band gap ^b (eV)
TiO ₂ NF	93.5	3.28
Cu ₂ O	22.9	2.36
TiO ₂ NF/Cu ₂ O	53.8	2.38
C-NW/TiO ₂ NF/Cu ₂ O	66.9	2.21

^aN₂ porosimetry and ^bDRUVS

The carbon content in C-NW/TiO₂ NF/Cu₂O was investigated by Thermogravimetric Analysis (TGA), shown in Figure 4.6a, where there are three main weight losses at 100 °C, 200 °C and 400 °C. The initial loss for the samples at around 100 °C is due to the adsorbed moisture, which was 2.1%. The weight loss (2.9%) until 200 °C is attributed to the removal of residual PEG, which was the structuring agent used to fabricate Cu₂O nanocubes. The weight loss above 200 °C was 4.3%, which accounted for the total loss of C-NWs in the nanocomposite.

Figure 4.6b illustrates the nature of carbon in C-NW/TiO₂ NF/Cu₂O, by using Raman spectroscopy. The Raman spectra shows two peaks of 1370 cm⁻¹ and 1593 cm⁻¹ for the D and G band respectively, which is characteristic for amorphous carbon.

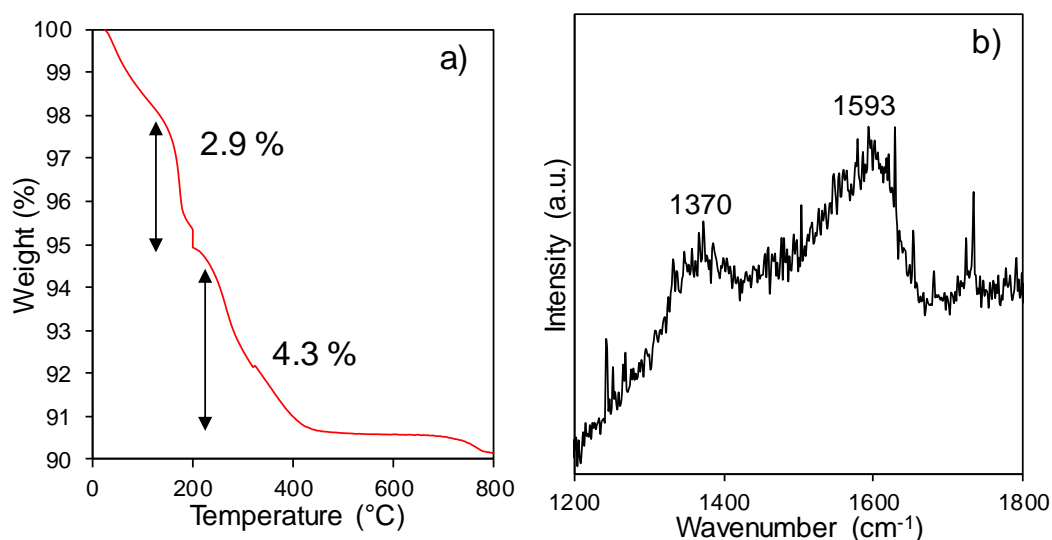


Figure 4.6 a) TGA and b) Raman spectra of C-NW/TiO₂ NF/Cu₂O.

4.4. Photoelectrochemical analysis

The effect of interparticle charge transfer between C-NWs and TiO₂ NF/Cu₂O nanocomposite was investigated using PEC measurements under chopped visible light illumination at 0 V vs. RHE. PEC measurements were studied in a three-electrode system, with Pt wire as counter electrode, Hg/Hg₂SO₄ as reference electrode and photocatalyst was dropcasted onto glassy carbon electrode as the working electrode. The Figure 4.7a shows C-NW/TiO₂ NF/Cu₂O > TiO₂ NF/Cu₂O > Cu₂O > TiO₂ NF in terms of photoresponse. The low photocurrent density of TiO₂ NF is attributed to high recombination, and Cu₂O had photostability issues during charge transfer. The photocurrent density of C-NW/TiO₂ NF/Cu₂O is approximately 6 times higher than TiO₂ NF/Cu₂O and over 8 times higher than both Cu₂O and TiO₂ NF. The nanocomposite produced a higher photocurrent response indicating more efficient charge transfer where C-NWs can act as a carrier mobility layer at the nanocomposite²⁶. The increase in photocurrent of C-NW/TiO₂ NF/Cu₂O compared to TiO₂ NF/Cu₂O suggests the C-NWs have more significant influence on electron transfer than the nanocomposite.

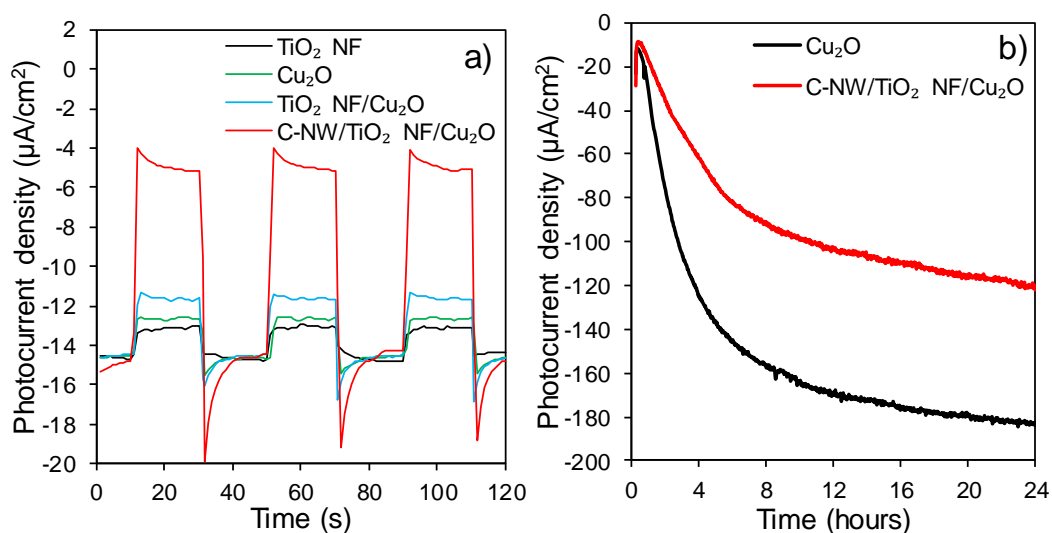


Figure 4.7 a) Transient photocurrent and b) catalyst stability (0 V vs. RHE) of TiO₂ NF, Cu₂O, TiO₂ NF/Cu₂O and C-NW/TiO₂ NF/Cu₂O under visible light irradiation, using 200 W Hg-Xe arc lamp, 0.5 M Na₂SO₄ electrolyte.

Cu₂O is difficult to use in practical applications as it has low photostability, therefore the effect of C-NWs was studied on the catalyst stability (Figure 4.7b). The photocurrent generated by Cu₂O decreased at a faster rate than C-NW/TiO₂/Cu₂O over a period of 24 hours, which suggests the addition of TiO₂ NF and C-NWs increased photostability.

Bare TiO₂ NF showed low photocurrent density vs. voltage curves (Figure 4.8a) but Cu₂O nanocubes exhibited a higher photocurrent density under visible light due to its narrow band gap. With the introduction of the nanocomposite, TiO₂ NF/Cu₂O, the photocurrent density increased slightly to 60.3 μA/cm² at 1.23 V vs. RHE. The integration of C-NWs yielded a significant increase in photocurrent density of 139.8 μA/cm², which is almost 4 times higher than TiO₂ NF. The sharp increase in photocurrent density indicates high charge transfer and separation efficiency with C-NWs in C-NW/TiO₂ NF/Cu₂O¹⁰. The results were similar in the chopped photocurrent density vs. voltage curve, as shown in Figure 4.8b, where C-NW/TiO₂ NF/Cu₂O reached photocurrent densities of 122.4 μA/cm² at -0.3 V vs. RHE, which was 2 times higher than TiO₂ NF/Cu₂O. This shows the large aspect ratio of 1D TiO₂ NF provides efficient charge transport in a vertical path as it has a much smaller

diameter. Therefore, there is a shorter distance for charge transfer which minimises the possibility of recombination²⁷.

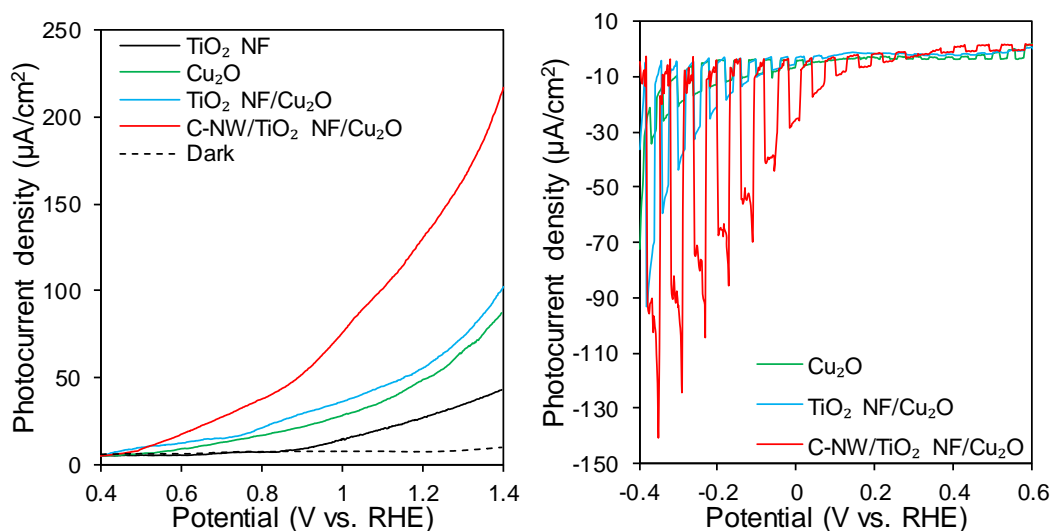


Figure 4.8 a) I-V curve and b) chopped I-V curves of TiO₂ NF, Cu₂O, TiO₂ NF/Cu₂O and C-NW/TiO₂ NF/Cu₂O under visible light irradiation at a scan rate of 10 mV/s, using 200 W Hg-Xe arc lamp, 0.5 M Na₂SO₄ electrolyte.

The interfacial properties of C-NW/TiO₂ NF/Cu₂O were studied by electrochemical impedance spectroscopy (EIS), in the form of a Nyquist plot. A Nyquist plot is used to investigate the characteristics of the charge transfer process, where the semicircle diameter indicates the charge transfer resistance. In Figure 4.9, the semicircle diameter of Cu₂O and TiO₂ NF is slightly larger than TiO₂ NF/Cu₂O, which shows they have similar charge transfer resistance. C-NW/TiO₂ NF/Cu₂O exhibited the lowest charge transfer resistance, which is attributed to the integration of C-NWs. This indicates that C-NWs reduced the resistance to charge carrier transport due to the efficient separation of charge carriers in the nanocomposite¹⁰.

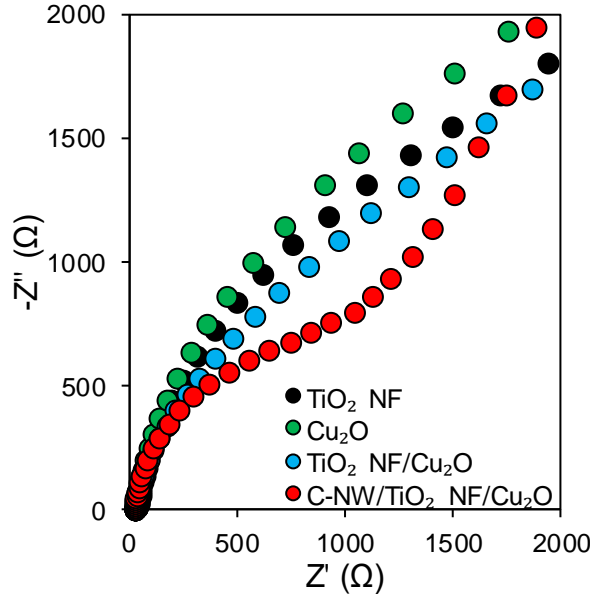


Figure 4.9 EIS (Nyquist plot at 0 V vs. RHE) of TiO₂ NF, Cu₂O, TiO₂ NF/Cu₂O and C-NW/TiO₂ NF/Cu₂O at a scan rate of under visible light irradiation, using 200 W Hg-Xe arc lamp, 0.5 M Na₂SO₄ electrolyte.

Figure 4.10 shows the Mott Schottky plots of Cu₂O, TiO₂ NF, C-NW/TiO₂ NF which is used to calculate the flat-band potential and majority carrier densities of each semiconductor in the nanocomposite. The positive and negative slopes are indicative of n-type and p-type semiconductors, respectively. The flat-band potentials are shown by the x-intercept of the linear section, which are 0.54 V, -0.76 V and -0.72 V vs. RHE for Cu₂O, TiO₂ NF and C-NW/TiO₂ NF respectively. The anodic shift of 40 mV between TiO₂ NF and C-NW/TiO₂ NF is in agreement with previous reports²⁷.

The gradient of the linear portion of the plot is used to calculate the majority carrier density (N_A), using Equation 2.10.

$$\frac{1}{c^2} = \frac{2}{\epsilon\epsilon_0 e N_A} \left(V - E_{fb} - \frac{k_B T}{e} \right) \quad (2.10)$$

Where c is the capacitance, ϵ is the dielectric constant of TiO₂ and Cu₂O is 170²⁸ and 7.60²⁹ respectively, ϵ_0 is permittivity of free space, V is the applied potential, E_{fb} is the flat-band

potential, e is the electron charge, k_B is the Boltzmann's constant and T is the temperature. The N_A values Cu_2O , TiO_2 NF and TiO_2 NF/C-NWs are $5.36 \times 10^{18} \text{ cm}^{-3}$, $1.06 \times 10^{19} \text{ cm}^{-3}$ and $1.30 \times 10^{19} \text{ cm}^{-3}$ respectively. This showed that 1D TiO_2 NF had more charge carrier activity, but more studies are needed to gain conclusive results.

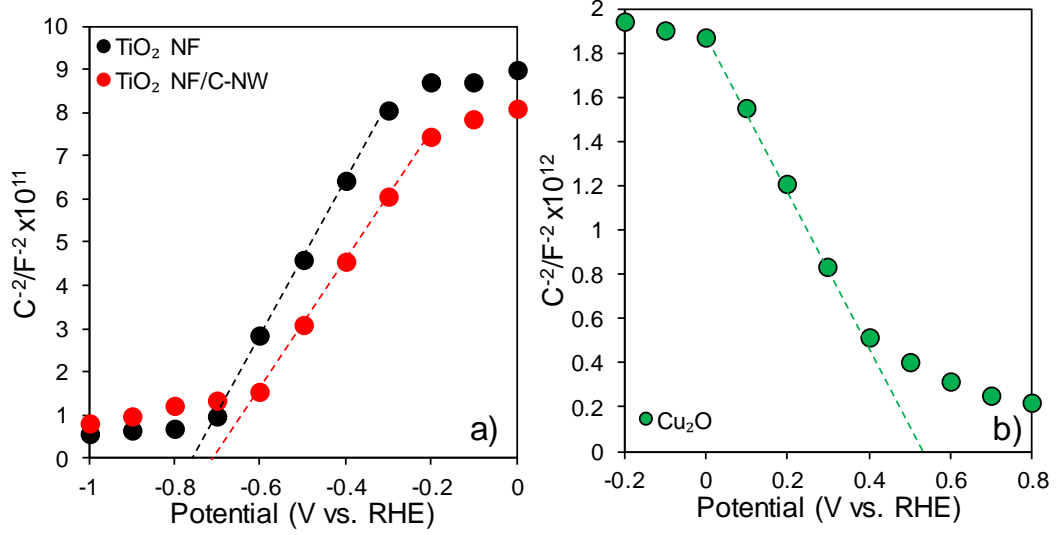


Figure 4.10 a) Mott Schottky plot of TiO_2 NF and Cu_2O (b) using 200 W Hg-Xe arc lamp, 0.5 M Na_2SO_4 electrolyte.

The valence band edge of Cu_2O , E_V , is calculated by Equation 2.11.

$$E_V = E_{fb} - k_B T \ln \frac{N_V}{N} \quad (2.11)$$

Where E_{fb} is the flat-band potential, k_B is the Boltzmann's constant, T is the temperature and N is Avogadro's constant.

Where the effective density of states, N_V , is calculated using Equation 2.12.

$$N_V = 2 \left(\frac{2\pi m_h k_B T}{h^2} \right)^{\frac{3}{2}} \quad (2.12)$$

The effective hole mass is denoted as $m_h = 0.58m_e$ for Cu_2O ³⁰, where m_e is the mass of a free electron. N_V for Cu_2O was $1.10 \times 10^{19} \text{ cm}^{-3}$. The valence band edge (E_V) was 0.56 V for Cu_2O , thus as Cu_2O has a band gap of 2.36 eV, the valence and conduction band positions are at 0.56 V and -1.80 V vs. RHE respectively. Assuming the distance between the flat-band potential of TiO_2 NF and the lowest potential of the CB is negligible³⁰, the CB of TiO_2 NF is -0.76 V vs. RHE. Thus, the band gap of TiO_2 NF is 3.28, so the valence band and conduction band are positioned at 2.52 V and -0.76 V vs. RHE respectively.

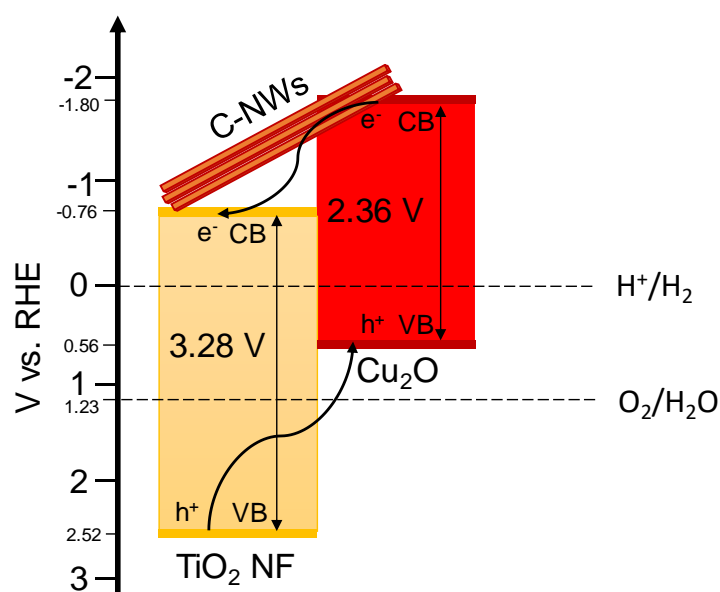


Figure 4.11 Schematic for the energy band structure of C-NWs/ TiO_2 NF/ Cu_2O nanocomposite.

A schematic of the energy band structure is proposed in Figure 4.11. The enhanced photocatalytic activity of C-NW/ TiO_2 NF/ Cu_2O nanocomposite was attributed to a few reasons. Electrons from Cu_2O travel to TiO_2 NF and holes from TiO_2 NF migrate to the surface of Cu_2O ³¹, which is supported by the band positions of Cu_2O and TiO_2 NF. The addition of C-NWs to TiO_2 NF greatly broadens the solar absorption to the visible light region as shown in Figure 4.5a. Also, the impedance spectra show the C-NW/ TiO_2 NF/ Cu_2O nanocomposite has improved charge carrier density and least charge transfer

resistance compared to bare TiO₂ NF and Cu₂O. This suggests that the efficient charge transfer is related to high surface area to volume ratio³² of 1D TiO₂ NF and increased conductivity with C-NWs. The addition of C-NWs improved the charge carrier density, so it is proposed that the C-NWs promotes electron transfer between CB of Cu₂O toward CB of TiO₂, enhancing separation of photogenerated electron-hole pairs. Overall, the introduction of C-NWs in the nanocomposite of C-NWs/ TiO₂/Cu₂O enhance the PEC performance and the 1D structure of TiO₂ NF increase charge transport, and the nanocomposite increases photostability and extends light absorption region.

4.5. Conclusions

In summary, C-NW/TiO₂ NF/Cu₂O nanocomposite was fabricated via hydrothermal treatment and subsequent solution phase chemistry, which provided intimate contact between 1D TiO₂ NF and Cu₂O nanocubes surrounded by C-NWs. The carbon content in the photocatalyst was confirmed by both TGA and Raman spectroscopy, and DRUVS indicated that C-NWs has strong absorption properties as there is superior absorption at higher wavelengths.

C-NW/TiO₂ NF/Cu₂O recorded enhanced PEC activity with higher photocurrent density and impedance spectra illustrated less charge transfer resistance than bare TiO₂ NF and Cu₂O. After calculating the charge carrier densities of TiO₂ NF and C-NW/TiO₂ NF, it was shown that the addition of C-NWs improved the charge carrier density by promoting electron transfer. Therefore, C-NW/TiO₂ NF/Cu₂O provided superior light absorption properties, efficient charge transfer, separation of electron-hole pairs and the integration of C-NWs, which promote further electron transport within the nanocomposite. All these properties contribute towards fabricating a photocatalyst with superior PEC activity. This design and preparation of novel photocatalysts is an example of fabricating effective nanocomposite materials for solar water splitting.

4.6. References

1. Linsebigler, A.L.; Lu, G.; Yates, J.T. *Chem. Rev.* **1995**, *95*.
2. Özgür, Ü.; Alivov, Y.I.; Liu, C.; Alivov, Y.I.; Teke, a.; Reshchikov, M.A.; Doğanc, S.; Avrutin, V.; Cho, S.J.; Morkoç, H. *J. App. Phys.* **2005**, *98*.
3. Sivula, K.; Formal, F.L.; Graetzel, M. *Chem. Sus. Chem.* **2011**, *4*.
4. Kudo, A.; Omori, K.; Kato, H. *J. Am. Chem. Soc.* **1999**, *121*.
5. Ni, M.; Leung, M.K.H.; Leung, D.Y.C.; Sumathy, K. *Renew. Sus. Ener. Rev.* **2007**, *11*.
6. Abe, R.; *J. Photochem. & Photobio. C: Photochem. Rev.* **2010**, *11*.
7. Hara, M.; Kondo, T.; Komoda, M.; Ikeda, S.; Kondo, J.N.; Domen, K.; Hara, M.; Shinohara, K.; Tanaka, A. *Chem. Commun.* **1998**, *357*.
8. Moniz, S.J.A.; Shevlin, S.A.; Martin, D.J.; Guo, Z-X.; Tang, J.; *En. & Env. Sci.* **2015**, *3*.
9. Woan, K.; Pyrgiotakis, G.; Sigmund, W. *Adv. Mater.* **2009**, *21*.
10. Hou, J.; Yang, C.; Cheng, H.; Jiao, S.; Takeda, O.; Zhu, H. *Energy Environ. Sci.*, **2014**, *7*.
11. Li, W.; Bai, Y.; Liu, W.; Liu, C.; Yang, Z.; Feng, X.; Lu, X.; Chan, K-Y. H. *J. Mat. Chem.* **2011**, *18*.
12. Amjad, M.; Iqbal, M.; Faisal, A.; Junjua, A.M.; Hussain, I.; Hussain, S.Z.; Ghramh, H.A.; Khan, K.A.; Janjua, H.A. *Nanoscale Adv.* **2019**, *1*.
13. Cui, Q.; He, F.; Wang, X.; Xia, B.; Li, L. *ACS Appl. Mater. Interfaces.* **2013**, *5*.
14. Liang, Q.; Ma, W.; Shi, Y.; Li, Z.; Yang, X. *Carbon.* **2013**, *60*.
15. Liu, G.; Qiao, S.Z.; Sun, C.H.; Jin, Y.G.; Smith, S.C.; Zou, J.; Cheng, H.M.; Lu, G.Q. *J. Am. Chem. Soc.* **2009**, *13*, *11*.
16. Sun, S.; Zhang, X.; Song, X.; Liang, S.; Wang, L.; Yang, Z. *Cryst. Eng. Comm.* **2012**, *14*.
17. Zhang, S.; Liu, H.; Sun, C.; Liu, P.; Li, L.; Yang, Z.; Feng, X.; Huo, F.; Lu, X. *J. Mater. Chem. A.* **2015**, *10*.
18. Kumar, S.; Parlett, C.M.A.; Isaacs, M.A.; Jowett, D.V.; Douthwaite, R.E.; Cockett, M.C.R.; Lee, A.F. *Appl. Catal. B-Environ.* **2016**, *189*.
19. Huang, L.; Peng, F.; Yu, H.; Wang, H. *Mater. Res. Bull.* **2008**, *43*.
20. Aghasiloo, Y.; Latifi, M.; Jose, R. *J. Allo. & Comp.* **2019**, *790*.
21. Zhang, W.; Zhu, R.; Ke, L.; Liu, X.; Liu, B. *Small.* **2010**, *6*.
22. Hiramatsu, M.; Hori, M. *Carbon Nanowalls: Synthesis and Emerging Applications.* Springer. **2010**.
23. Meng, F.; Li, J.; Cushing, S.K.; Bright, J.; Zhi, M.; Rowley, J.D.; Hong, Z.; Manivannan, A.; Bristow, A.D.; Wu, N. *ACS Catal.* **2013**, *3*.
24. Zhang, J.; Liu, W.; Wang, X.; Wang, X.; Hu, B.; Liu, H. *App. Sur. Sci.* **2013**, *282*, *1*.
25. Bessekhoad, Y.; Robert, D.; Weber, J.V.; *Catalysis Today.* **2005**, *101*.
26. Babu, S.G.; Vinoth, R.; Kumar, D.P.; Shankar, M.V.; Chou, H.L.; Vinodgopal, K.; Neppolian, B. *Nanoscale.* **2015**, *7*.
27. Sakthivel, S.; Kisch, H.; *Angew. Chem. Int. Ed.* **2003**, *42*.
28. Parker, R. A. *Phys. Rev.* **1961**, *124*.
29. Zhang, Z.; Wang, P. *J. Mat. Chem.* **2012**, *22*.
30. Paracchino, A.; Brauer, J.C.; Moser, J-E.; Thimsen, E.; Graetzel, M. *J. Phys. Chem. C.* **2012**, *116*.

31. Hitoki, G.; Takata, T.; Kondo, J.N.; Hara, M.; Kobayashi, H.; Domen, K. *Chem. Commun.* **2002**, 1698.
32. Luo, J.; Steier, L.; Son, M.K.; Schreier, M.; Mayer, M.; Gratzel, M. *Nano Lett.* **2016**, 16.

Chapter 5

Two-dimensional carbon enhanced chemical stability of Cu₂O

Chapter 5 describes the facile one-pot synthesis of hierarchical Cu₂O nanospheres and the fabrication of Cu₂O/rGO. The photocatalyst was characterised and photocatalytic activity was tested by hydrogen evolution in visible light, photodecomposition of 4-chlorophenol (4-CP) and photoelectrochemical analysis.

5.1. Introduction

Copper (I) oxide (Cu₂O) is a well-documented p-type semiconductor with a band gap of 2.17 eV, which is favourable for visible light hydrogen evolution and photocatalytic water splitting¹. Cu₂O has a high optical absorption coefficient with a theoretical H₂ conversion efficiency of 18%². Thus, Cu₂O is widely used in photodecomposition of pollutants for water purification processes³⁻⁵. However, the two major issues with Cu₂O is the reduction and oxidation potential lie within the bandgap which results in poor photostability² and the rapid recombination of photogenerated electrons and holes hinder activity⁶.

Over the last decade, research in structurally modifying Cu₂O have been carried out to combat the above issues in photocatalysis⁷⁻¹⁰. For example, there have been many reports on tuning photophysical properties of Cu₂O by forming phase junctions, heterojunctions or using cocatalysts for efficient solar harvesting, improved charge carrier separation and transport¹¹. Moreover, hierarchical semiconductors have shown to increase electronic and optical properties further¹².

Graphene is a 2-dimensional monolayer that has attracted attention since it has unique physical and electronic properties¹³. Reduced graphene oxide (rGO) has caused extreme interest over the last few years as they have favourable properties, such as high surface area, tuneable band gap and strong electron mobility¹⁴. rGO possesses chemically reactive oxygen functionalities on the surface, which means it is a versatile catalyst support that can

be hybridised with other semiconductors with superior photocatalytic properties^{15, 16}. For example, rGO was studied as a support for both p-type Cu₂O and n-type TiO₂ and were reported to enhance charge separation and improve photostability of Cu₂O in particular³. They learned that it was because of three important functions of graphene, which are trapping and shuttling photogenerated electrons as well as increasing light absorption¹⁷. Furthermore, Zhang et al.¹⁸ studied thin protective carbon layers formed by glucose carbonisation and found it increased photostability of Cu₂O greatly. They learned that an optimal carbon thickness of 20 nm gave the highest photocurrent density.

Therefore, in this chapter, Cu₂O nanospheres were fabricated which consist of large aggregates and small particles of Cu₂O, hence using the term 'hierarchical'. Subsequent Cu₂O/rGO nanocomposite was designed by one-pot hydrothermal synthesis. Cu₂O/rGO was used to decompose 4-chlorophenol as a model pollutant. Hydrogen evolution and photoelectrochemical (PEC) measurements were recorded, where Cu₂O/rGO showed enhanced PEC activity, photostability and improved charge transport properties than bare Cu₂O.

5.2. Catalyst synthesis

Cu₂O/rGO was synthesised by a wet chemical method under ambient conditions and had the appearance of Pompom Dahlia flowers, as shown in Figure 5.1. Graphene oxide (GO) was prepared by a modified Hummer's method¹⁹ and ultrasonicated in 10 ml water for 30 minutes. A mixture of 50 ml (0.2 M) CuCl₂ and 5 ml (0.06 M) PEG-600 was added and ultrasonicated for 10 minutes. The suspension was heated to 60°C and stirred for 30 minutes, observing a blue solution.

8 ml (2 M) NaOH was added into the blue solution and 1 M aqueous hydrazine monohydrate (H₄N₂.H₂O) (1:5 v/v water) and stirred for 5 minutes. The mixture was poured into a round bottom flask and purged under N₂ for 30 minutes to form Cu₂O, where the solution changed colour to brown. The residual solid was removed by centrifugation at 6,000 RPM for 10min with several water washes and ethanol washes to remove remaining PEG.

The synthesis procedure of Cu_2O is demonstrated in Figure 5.1. The Cu (II)-PEG complex was added to GO, and this mixture was precipitated by NaOH and then reduced to Cu_2O by hydrazine, as well as reduction of the graphene framework to form hierarchical $\text{Cu}_2\text{O}/\text{rGO}$ ²⁰. The hydroxyl groups in PEG and rGO control Cu (II) density and directly affect formation of hierarchical Cu_2O , as PEG acts as a structure-directing agent promoting formation of Cu_2O which combines around rGO.

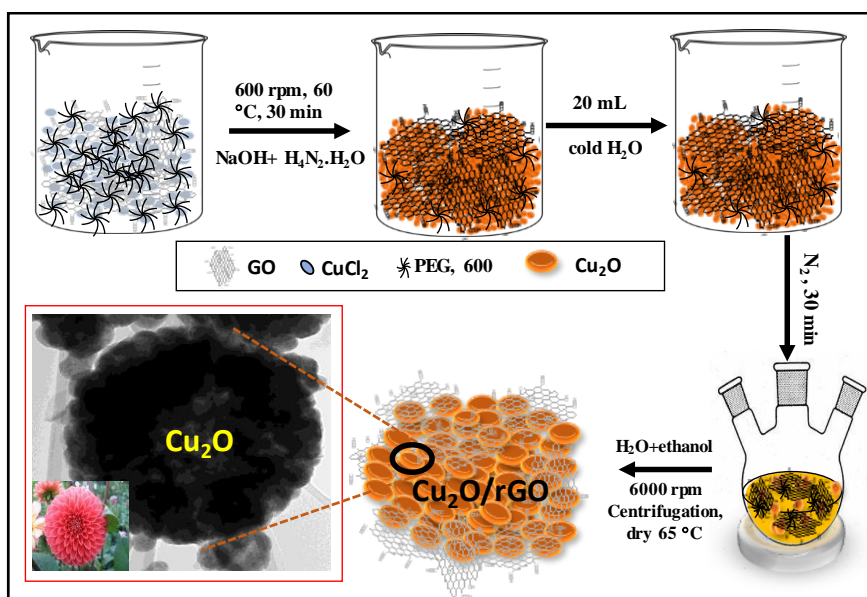


Figure 5.1 Schematic of the synthesis procedure of Pom-pom Dahlia $\text{Cu}_2\text{O}/\text{rGO}$.

5.3. Characterisation

5.3.1. Microscopy studies

TEM images were used to observe the morphology of Cu_2O and $\text{Cu}_2\text{O}/\text{rGO}$. Cu_2O nanoparticles were successfully synthesised as spherical aggregates approximately 400-500 nm in diameter (5.2a) and smaller individual particles are identified with sizes between 40-60 nm (5.2b). The shapes of the aggregates were that of a Pom-pom Dahlia-like morphology (Figure 5.2d). The TEM images presented in Figure 5.3 introduce rGO into

the nanocomposite, as shown by the transparent graphene oxide sheets that are folded and wrinkled. Both Cu_2O aggregates and individual particles in the nanocomposite were smaller than pure hierarchical Cu_2O , ranging from 250-400 nm (Figure 5.3a inset) and 15-20 nm (Figure 5.3c inset).

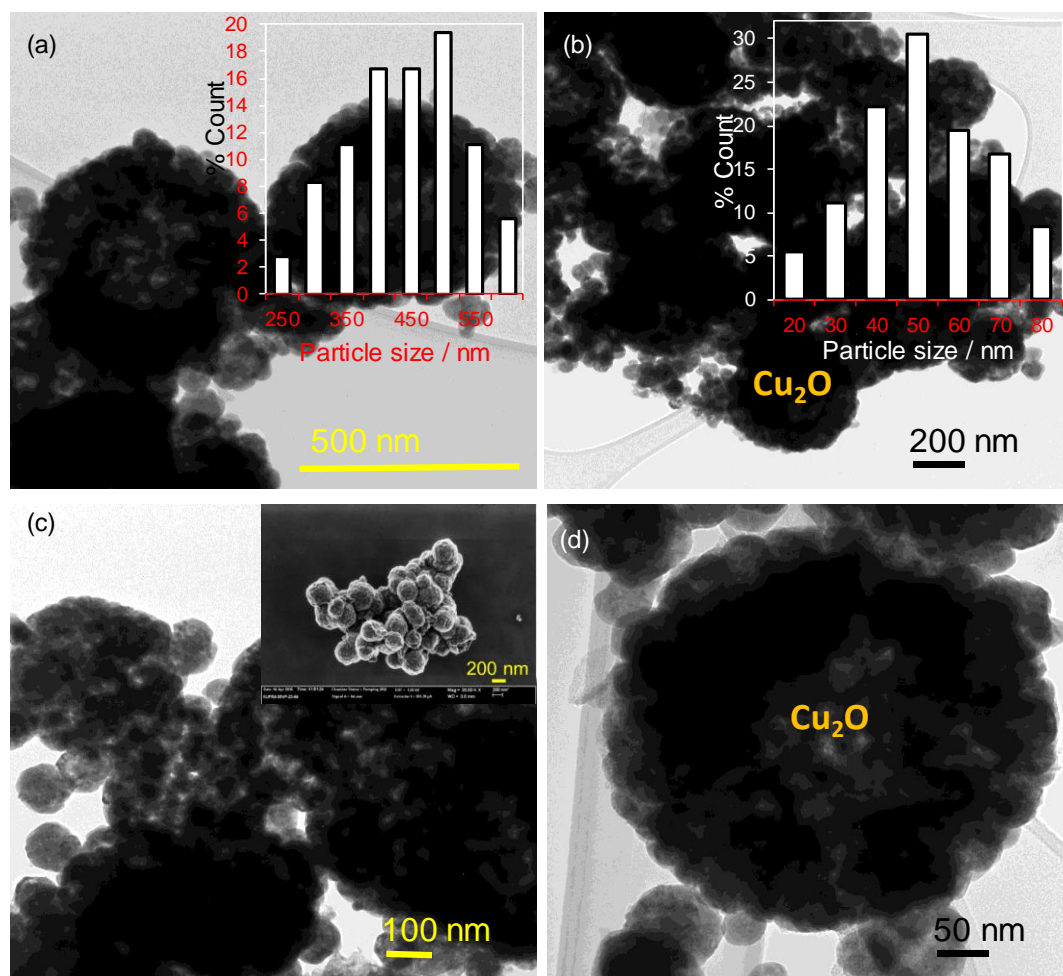


Figure 5.2 (a-d) TEM images of Pompon Dahlia hierarchical Cu_2O . Insets of (a) and (b) show particle size distribution of aggregated Cu_2O and individual Cu_2O nanospheres. Insets of (c) show the SEM image of aggregates.

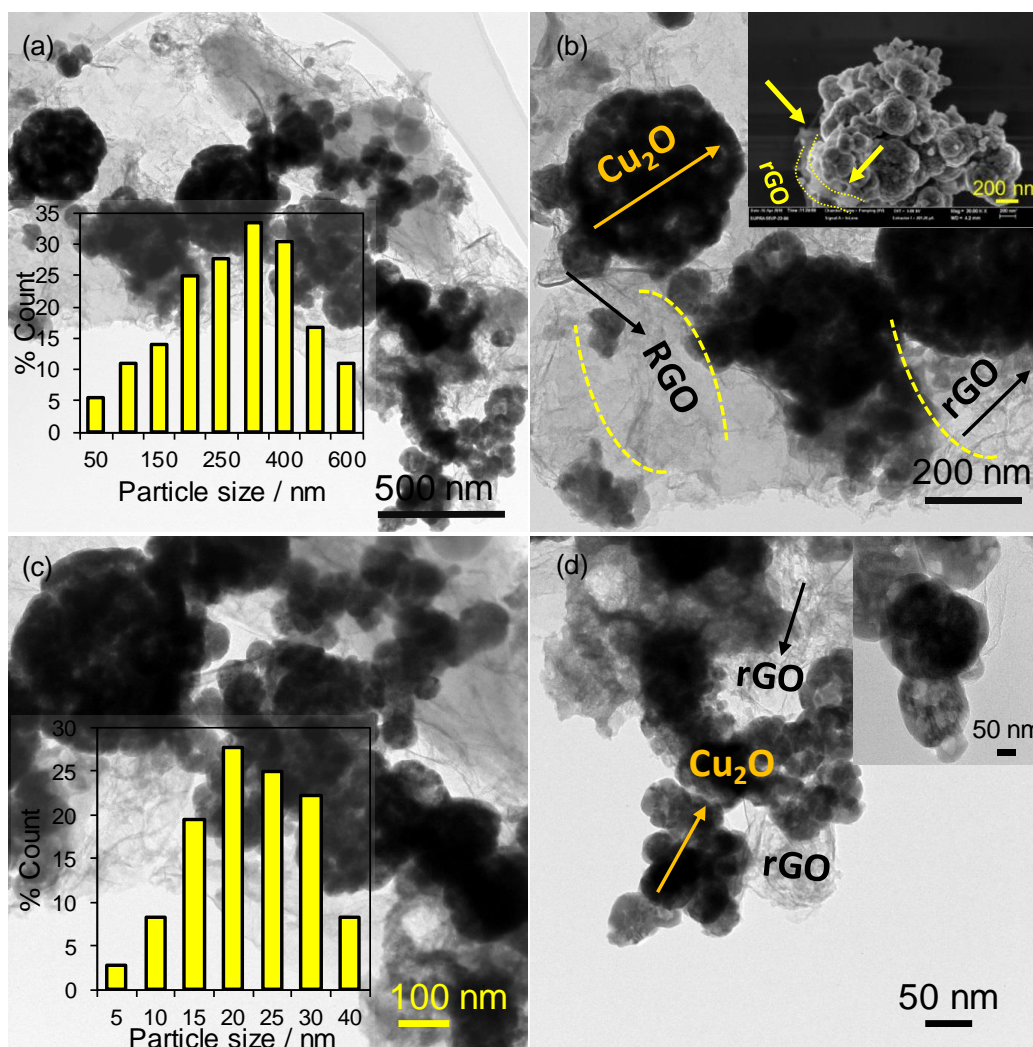


Figure 5.3 TEM images of Cu₂O/rGO. Insets of (a) and (c) show particle size distribution of aggregates and individual Cu₂O particles respectively, (b) SEM image and (d) HRTEM image of aggregates.

5.3.2. Photophysical properties

The XRD patterns indicated the formation of crystalline Cu₂O (Figure 5.4a) in both hierarchical Cu₂O and Cu₂O/rGO nanocomposite, indicated by peaks at 29.56°, 36.41°,

42.31°, 61.36°, and 73.50° associated with characteristic (110), (111), (200), (220), (311), and (222) peaks of pure Cu₂O (JCPDS 03-0898)²¹.

The absence of reduced graphene oxide reflections at 25° is attributed to a very low concentration (<0.5 wt.%) in Cu₂O/rGO^{22, 23}. The average crystallite size calculated from the Scherrer equation (Equation 2.2) shows a similar size for both Cu₂O and Cu₂O/rGO (at 15 nm), which suggests rGO matrix has little impact on the precipitation and reduction of the copper precursor. The optical properties of the two catalysts were investigated by DRUVS (Figure 5.4b); where the absorbance spectra ranged from 200-600 nm, which is consistent with literature^{24, 25}.

The optical band gaps E_{BG} were calculated from the Tauc plots (Figure 5.4c):

$$\alpha h\nu = C(h\nu - E_{BG})^n \quad (2.6)$$

Where C is the proportionality constant and α is the absorption coefficient determined from the Kubelka-Munk formula.

$$\alpha = \frac{(1-R)^2}{2R} \quad (2.7)$$

The direct band gaps for Cu₂O and Cu₂O/rGO were calculated as 2.42 eV and 2.13 eV respectively. From Figure 5.4b, there was a higher absorbance of Cu₂O than Cu₂O/rGO, but the red shift in Cu₂O/rGO may arise from interfacial contact between rGO sheets and Cu₂O or from changes in valence band (VB) or conduction band (CB) energies²⁶.

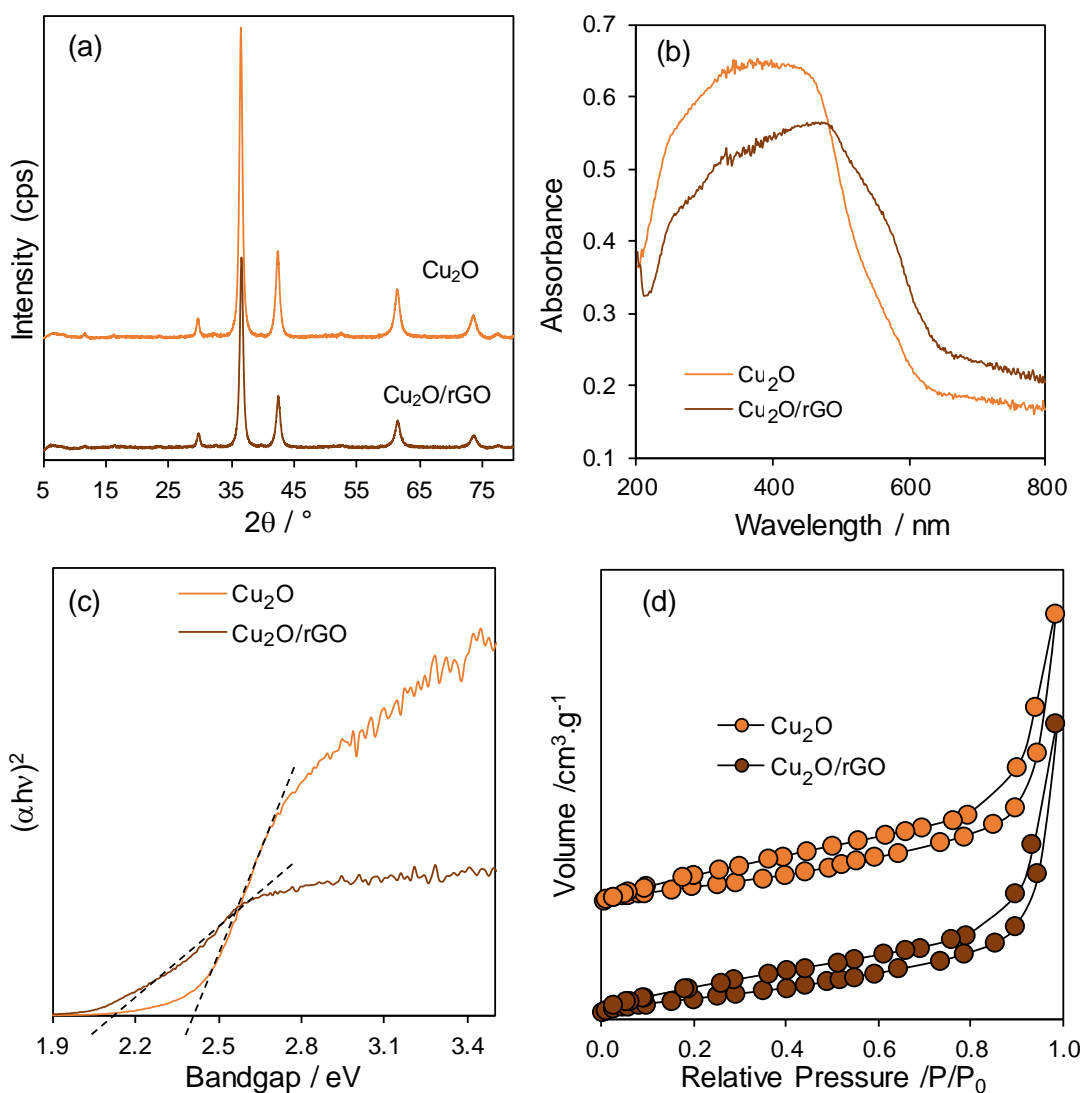


Figure 5.4 (a) XRD patterns, (b) DRUV spectra and (c) Tauc plots, and (d) N_2 adsorption-desorption isotherms of Pom-pom Dahlia-like hierarchical Cu_2O and $\text{Cu}_2\text{O}/\text{rGO}$ nanocomposite.

5.3.3. XPS analysis

The surface copper oxidation state was quantified from Cu 2p XP Spectra (Figure 5.5a). Cu_2O and $\text{Cu}_2\text{O}/\text{rGO}$ had many spin-orbits split doublets with $2p_{3/2}$ binding energies of 932.2 eV and 934.4 eV (Cu_2O and Cu (II) carbonate dihydroxide respectively). The peak at 943.4 eV is associated with Cu (II) species. The lack of Cu (II) XRD features proposes

that $\text{Cu}_2(\text{OH})_2\text{CO}_3$ is formed from a post-synthesis side reaction of Cu_2O nanoparticle surfaces with the atmosphere²⁷.

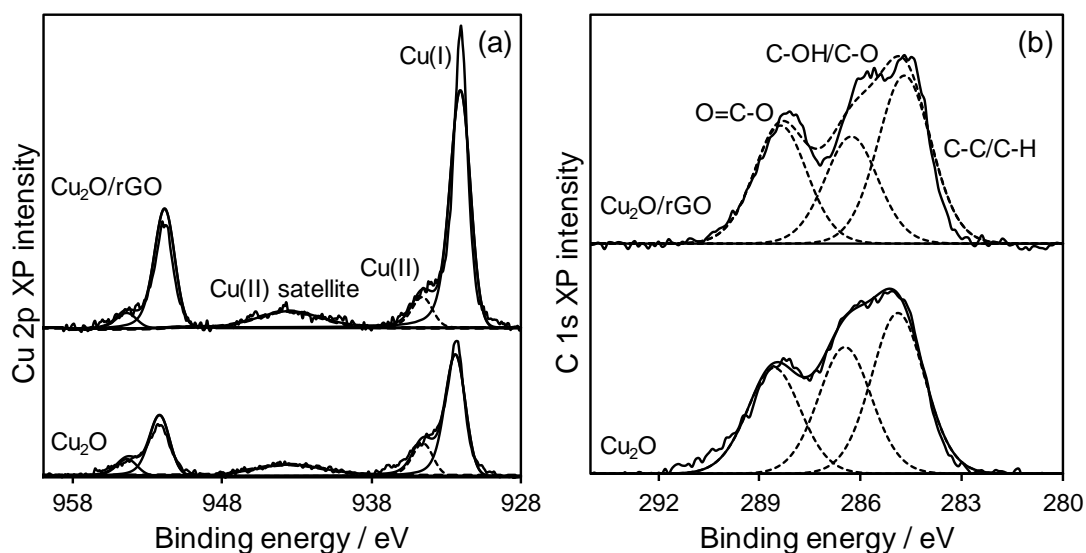


Figure 5.5 (a) Cu 2p and (b) corresponding C 1s XP spectra of Pompom Dahlia-like hierarchical Cu_2O and $\text{Cu}_2\text{O}/\text{rGO}$ nanocomposite.

The C 1s XP spectra (Figure 5.5b) illustrated identical distributions of three distinct chemical environments for both catalysts at 284.6, 286.2, and 288.3 eV, assigned to the alcohol and ether functions of PEG and surface carbonate respectively^{3, 28}. The spectral fittings were shown in Table 5.1, showing the photocatalysts consist of mainly Cu_2O (78.8% and 88.5%).

Table 5.1 Fitted C 2p XP spectra of Pompom Dahlia-like hierarchical Cu_2O and $\text{Cu}_2\text{O}/\text{rGO}$ nanocomposite.

Catalyst	Cu (I) atom %	Cu (II) atom %	Cu (I)/ Cu (II)
Hierarchical Cu_2O	78.8	21.2	3.72
Hierarchical $\text{Cu}_2\text{O}/\text{rGO}$	88.5	11.5	7.70

There was a slight increase in sp^2 carbon for Cu_2O/rGO as shown in Table 5.2, which is expected with the addition of graphene²⁸. The O 1s spectra (Figure 5.6) were consistent with these assignments, exhibiting three distinct chemical environments at 531.4, 533.4, and 535.8 eV from Cu_2O , carbonate, and PEG ether species respectively. The band gap energies were examined using valence band (VB) XPS, as shown in Figure 5.7. The VB edge potential of hierarchical Cu_2O and Cu_2O/rGO were +1.30 and +1.10 eV relative to the Fermi level. The conduction band (CB) edge was calculated from the band gap and VB XPS, to give a value of -1.12 eV and 1.03 eV for hierarchical Cu_2O and Cu_2O/rGO respectively.

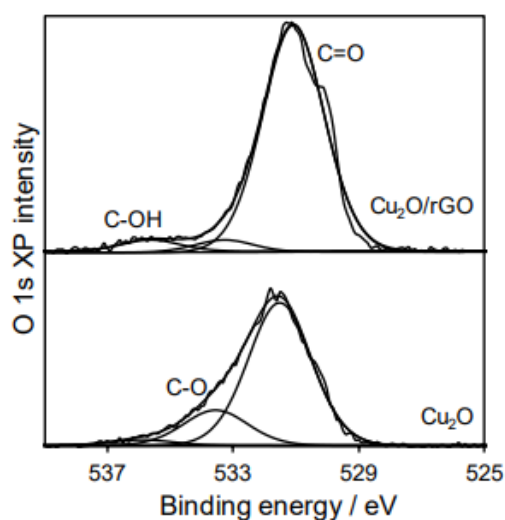


Figure 5.6 O 1s XP spectra of Pompon Dahlia-like hierarchical Cu_2O and Cu_2O/rGO nanocomposite.

Table 5.2 Fitted C 1s XP spectra of Pompon Dahlia-like hierarchical Cu_2O and Cu_2O/rGO nanocomposite.

Catalyst	(C-C) (%)	(C=O) (%)	(-O-C=O) (%)
Hierarchical Cu_2O	40.8	32.3	26.9
Hierarchical Cu_2O/rGO	42.7	27.3	30.0

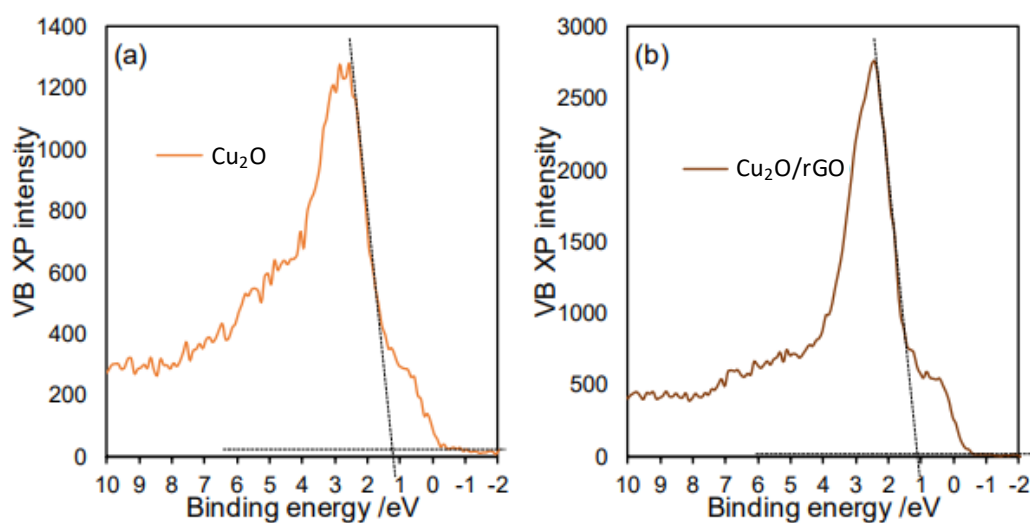


Figure 5.7 Valence band XPS of Pompom Dahlia-like hierarchical Cu₂O and Cu₂O/rGO nanocomposite.

The photophysical properties of Pompom Dahlia-like hierarchical Cu₂O and Cu₂O/rGO nanocomposite were summarised in Table 5.3.

Table 5.3 Photophysical properties of Pompom Dahlia-like hierarchical Cu₂O and Cu₂O/rGO nanocomposite.

Sample	Crystallite size ^a (nm)	Particle size ^b (nm)	Band gap ^d (eV)	CB edge potential ^e (eV)	VB edge potential ^e (eV)
Hierarchical Cu ₂ O	15.3	400-500	2.42	-1.12	1.3
Hierarchical Cu ₂ O/rGO	14.7	250-400	2.13	-1.03	1.1

^aXRD, ^bTEM. ^cN₂ porosimetry. ^dDRUVS. ^eCalculated from valence band XPS and DRUVS.

5.4. Hydrogen evolution

The photocatalytic activity of Cu₂O and Cu₂O/rGO for H₂ evolution was investigated under visible light irradiation in the presence of methanol as a sacrificial hole scavenger (Figure 5.8). There was no oxygen evolution for either catalyst, but 18 μmol. g⁻¹.h⁻¹ and 31 μmol. g⁻¹.h⁻¹ of hydrogen was evolved for Cu₂O and Cu₂O/rGO respectively, with negligible deactivation during a 14-hour operation for each catalyst.

The increase in methanol concentration from 1% to 10% increased H₂ evolution greatly, which reached 234 μmol.g⁻¹.h⁻¹ for the hierarchical Cu₂O and 352 μmol.g⁻¹.h⁻¹ for the hierarchical Cu₂O/rGO nanocomposite. This suggests that electron-hole recombination is rate-determining for hydrogen evolution over both catalysts. In Figure 5.8, Cu₂O/rGO exhibited greater photocatalytic activity than Cu₂O, which is confirmed by a higher apparent quantum efficiency (AQE) of 3.35% using Equation 2.14, compared to 2.23% for hierarchical Cu₂O. The hybridisation of Cu₂O with rGO nanosheets almost doubles the specific activity, consistent with greater visible light absorption²⁹.

$$\text{AQE (\%)} = \frac{\text{Mol. reacted electrons per unit time}}{9.94 \times 10^{-8}} \times 100 \quad (2.14)$$

The hydrogen evolution of hierarchical Cu₂O was superior to non-porous Cu₂O (13 μmol. g⁻¹.h⁻¹)³⁰ and Cu₂O nanoparticles (10 μmol. g⁻¹.h⁻¹) of comparable size³¹. The AQE. is higher than reported for Pt-decorated 500 nm Cu₂O nanocubes (AQE = 1.2%)³², 375 nm hierarchical Cu₂O nanocubes (AQE = 1.2%)³³, and 150 nm Cu₂O nanostructures on a silicon wafer (AQE = 0.3%)³⁴ under visible light. This demonstrates the superior photophysical properties of the Pom-pom-like aggregates. Table 5.4 illustrates the visible light hydrogen evolution of Cu₂O photocatalysts.

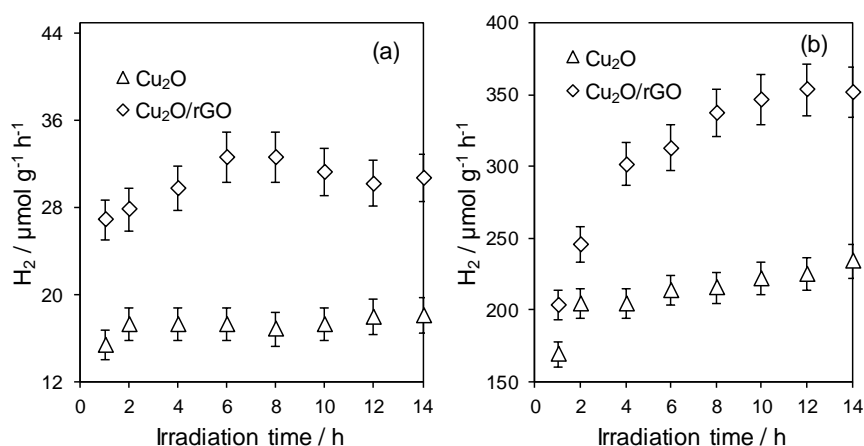


Figure 5.8 Visible light photocatalytic H₂ production over Pompom Dahlia-like hierarchical Cu₂O and Cu₂O/rGO nanocomposite with (a) 1 vol.% and (b) 10 vol.% methanol (in water) as a sacrificial hole scavenger. Reaction conditions: 0.02 g catalyst, 200 W Hg-Xe ($\lambda > 420$ nm).

Table 5.4 Visible light photocatalytic hydrogen evolution of Cu₂O photocatalysts.

Photocatalyst (~300 nm particle size)	Apparent quantum efficiency (%)	H ₂ evolution (μmol. g ⁻¹ .h ⁻¹)	Experimental details	Reference
Cu ₂ O	0.3	10	<ul style="list-style-type: none"> • 0.5 g catalyst • 300 W Xe lamp 	31
Cu ₂ O	N/A	13	<ul style="list-style-type: none"> • 20 mg catalyst • 150 W halogen lamp 	30
Hierarchical Pt/Cu ₂ O	1.2	15	<ul style="list-style-type: none"> • 25 mg catalyst • 50 ml, 0.5 M Na₂SO₃ • 200 W Hg-Xe arc lamp 	33
Hierarchical Cu ₂ O/rGO	2.29	30.72	<ul style="list-style-type: none"> • 50 mg catalyst • 50 ml, 1 vol.% methanol • 200 W Hg-Xe arc lamp 	This work

5.5. Photodecomposition of 4-chlorophenol

The visible light photocatalytic decomposition of 4-chlorophenol (CP) was studied over hierarchical Cu_2O and $\text{Cu}_2\text{O}/\text{rGO}$. 4-CP was selected as a model recalcitrant organic compound as it does not exhibit visible light absorption, thus cannot act as a photosensitiser which is problematic in mechanistic investigations of photocatalytic dye degradation³⁵.

The initial rates and AQE. for 4-CP removal (Figure 5.9a and b) by $\text{Cu}_2\text{O}/\text{rGO}$ were slightly higher than hierarchical Cu_2O aggregates (0.18 vs. 0.16 $\text{mmol.g}^{-1}.\text{min}^{-1}$, and 59 vs. 52% respectively). The conversion of 4-CP reached 95% for hierarchical $\text{Cu}_2\text{O}/\text{rGO}$, compared with 73% for the Cu_2O aggregates after a one-hour reaction.

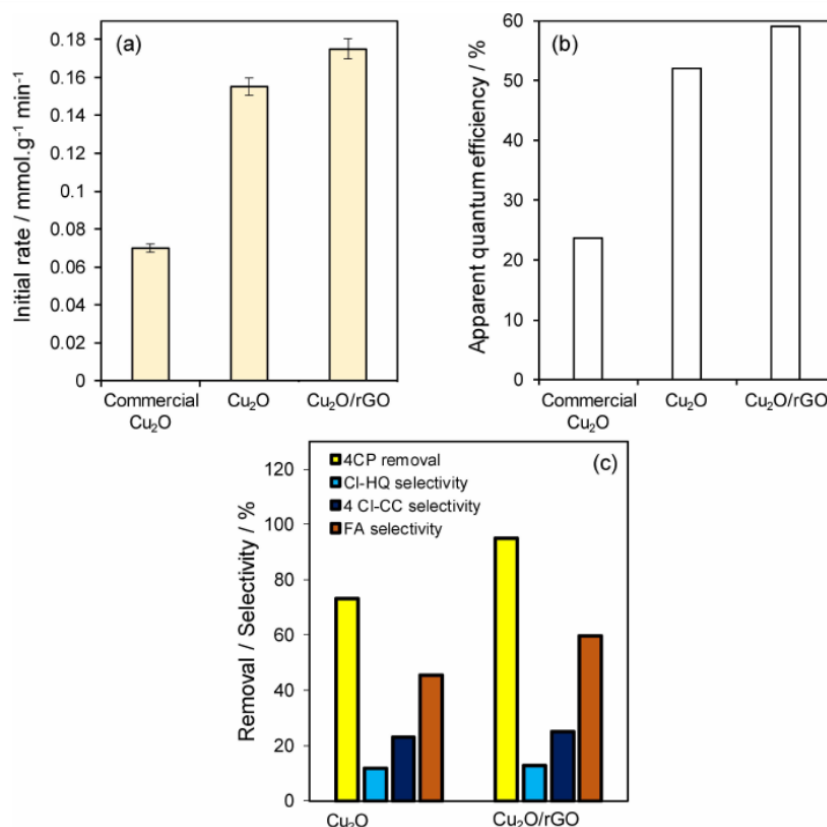


Figure 5.9 Visible light photocatalytic 4-CP degradation over Pompon Dahlia-like hierarchical Cu_2O and $\text{Cu}_2\text{O}/\text{rGO}$ nanocomposite. (a) initial rates of 4-CP removal and (b) corresponding apparent quantum efficiencies after 15 minutes reaction; and (c) 4-CP removal efficiency.

The major products of 4-CP decomposition were identified using HPLC, where chlorohydroquinone (CL-HQ), 4-chlorocatechol (4Cl-CC), and fumaric acid (FA) were formed (Figure 5.9c). The formation of polyoxygenated intermediates is consistent with a radical mechanism involving photogenerated holes transferred to adsorbed water or surface hydroxyls to form hydroxyl radicals ($\cdot\text{OH}$). The reaction of photoexcited electrons with oxygen may produce $\cdot\text{OH}$ via H_2O_2 . The hierarchical $\text{Cu}_2\text{O}/\text{rGO}$ favours more oxidising equivalents potentially resulting from longer charge carrier lifetimes, and faster charge transfer kinetics³⁶.

5.5.1. Photocatalytic stability

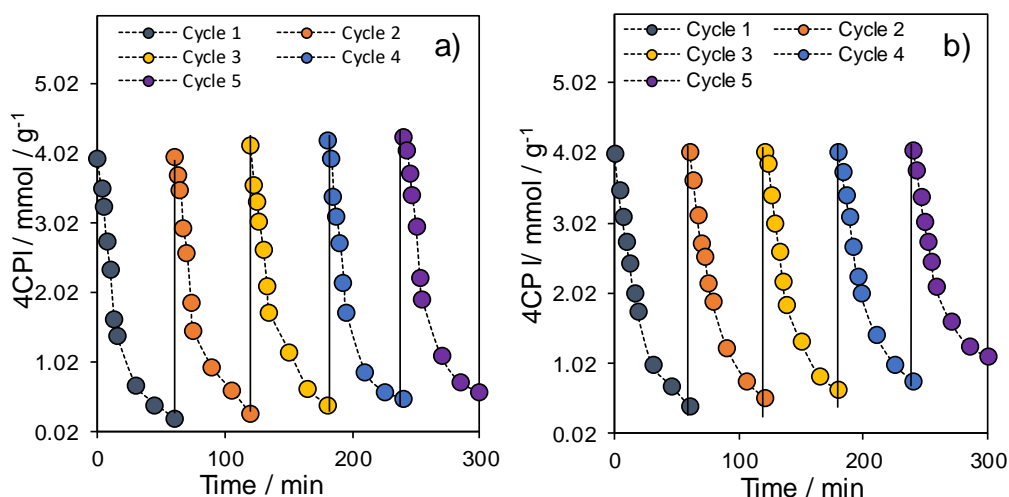


Figure 5.10 Recycles during visible light photocatalytic 4-CP degradation using a) Pompon Dahlia-like hierarchical $\text{Cu}_2\text{O}/\text{rGO}$ nanocomposite and b) Cu_2O .

$\text{Cu}_2\text{O}/\text{rGO}$ and Cu_2O decomposed 4-CP under visible light irradiation consistently for five cycles and showed slight reduction in decomposition after each cycle, as shown in Figure 5.10. After the first cycle over 99% of 4-CP was degraded, and on the third cycle 89% of 4-CP decomposed at the 3-hour mark. After the fifth cycle, approximately a total of 85% of 4-CP was decomposed. In comparison, Cu_2O decomposed 10% 4-CP in the first cycle, and after five cycles (at 5-hour mark), 73% of 4-CP degraded under visible light. This

suggest that rGO enhances catalyst photostability, as 12% more 4-CP was decomposed after 5 hours of repeated decomposition. The integration of rGO as a catalyst support to increase the stability is essential in practical applications³⁷. Furthermore, the large contact area provided by the planar structure of rGO sheets can interact with Cu₂O nanospheres, enhancing the interfacial contact³⁸.

5.6. Photoelectrochemical analysis

The effect of formation between the hierarchical Cu₂O aggregates and rGO nanosheets on charge separation, charge transfer resistance, and charge recombination was further explored by transient photocurrent measurements under chopped light illumination and resulting EIS (Nyquist) and Mott-Schottky analysis (Figure 5.11). The maximum photocurrent of Cu₂O/rGO was approximately two times higher than that of the Cu₂O aggregates; which indicates more redox equivalents are available for photocatalytic reactions.

Electrochemical impedance spectroscopy provides insight into the effectiveness of rGO and Cu₂O as a photoelectrode. Nyquist plots were studied at 0 V vs. RHE under illumination. The semicircle in the Nyquist plot represents the charge transfer process, and the semicircle diameter indicates the charge transfer resistance. As shown in Figure 5.11b, Cu₂O/rGO has a smaller semicircle than hierarchical Cu₂O under illumination, which suggests that rGO facilitates electron migration across the electrode or at the electrode/electrolyte interface³⁹.

The Mott Schottky plots (Figure 5.11c) provide insight into the flat-band potential and majority carrier density of a semiconductor. Negative slopes were obtained for the hierarchical Cu₂O and Cu₂O/rGO nanocomposite, consistent with p-type semiconductors. The x-axis intercept shows the flat band potentials of Cu₂O and Cu₂O/rGO nanocomposite are 1.1 V and 0.98 V, respectively. The slope of the linear portion of the curve in a Mott-Schottky plot is used to calculate the majority carrier density from the Mott-Schottky equation.

$$\frac{1}{c^2} = \frac{2}{\epsilon\epsilon_0 e N_A} \left(V - E_{fb} - \frac{k_B T}{e} \right) \quad (2.10)$$

Where c is the capacitance, ε is the dielectric constant (7.60 for Cu_2O ⁴⁰), ε_0 is the permittivity of free space, e is the electron charge, N_A is the majority carrier density, V is the applied potential, E_{fb} is the flat-band potential, k_B is the Boltzmann's constant and T is the temperature. The majority carrier densities were $1.5 \times 10^{19} \text{cm}^{-3}$ and $1.7 \times 10^{19} \text{cm}^{-3}$ for hierarchical Cu_2O and $\text{Cu}_2\text{O}/\text{rGO}$ respectively, both higher than Cu_2O ($3.7 \times 10^{17} \text{cm}^{-3}$), CuO ($2.41 \times 10^{18} \text{cm}^{-3}$) and $\text{Cu}_2\text{O}/\text{CuO}$ bilayered composite ($2.5 \times 10^{18} \text{cm}^{-3}$) prepared by thermal oxidation⁴¹, but less than electrodeposited/annealed p-type $\text{Cu}_2\text{O}-\text{CuO}$ thin films ($1.3 \times 10^{20} \text{cm}^{-3}$)⁴².

The similar values of flat-band potentials and N_A shows there is a minor difference in either charge transfer or charge separation between both catalysts, which differs from $\text{Cu}_2\text{O}/\text{CuO}$ bilayered composite. Therefore, the higher photocatalytic activity of hierarchical $\text{Cu}_2\text{O}/\text{rGO}$ for hydrogen production and 4-CP decomposition is related to the broader absorption of visible light and not reduced recombination.

A tentative mechanism for photocatalytic 4-CP oxidative degradation over $\text{Cu}_2\text{O}/\text{rGO}$ is demonstrated in Figure 5.11d. The electrons in Cu_2O valence band are photoexcited into the conduction band and are migrated to rGO sheets under illumination. As a result, Cu_2O valence band holes (h^+) may react with hydroxyl ions from the aqueous solution to form OH radicals, whereas photoexcited electrons trapped by rGO react with dissolved oxygen to form superoxide O_2^- radicals. This may further react with water to produce additional OH through redox reactions.

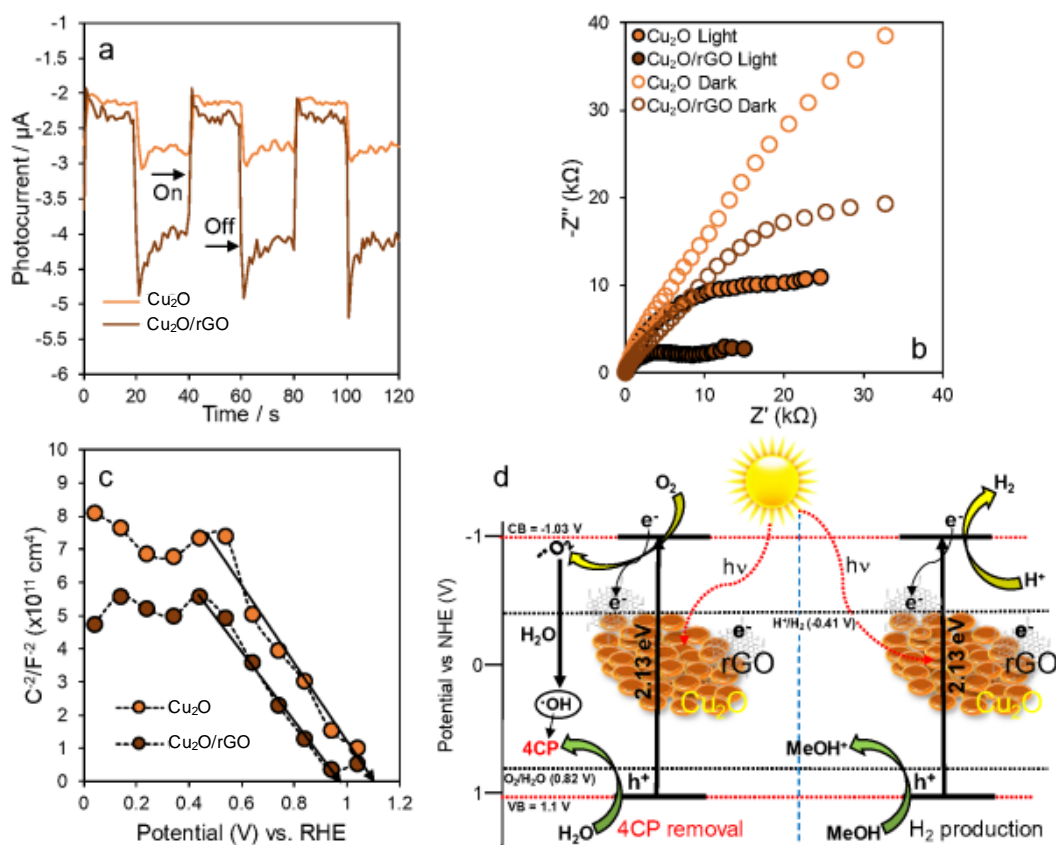


Figure 5.11 (a) Transient photocurrent, (b) EIS (Nyquist) plot at 0 V vs. RHE under illumination, (c) Mott-Schottky plot of Cu₂O and Cu₂O/rGO using 200 W Hg-Xe arc lamp, 0.5 M Na₂SO₄ electrolyte, (d) proposed charge transfer schematic mechanism of Cu₂O/rGO.

5.6.1. Photoelectrochemical stability

The photoelectrochemical stability of hierarchical Cu₂O and Cu₂O/rGO were investigated at 0 V vs. RHE under 20 minute chopped light irradiation over a two-hour period, as tested in literature^{18, 42}. The stability of the photocatalysts were quantified comparing the photocurrent loss after every 20-minute illumination cycle. As shown in Figure 5.12, there is a big difference in photoelectrochemical stability between Cu₂O and Cu₂O/rGO. Hierarchical Cu₂O had a reduction of 10% photocurrent in the second illumination cycle and 27% on the third illumination cycle. In contrast, Cu₂O/rGO had a reduction in

photocurrent by 3% on the second illumination cycle and 5% on the third illumination cycle. The increase in photostability of Cu₂O/rGO is attributed to efficient electron transfer between rGO and Cu₂O.

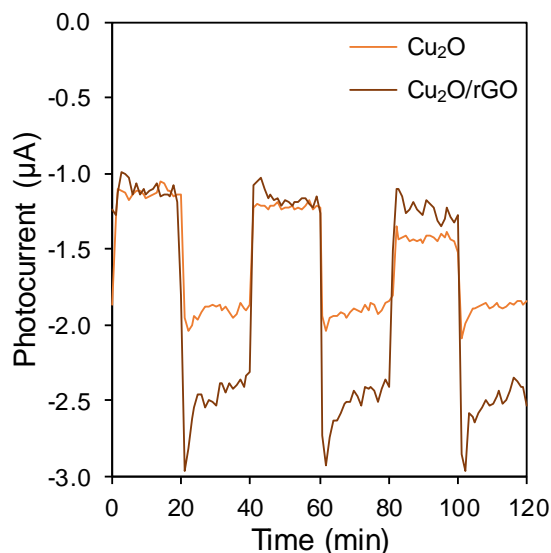


Figure 5.12 Photoelectrochemical stability of Cu₂O and Cu₂O/rGO at 1 V vs. RHE with chopped illumination cycles of 20 minutes.

5.7. Conclusions

In conclusion, Cu₂O/rGO nanocomposite was synthesised by a one-pot electrostatic self-assembly and subsequent low temperature hydrothermal processing. The nanocomposite comprised of 300-500 nm aggregates of 15-30 nm Cu₂O nanocrystals arranged in a Pompom Dahlia(flower)-like structure, in contact with 1 wt.% of rGO nanosheets. This structured photocatalyst offers broad visible light absorption and excellent stability, which resulted in high activity for photocatalytic hydrogen production from water-methanol, and 4-CP decomposition predominately to fumaric acid. Furthermore, the hierarchical Cu₂O/rGO may provide a low-cost approach to solar fuels and environmental remediation of wastewater pollutants.

5.8. References

1. Hara, M.; Kondo, T.; Komoda, M.; Ikeda, S.; Kondo, J.N.; Domen, K.; Hara, M.; Shinohara, K.; Tanaka, A. *Chem. Commun.* **1998**, 357.
2. Luo, J.; Steier, L.; Son, M.-K.; Schreier, M.; Mayer, M.T.; Gratzel, M.; *Nano. Lett.* **2016**, *16*, 1848.
3. Chakravarty, A.; Bhowmik, K.; Mukherjee, A.; De, G. *Langmuir.* **2015**, *31*, 5210.
4. An, X.; Li, K.; Tang, J. *ChemSusChem.* **2014**, *7*, 1086.
5. Chen, R.; Pang, S.; An, H.; Zhu, J.; Ye, S.; Gao, Y.; Fan, F.; Li, C. *Nat. Energy.* **2018**, *3*, 655.
6. Sahoo, S.; Husale, S.; Colwill, B.; Lu, T.-M.; Nayak, S.; Ajayan, P.M. *ACS Nano.* **2009**, 3935.
7. Wang, W.Z.; Wang, G.; Wang, X.S.; Zhan, Y.; Liu, Y.; Zheng, C.L. *Adv. Mater.* **2002**, *14*, 67.
8. Huang, W.-C.; Lyu, L.-M.; Yang, Y.-C.; Huang, M.H. *J. Am. Chem. Soc.* **2011**, *134* 1261.
9. Jiao, S.; Xu, L.; Jiang, K.; Xu, D. *Adv. Mater.* **2006**, *18*, 1174.
10. Xu, H.; Wang, W. *Angew. Chem. Int. Ed.* **2007**, *46*, 1489.
11. Ran, J.; Zhang, J.; Yu, J.; Jaroniec, M.; Qiao, S.Z. *Chem. Soc. Rev.* **2014**, *43*, 7787.
12. Parlett, C.M.A.; Wilson, K.; Lee A.F. *Chem. Soc. Rev.* **2013**, *42*, 387.
13. Novoselov, K.S.; Geim, A.K.; Morozov, S.V.; Jiang, D.; Zhang, Y.; Dubonos, S.V.; Grigorieva, I.V.; Firsov, A.A. *Science.* **2004**, *306*, 666.
14. Li, F.; Zhang, L.; Tong, J.; Liu, Y.; Xu, S.; Cao, Y.; Cao, S. *Nano. Energy.* **2016**, *27*, 320.
15. Liang, Y.; Li, Y.; Wang, H.; Zhou, J.; Wang, J.; Regier, T.; Dai, H. *Nat. Mater.* **2011**, *10*, 780.
16. Xiang, Q.; Cheng, B.; Yu, J. *Angew. Chem. Int. Ed.* **2015**, *54*, 11350.
17. Gan, Z.; Wu, X.; Meng, M.; Zhu, X.; Yang, L.; Chu, P.K. *ACS Nano*, **2014**, *8*, 9304.
18. Zhang, Z.; Dua, R.; Zhang, L.; Zhu, H.; Zhang, H.; Wang, P. *ACS Nano.* **2013**, *7*, 1709.
19. Yang, D.; Velamakanni, A.; Bozoklu, G.; Park, S.; Stoller, M.; Piner, R.D.; Stankovich, S.; Jung, I.; Field, D.A.; Ventrice Jr.; C.A.; Ruoff, R.S. *Carbon.* **2009**, *47*, 1.
20. Chua, C.K.; Pumera, M. *Chem. Commun.* **2016**, 52, 72.
21. Sun, S.; Zhang, X.; Song, X.; Liang, S.; Wang, L.; Yang, Z. *CrystEngComm.* **2012**, *14*, 3545.
22. Li, Q.; Guo, B.; Yu, J.; Ran, J.; Zhang, B.; Yan, H.; Gong, J.R. *J. Am. Chem. Soc.* **2017**, *133*, 10878.
23. Wang, J.T.-W.; Ball, J.M.; Barea, E.M.; Abate, A.; Alexander-Webber, J.A.; Huang, J.; Saliba, M.; MoraSero, I.; Bisquert, J.; Snaith, H.J.; Nicholas, R.J. *Nano. Lett.* **2014**, *14*, 724.
24. Zou, W.; Zhang, L.; Liu, L.; Wang, X.; Sun, J.; Wu, S.; Deng, Y.; Tang, C.; Gao, F.; Dong, L. *Appl. Catal. B-Environ.* **2016**, *181*, 495.
25. Kuo, C.H.; Chen, C.H.; Huang, M.H. *Adv. Funct. Mater.* **2007**, *17*, 3773.
26. Liu, J.; Ke, J.; Li, D.; Sun, H.; Liang, P.; Duan, X.; Tian, W.; Tadè, M.O.; Liu, S.; Wang, S. *ACS Appl. Mater. Interfaces.* **2017**, *9*, 11678.
27. Deng, S.; Tjoa, V.; Fan, H.M.; Tan, H.R.; Sayle, D.C.; Olivo, M.; Mhaisalkar, S.; Wei, J.; Sow, C.H.; Reduced graphene oxide conjugated Cu₂O nanowire mesocrystals for high-performance NO₂ gas sensor, *J. Am. Chem. Soc.* **2012**, *134*, 4905.
28. Xu, L.; Zhang, F.; Song, X.; Yin, Z.; Bu, Y. *J. Mat. Chem. A.* **2015**, *3*, 5923.

29. Mateo, D.; Esteve-Adell, I.; Albero, J.; Primo, A.; Garcìa, H. *Appl. Catal. B-Environ.* **2017**, *201*, 582.
30. Kakuta, S.; Abe, T. *Electrochem. Solid State Lett.* **2009**, *12*, 1.
31. Hara, M.; Kondo, T.; Komoda, M.; Ikeda, S.; Kondo, J. N.; Domen, K.; Hara, M.; Shinohara, K.; Tanaka, A. *Chem. Commun.* **1998**, 357.
32. Karthikeyan, S.; Kumar, S.; Durndell, L.J.; Isaacs, M.A.; Parlett, C.M.A.; Coulson, B.; Douthwaite, R.E.; Jiang, Z.; Wilson, K.; Lee, A.F. *Chem. Cat. Chem.* **2018**, *10*, 3554.
33. Kumar, S.; Parlett, C.M.A.; Isaacs, M.A.; Jowett, D.V.; Douthwaite, R.E.; Cockett, M.C.R.; Lee, A.F. *Appl. Catal. B-Environ.* **2016**, *189*, 226.
34. Barreca, D.; Fornasiero, P.; Gasparotto, A.; Gombac, V.; Maccato, C.; Montini, T.; Tondello, E. *Chem. Sus. Chem.* **2009**, *2*, 230.
35. Barbero, N.; Vione, D. *Environ. Sci. Technol.* **2016**, *50*, 2130.
36. Li, Y.; Sun, Z.; Zhu, S.; Liao, Y.; Chen, Z.; Zhang, D. *Carbon.* **2015**, *94*, 599.
37. Cui, Y.; Huang, J.; Fu, X.; Wang, X. *Catal. Sci. Technol.* **2012**, *2*, 1396.
38. Li, B.; Cao, H.; Yin, J.; Wu, Y. A.; Warner, J. H. *J. Mater. Chem.* **2012**, *22*, 1876.
39. Yang, Y.; Xu, D.; Wu, Q.; Diao, P. *Sci. Rep.* **2016**, *6*, 35158.
40. Zhang, Z.; Wang, P. *J. Mat. Chem.* **2012**, *22*, 2456.
41. Wang, P.; Wu, H.; Tang, Y.; Amal, R.; Ng, Y.H. *J. Phys. Chem. C.* **2015**, *119*, 26275.
42. Tran, P.D.; Batabyal, K.S.; Pramana, S.S.; Barber, J.; Wong, L.H.; Loo, S.C.J. *Nanoscale.* **2012**, *4*.

Chapter 6

Two-dimensional carbon enhanced structural stability of BiVO₄

In Chapter 6, quantum dot BiVO₄ on reduced graphene oxide (QD-BiVO₄/rGO) was synthesised by a facile one-pot solution phase approach. QD-BiVO₄/rGO was fabricated using triethanolamine in the presence of a stabilising agent. QD-BiVO₄/rGO showed greater photocatalytic activity towards bisphenol A removal (as the organic pollutant), where QD-BiVO₄/rGO had 4 times higher decomposition rate than BiVO₄. Hydrogen evolution under visible light was higher for QD-BiVO₄/rGO at 68 μmol g⁻¹ compared to 36.9 μmol g⁻¹ of QD-BiVO₄. Furthermore, the photocatalyst efficiency was confirmed by investigating the photoelectrochemical properties, electronic properties, energy band structures and detailed mechanistic studies.

6.1. Introduction

BiVO₄ is a n-type semiconductor with a band gap of 2.4 eV and is widely used for environmental remediation and oxygen evolution under visible light¹. However, H₂ evolution using BiVO₄ has not been consistently reported in research because the conduction band (CB) position of BiVO₄ is near the reduction potential of water, so band engineering is needed to adjust the band position for H₂ evolution². Semiconductor quantum dots are successful in water splitting and organic pollutant decomposition under visible light³⁻⁶. Sun et al. fabricated QD-BiVO₄⁷, which exhibited an elevated CB position that was more negative than the redox potential of H⁺/H₂ to split water into hydrogen. Also, Wu et al. reported carbon dots/QD-BiVO₄ with high optical absorption coefficient and stability, which increased photocatalytic activity to produce H₂ (0.92 μmol.h⁻¹)⁸.

Reduced graphene oxide (rGO) are promising 2D nanomaterials that have high surface area with excellent optical, electrical and mechanical properties⁹. When hybridised with a metal oxide photocatalyst, graphene can enhance charge transfer properties and increase the stability of otherwise unstable semiconductors¹⁰. Graphene also acts as a stabiliser against

aggregating nanoparticles by strong van der Waals forces between graphene layers¹¹. However, there are still some necessary studies needed on electron migration pathways of photogenerated electron-hole pairs and structural stability of heterojunctions between graphene and semiconductors.

Therefore, in this work, QD-BiVO₄/rGO nanocomposite was synthesised by solution phase chemistry in acidic conditions. The photocatalytic activity of QD-BiVO₄/rGO was examined by the photodecomposition of Bisphenol-A, hydrogen evolution and photoelectrochemical (PEC) measurements.

6.2. Catalyst synthesis

The synthesis of GO was as described previously by a modified Hummer's method¹², where 10 mg of GO is dispersed in 100 ml deionised water and ultrasonicated for 2 hours. The quantum dot (QD)-BiVO₄/rGO was fabricated by solution phase chemistry followed by hydrothermal synthesis. 50 ml of 0.1 M bismuth (III) nitrate was mixed with 20 ml of 0.2 M ammonium metavanadate and 0.5 ml of 0.06 M polyethylene glycol (PEG), observing a colour change to red. PEG was used as a stabilising agent. The mixture was poured into GO solution and 10 ml of 2 M HNO₃ was poured dropwise at 400 RPM at 50 °C for 25 minutes, observing a colour change to yellow.

5 ml mixture of 0.1 M C₂H₇NO (MEA) was poured dropwise to the yellow mixture, and stirred at 50 °C for 10 minutes, producing a yellow precipitate. The initial electrostatic interaction with Bi-PEG complex and simultaneous addition of MEA leads to a suitable pH for favoured BiVO₄ crystal formation. The resulting mixture was transferred to a 200ml Teflon-lined autoclave and heated at 160 °C for 24 hours, and then cooled to room temperature. The resulting sample was centrifuged at 10,000 RPM for 7 minutes and had several water and ethanol washes before it was vacuum dried for 12 hours at 65°C. QD-BiVO₄ was synthesised using the same method without adding GO and PEG. 5 ml of 0.5 M ammonium hydroxide was used in this case instead of MEA.

6.3. Characterisation

6.3.1. Microscopy studies

The successful synthesis of QD-BiVO₄/rGO and particle size distributions were illustrated with TEM images in Figure 6.1. The images identified the formation of 0D quantum dot sized BiVO₄ with 2D rGO sheets (Figure 6.1d), with an average particle size distribution of 150 nm (Figure 6.1b inset). The dispersion with rGO as a support was shown in Figure 6.1e, which suggests controlled particle size quantum dots (between 1.5-2.5 nm) highly dispersed on the 2D graphene sheets. The interplanar lattice spacing of 0.307 nm (Figure 6.1f) corresponds to BiVO₄ with interconnected quantum dots⁸ that have a particle diameter of 2.5 nm (Figure 6.1e inset).

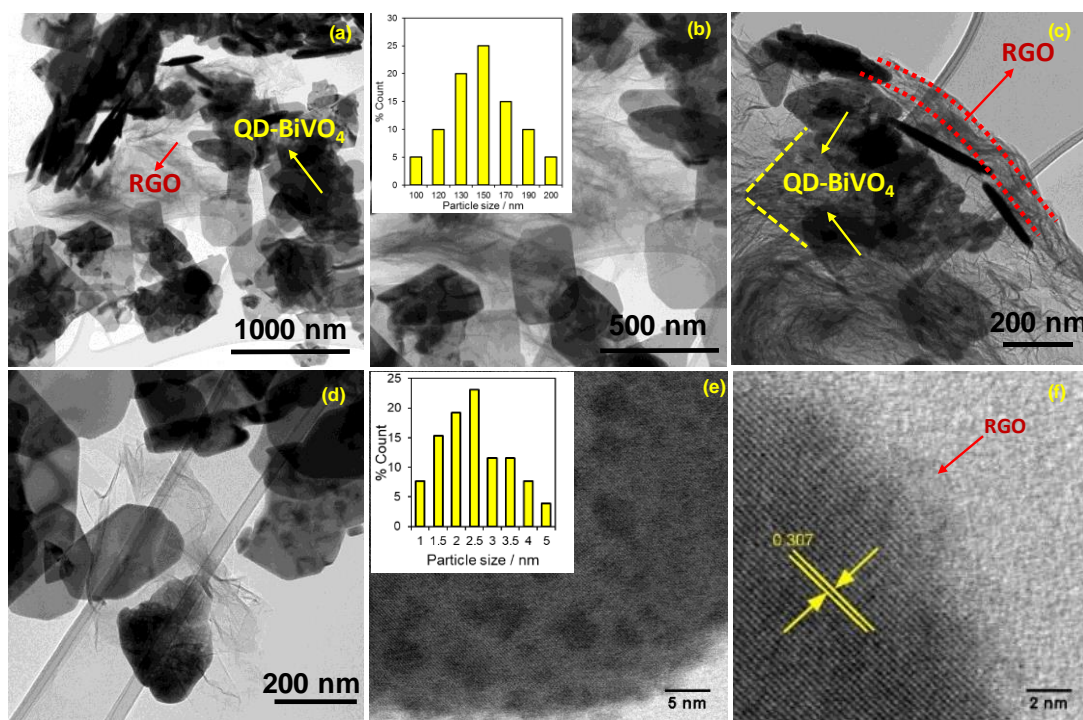


Figure 6.1 TEM images of QD-BiVO₄/rGO at various magnifications and (b,e) insets corresponding to particle size distributions.

Furthermore, TEM images of BiVO₄ and QD-BiVO₄ were presented in Figure 6.2 and shows average particle size distribution of BiVO₄ were around ~160-200 nm (Figure 6.2d). From the microscopy studies, it is suggested the quantum dots were formed with low-temperature hydrothermal synthesis using PEG. PEG was used a stabilising agent and the particle size is dependent on amalgamation time and temperature of the reaction¹³. PEG and rGO were used for the synthesis of QD-BiVO₄/rGO because they favour the formation of a metal-polymer matrix. In addition, ethanolamine was used as an active surface initiator, which formed an aerogel-like assembly by crosslinking the complex¹⁴. It was concluded from previous reports that size and shape of quantum dots are controlled by in-situ polymerisation using polymeric material^{15,16}.

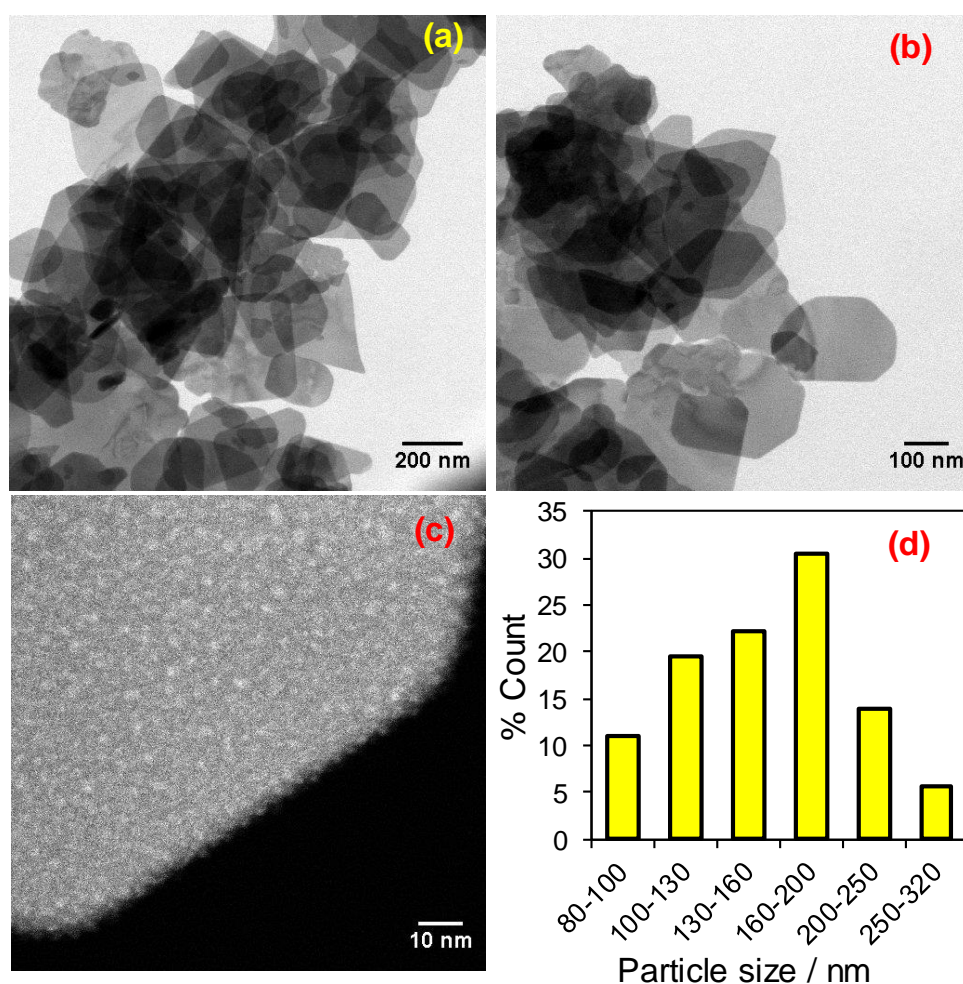


Figure 6.2 a-b) TEM images of BiVO₄, c) TEM image of QD-BiVO₄, d) corresponding particles size distributions.

6.3.2. Photophysical properties

Commercial BiVO_4 was used to compare with QD-BiVO_4 and $\text{QD-BiVO}_4/\text{rGO}$. Their crystallinity was examined using XRD patterns (Figure 6.3a). The major XRD diffraction peaks at 18.67° , 28.96° , 30.54° , 34.51° , 39.78° , 42.49° , 46.64° and 52.23° indexed as (101), (112), (004), (200), (211), (015), (204) and (116) reflections, which are all assigned to a monoclinic scheelite structure of BiVO_4 (JCPDS 14-0688)¹⁷. There are peaks that are indicative of tetragonal phase (JCPDS 14-0133)¹⁸ at 23.65° and 32.46° for both QD-BiVO_4 and $\text{QD-BiVO}_4/\text{rGO}$. The average crystallite size of BiVO_4 , QD-BiVO_4 and $\text{QD-BiVO}_4/\text{rGO}$ were 32.4, 29.2 and 26 nm respectively, calculated using the Scherrer equation.

$$\tau = \frac{K\lambda}{\beta \cos \theta} \quad (2.2)$$

This indicated the formation of smaller crystallite size in the $\text{QD-BiVO}_4/\text{rGO}$ nanocomposite, but it is important to know that the estimated differences in crystallite size are insignificant.

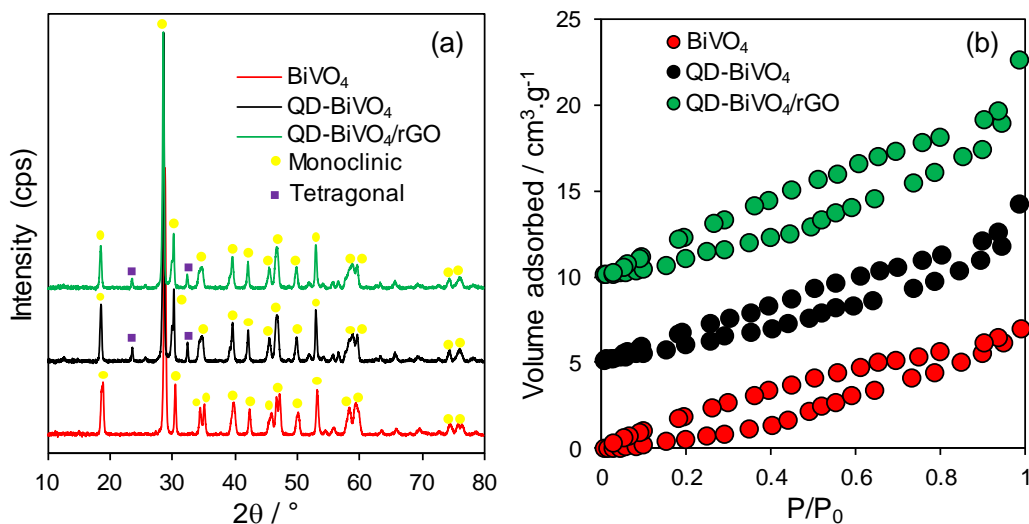


Figure 6.3 a) XRD pattern, b) N_2 adsorption-desorption isotherm of synthesised BiVO_4 , QD-BiVO_4 and $\text{QD-BiVO}_4/\text{rGO}$.

Figure 6.3b illustrates N_2 adsorption-desorption isotherms and showed the surface area of QD-BiVO₄/rGO and QD-BiVO₄ was 6.20 m²·g⁻¹ and 5.23 m²·g⁻¹ respectively. The higher surface area of QD-BiVO₄/rGO suggests more surface-active sites available for photocatalytic processes, approximately 3 times higher than pure BiVO₄ (1.84 m²·g⁻¹). Diffuse reflectance UV-Vis spectra (DRUVS) determined the absorbance properties of BiVO₄, QD-BiVO₄ and QD-BiVO₄/rGO in Figure 6.4. BiVO₄ displayed a strong absorption at shorter wavelengths, which is characteristic of scheelite BiVO₄. In contrast, QD-BiVO₄/rGO exhibited a red shift, which indicates the optical energy band gap elevated in the presence of QDs and rGO. Furthermore, the red shift is linked to the colour change between QD-BiVO₄ and QD-BiVO₄/rGO (from yellow to yellowish green). The physical driving force for the apparent lattice strain and colour evolution is presumed to enlarge the CB position and shifts the band gap^{19,20}.

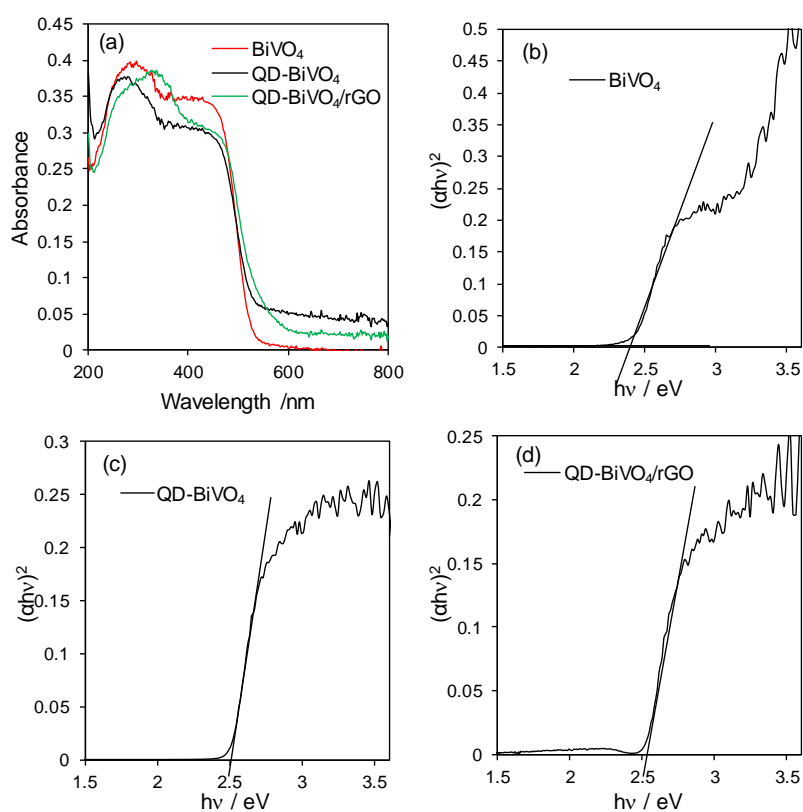


Figure 6.4 (a) DRUVS Absorption spectra, (b-d) corresponding Tauc plot of BiVO₄ and QD-BiVO₄ with QD-BiVO₄/rGO.

The optical band gaps E_{BG} were calculated from the Tauc plots (Figures 6.4b-d):

$$\alpha h\nu = C(h\nu - E_{BG})^n \quad (2.6)$$

where C is the proportionality constant and α is the absorption coefficient determined from the Kubelka-Munk formula.

$$\alpha = \frac{(1-R)^2}{2R} \quad (2.7)$$

The band gap increased with the addition of rGO from 2.39 to 2.52 eV, as shown by direct comparison in band gaps between BiVO₄, QD-BiVO₄ and QD-BiVO₄/rGO in Figure 6.5a. The band gap of QD-BiVO₄ is higher than reported values due to the small particle size of QDs, which is affected by the quantum confinement effect and surface defects^{21,22}. The valence band of the photocatalyst was determined by valence band (VB) XPS, as shown in Figure 6.5b. The VB edges for BiVO₄, QD-BiVO₄, QD-BiVO₄/rGO is +2.00, +1.82 and +1.48 eV respectively. Thus, the conduction band (CB) edges were calculated from the band gap, which are -0.39 eV, -0.68 eV, -1.04 eV for BiVO₄, QD-BiVO₄, QD-BiVO₄/rGO respectively.

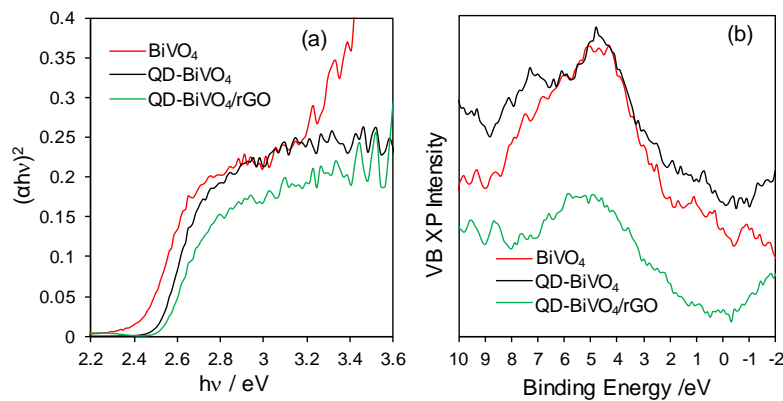


Figure 6.5 (a) DRUVS Tauc plot, (b) valence band XPS of BiVO₄, QD-BiVO₄ and QD-BiVO₄/rGO.

6.3.3. XPS analysis

The chemical and oxidation states, as well as rGO and BiVO₄ interaction in BiVO₄, QD-BiVO₄ and QD-BiVO₄/rGO were analysed by high-resolution XPS in Figure 6.6. Bi4f_{5/2} and Bi4f_{7/2} XPS signals have binding energies at 164.56 eV and 159.16 eV respectively, which confirms BiVO₄ has Bi species in +3 oxidation state⁸. The V2p_{1/2} and V2p_{3/2} binding energies observed at 524.56 eV and 516.8 eV are assigned to V species in +5 oxidation state. A small binding energy shift was observed between Bi 4f_{5/2} (0.38 eV) and Bi 4f_{7/2} (0.94 eV) in QD-BiVO₄/rGO compared with QD-BiVO₄. There is an indication on QD-BiVO₄ of shoulder peaks which suggests an extra oxidation state or other impurities.

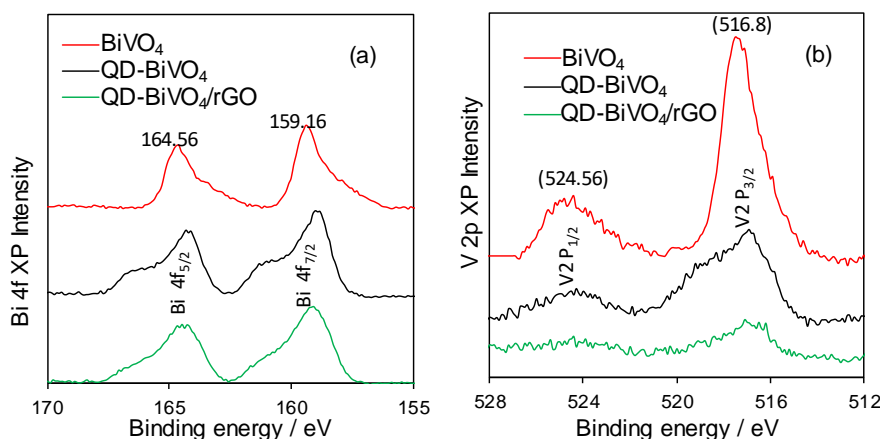


Figure 6.6 (a) Bi4f XPS, (b) V2p XPS offset for clarity.

To further confirm the incorporation of rGO, the core-level C1s XPS of BiVO₄, QD-BiVO₄ and QD-BiVO₄/rGO catalysts were presented in Figure 6.7. The interaction between BiVO₄ and rGO was confirmed by the π -orbital in the C=O bond. The electron cloud in oxygen species were more localised to interact with metal 'd- π ' orbitals, which is responsible for combining the two peaks into one²³. As shown in Figure 6.7, C1s binding energies were 284.6 (sp² C-C), 286.04 (C-O), 288.34 eV (C=O) and 290.10 eV (O-C=O) respectively. The most prevalent peak was sp² bonded C-C, which exists in graphene²⁴. The interaction between rGO and either Bi or V caused a shift of core level C1s peaks to a lower binding

energy²⁵. The physicochemical properties of BiVO₄, QD-BiVO₄ and QD-BiVO₄/rGO are summarised in Table 6.1.

Table 6.1 Physicochemical properties of BiVO₄, QD-BiVO₄ and QD-BiVO₄/rGO.

Sample	Average particle size (nm) (TEM)		Crystallite size (112), nm (XRD)	Surface area (m ² .g ⁻¹)	Band gap (eV) (DRUVS)	VB edge potential (eV) (XPS)	CB edge potential (eV) (XPS)
	Bulk	QDs					
BiVO ₄	300-400	-	32.39	1.84	2.39	-0.39	+2.00
QD-BiVO ₄	160-200	2-4	29.17	5.23	2.50	-0.68	+1.82
QD-BiVO ₄ /rGO	150	2-3	25.99	6.20	2.52	-1.04	+1.48

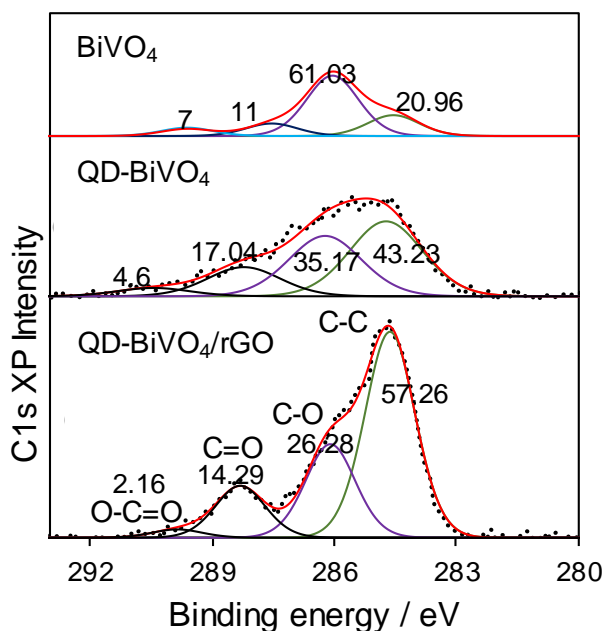


Figure 6.7 Core-level C 1s XPS of BiVO₄ and QD-BiVO₄ with QD-BiVO₄/rGO.

6.4. Hydrogen evolution

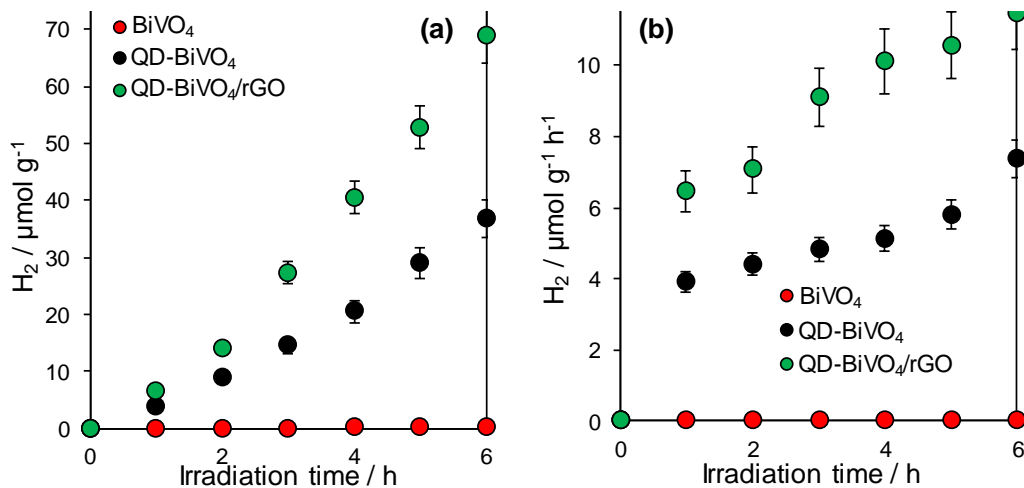


Figure 6.8 Schematic band positions of $BiVO_4$, $QD-BiVO_4$ and $QD-BiVO_4/rGO$.

H^+ reduction and water splitting are not suitable to test hydrogen evolution of $BiVO_4$ due to its insufficient reduction power in the CB position (-0.39 eV), which is located below the hydrogen evolution potential at pH 7 (-0.4 eV)⁷. In contrast, $QD-BiVO_4$ and $QD-BiVO_4/rGO$ photocatalyst can reduce H^+ to H_2 due to their elevated CB position (-0.68 eV and -1.04 eV for $QD-BiVO_4$ and $QD-BiVO_4/rGO$ respectively), which has enough redox potentials for photocatalytic water splitting into H_2 (Figure 6.8).

The visible light H_2 evolution of $BiVO_4$ ($0.03 \mu mol \cdot g^{-1} \cdot h^{-1}$), $QD-BiVO_4$ ($7.4 \mu mol \cdot g^{-1} \cdot h^{-1}$) and $QD-BiVO_4/rGO$ ($11.5 \mu mol \cdot g^{-1} \cdot h^{-1}$) were recorded using pure water with Na_2SO_3 as a hole scavenger. The hydrogen evolution of $QD-BiVO_4/rGO$ is 1.6-fold higher than $QD-BiVO_4$ and $QD-BiVO_4$ is approximately 240-fold higher $BiVO_4$ (Figure 6.9).

The improved structural and electronic properties of quantum dots in $QD-BiVO_4$ are responsible for the drastic increase in visible light photocatalytic H_2 evolution. In addition, $BiVO_4$ is highly dispersed onto the rGO, which acts as electron acceptors and mediators. This may trap photoinduced electrons to enhance visible light activity on the catalyst surface. Also, as shown by DRUVS in Figure 6.5a, the rGO layer may extend the light absorption in solar spectrum and is expected to drive hole reaction efficiently to complete the redox reaction to an increasing shift in the CB shown in Figure 6.8.

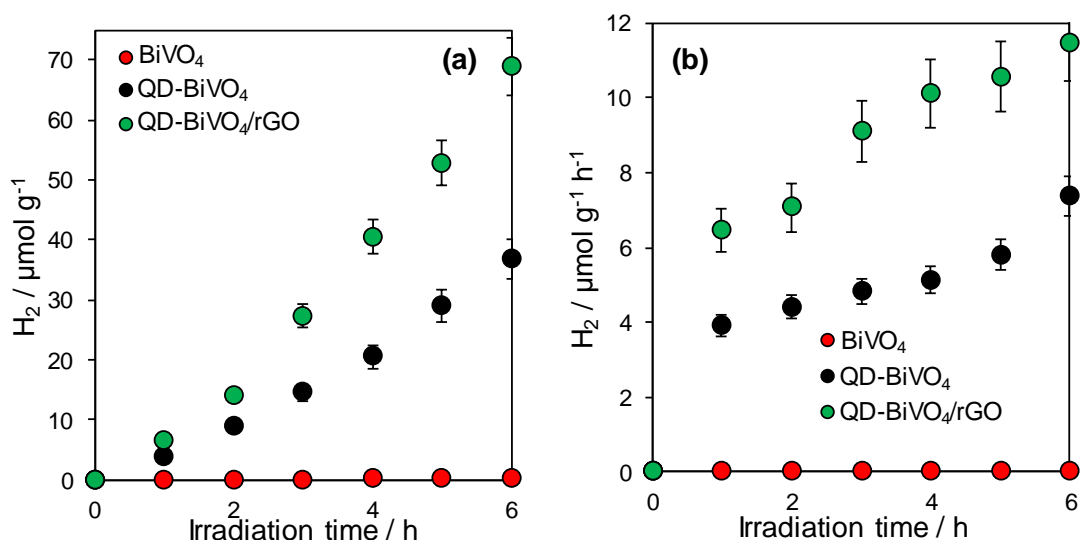


Figure 6.9 Photocatalytic hydrogen evolution under visible light over BiVO₄, QD-BiVO₄ and QD-BiVO₄/rGO (experimental conditions: 50 mg of catalyst with pure water containing 50 ml of 0.5 M Na₂SO₃ (hole scavenger) under visible irradiation by a 200 W Hg-Xe arc lamp).

Figure 6.9 shows the highest hydrogen evolution of QD-BiVO₄ was 36.9 μmol g⁻¹ and 68 μmol g⁻¹ for QD-BiVO₄/rGO, with the apparent quantum efficiency (AQE) of 0.21% and 0.32%, respectively using Equation 2.14.

$$AQE (\%) = \frac{Mol. \text{ reacted electrons per unit time}}{9.94 \times 10^{-8}} \times 100 \quad (2.14)$$

In comparison to the literature, the hydrogen evolution rate of QD-BiVO₄ (average grain size 50 nm) was only 0.23 μmol.h⁻¹, which is much less than the reported QD-BiVO₄⁷. Recently, Wu et al. reported a hybrid carbon dot/BiVO₄ quantum dot (5 nm) composite for H₂ evolution. The H₂ evolution rates were 0.21 μmol h⁻¹ for QDs BiVO₄ and 0.92 μmol h⁻¹ for CDs/ QDs BiVO₄⁸. Other papers reported a higher H₂ evolution rate of 195.6 mmol.h⁻¹ (using 2 ml ethanol sacrificial reagent) for BiVO₄ (particle size 10–20 nm) under UV light using 240 W Hg–Xe lamp but did not report quantum efficiencies²⁶. The highest reported H₂ evolution rate of BiVO₄/rGO was 0.75 μmol h⁻¹ (300 W Xe lamp) in a photoelectrochemical cell with an external bias²⁷.

6.5. Photodecomposition of Bisphenol A

BiVO₄, QD-BiVO₄ and QD-BiVO₄/rGO photocatalysts decomposed bisphenol A (BPA) as the model organic pollutant under visible light. Bisphenol A (BPA) was used in this study instead of dyes as most dyes are exploited in the field of dye sensitised solar cells because photocatalytic mechanism of either dye or photocatalyst cannot be explained²⁸.

The photocatalytic removal of BPA is carried out (50 ml of 4.2×10^{-2} mM) using BiVO₄, QD-BiVO₄ and QD-BiVO₄/rGO under visible light ($\lambda > 420$ nm) irradiation. Initially, aqueous BPA is stirred in the dark for 2 hours to reach an adsorption-desorption equilibrium. The mass normalised initial rates of BiVO₄, QD-BiVO₄, and QD-BiVO₄/rGO were recorded as 1×10^{-2} , 3.5×10^{-2} and 4.5×10^{-2} mmol.g⁻¹.min⁻¹ respectively. QD-BiVO₄/rGO has shown 4 times higher decomposition rate than BiVO₄ and the normalised rates of BPA removal using BiVO₄, QD-BiVO₄ and QD-BiVO₄/rGO were 5.4×10^{-3} , 6.7×10^{-3} and 7.3×10^{-3} mmol.m².g⁻¹.min⁻¹ respectively, presented in Figure 6.10. The reaction rates were proportional to particle size and structure, because faster photoreaction takes place with smaller particle size.

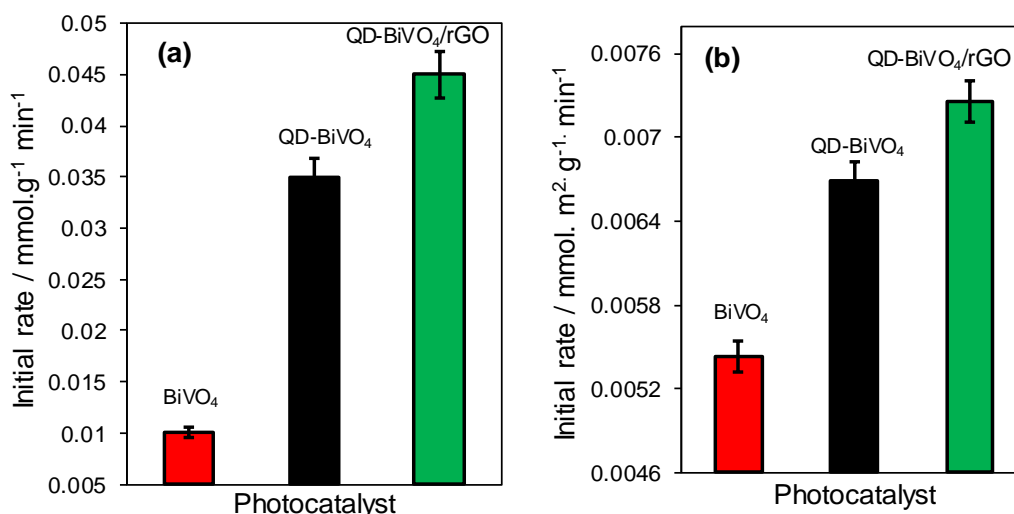


Figure 6.10 (a) Initial rates of Bisphenol A removal, and (b) surface area normalised initial rates of BPA removal over BiVO₄, QD-BiVO₄ and QD-BiVO₄/rGO (Experimental conditions: 50 ml BPA of 4.2×10^{-2} mM, 20 mg catalyst, 200 W Hg-Xe arc lamp with UV cut-off filter).

The irradiated catalyst is proposed to photoinduce holes, which react with water to form hydroxyl radicals ($\bullet\text{OH}$). While, the photoexcited electrons react with oxygen to form superoxide radicals ($\text{O}_2\bullet^-$), which react further with water to generate $\bullet\text{OH}$ radicals via redox reactions.

$$\text{AQE (\%)} = \frac{\text{Mol. reacted electrons per unit time}}{9.94 \times 10^{-8}} \times 100 \quad (2.14)$$

The photocatalytic conversion efficiencies were correlated with the AQE using Equation 2.14, which is 3.35%, 11.73% and 15.08% for BiVO_4 , QD-BiVO_4 , and $\text{QD-BiVO}_4/\text{rGO}$ respectively.

Table 6.2 Photocatalytic pollutant decomposition using nanostructured BiVO_4 photocatalysts under visible light irradiation.

Photocatalyst	Pollutant	Experimental details	Rate constant $\times 10^{-3}/\text{min}^{-1}$	AQE (%)	Reference
BiVO_4 nanorods	RhB	100 mg catalyst, 500 W Xe, 10^{-5}M L^{-1} RhB	0.16	-	29
$\text{Co}_3\text{O}_4/\text{BiVO}_4$	Phenol	3g/L catalyst, Phenol, 18mg/L; 1000 W Xe	1	-	30
Pd/BiVO_4	Methyl orange	200 mg catalyst, 12 W lamp, 10 mg L^{-1} MO.	0.033	-	31
$\text{BiVO}_4/\text{Bi}_2\text{O}_2\text{C O}_3$	RhB	100 mg catalyst, 350 W, $2 \times 10^{-5}\text{M L}^{-1}$ RhB	0.32	-	32
QD- BiVO_4/rGO	BPA	200 W, 20 mg catalyst, $4.2 \times 10^{-2}\text{ mM}$ BPA	1.2	2.02	Present work

The AQE of QD-BiVO₄/rGO was 4.5 times higher than BiVO₄, but it was difficult to compare with literature as no AQE was reported via pollution degradation using BiVO₄. Therefore, a collection of nanostructured BiVO₄ catalysts were compared in terms of photodecomposition instead, as shown in Table 6.2.

Overall, the higher amount of photon energies adsorbed on the photocatalyst surface shows higher light utilisation, thereby photoinducing electron-hole pairs. The enhanced photocatalytic oxidation is related to the rate of creation, transport, recombination and reaction of electron-hole charge carriers. This is responsible for the driving force of reduction and oxidation of adsorbates on photocatalyst surfaces^{33,34}. The zero-band gap material, rGO, act as an electron acceptor and mediator³⁵, can trap photoinduced electrons from QD-BiVO₄, which result in more efficient separation of charge-carriers than QD-BiVO₄, and BiVO₄.

6.5.1. Photocatalytic stability

BiVO₄/rGO and BiVO₄ were compared in the photodecomposition of methylene blue (MB) dye under visible light irradiation for 5 continuous cycles (one-hour reaction per cycle),^{36,37} and illustrated a significant difference in decomposition rates, as displayed in Figure 6.11. The photodecomposition efficiency for BiVO₄/rGO decreased slightly after 5 runs, at 98 % decomposition in the first cycle and 93 % of MB dye decomposed on the fifth cycle. In comparison, the ability of BiVO₄ to decompose MB dye under visible light over the same duration was much weaker, as 92% of MB dye decomposed in the first cycle and 62% of MB dye was decomposed in the fifth cycle. This indicates the addition of rGO increases the stability of the photocatalyst greatly, with the ability to decompose nearly 30% more after over 7 hours in the mixture. The stability of rGO is attributed to the large surface area and high dispersion of QD-BiVO₄ on the graphene layer.

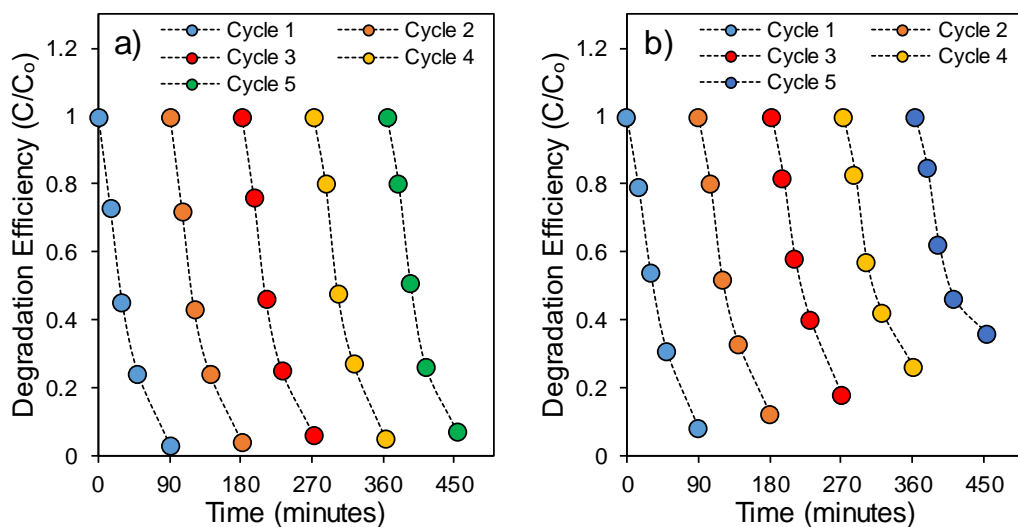


Figure 6.11 Recycles during visible light MB dye degradation over a) BiVO₄/rGO nanocomposite and b) BiVO₄.

6.6. Photoelectrochemical analysis

The enhanced photocatalytic activity of BiVO₄, QD-BiVO₄, and QD-BiVO₄/rGO were investigated by transient photocurrent measurements, carried out under chopped light illumination to investigate the effect of the rGO layer and QDs incorporated in BiVO₄ presented in Figure 6.12. The fast and reproducible photo response of the catalysts were in descending order: QD-BiVO₄/rGO > QD-BiVO₄ > BiVO₄. The photocurrent measurement of QD-BiVO₄/rGO is approximately 1.2 times higher than QD-BiVO₄ and 4 times higher than compared with BiVO₄. This enhanced photocurrent is related to the particle size of the catalyst, as the photocurrent of QD-BiVO₄ is 3.3 times higher than compared with reported BiVO₄⁸. Furthermore, the thin rGO layer increased the photoresponse³⁸, which suggests improved separation of photogenerated electron-hole pairs from BiVO₄.

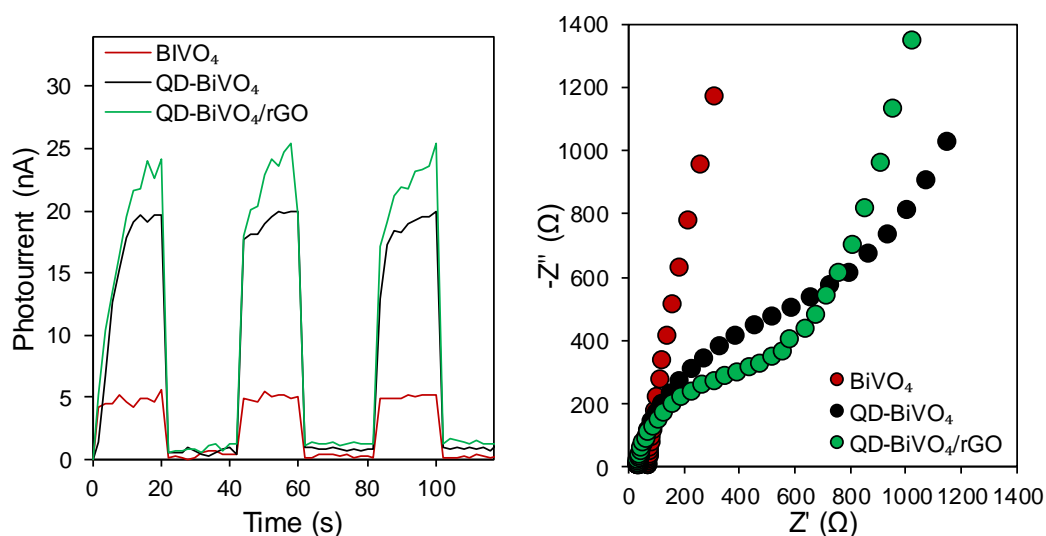


Figure 6.12 (a) Transient photocurrent, (b) Electrochemical Impedance Spectroscopy (EIS) of BiVO₄, QD-BiVO₄, QD-BiVO₄/rGO using 200 W Hg-Xe arc lamp and 0.5 M Na₂SO₄ electrolyte under visible light illumination ($\lambda > 420$ nm).

Moreover, investigated the charge transfer behaviour of the synthesised photocatalysts was investigated by electrochemical impedance spectroscopy (EIS) shown in Figure 6.12b and 6.13. In a Nyquist plot, the diameter of the impedance curve indicates the charge transfer resistance of the material³⁹. QD-BiVO₄/rGO exhibited a smaller diameter than QD-BiVO₄ and BiVO₄, which means it has a lower charge transfer resistance. This is because the rGO layer enables electron transfer from the space charge region to the semiconductor-electrolyte surface thus reducing the recombination rate, which is consistent with other reports^{40,41}.

Mott Schottky plot was used to study the donor density and flat-band potential under illumination. The QD-BiVO₄/rGO, QD-BiVO₄ and BiVO₄ photocatalysts were n-type semiconductors, as they have a positive slope (Figure 6.13). QD-BiVO₄/rGO shows the smallest slope, which suggests an increased donor density⁴². The flat-band potentials are calculated by x intercepts of the linear section, which are 0.38 V, 0.17 V and 0.15 V vs. RHE for QD-BiVO₄/rGO, QD-BiVO₄ and BiVO₄ respectively.

The majority carrier density is calculated by the Mott Schottky equation.

$$\frac{1}{c^2} = \frac{2}{\epsilon\epsilon_0 e N_A} \left(V - E_{fb} - \frac{k_B T}{e} \right) \quad (2.10)$$

Where c is the capacitance, ϵ is the dielectric constant of $\text{BiVO}_4 = 86^{43}$, ϵ_0 is the permittivity of free space, V is the applied potential and E_{fb} is the flat-band potential. The majority carrier densities for QD- BiVO_4/rGO , QD- BiVO_4 and BiVO_4 are $2.1 \times 10^{18} \text{ cm}^{-3}$, $1.4 \times 10^{18} \text{ cm}^{-3}$ and $1.3 \times 10^{18} \text{ cm}^{-3}$ respectively. The difference in majority carrier density between QD- BiVO_4 and pure BiVO_4 was negligible as both had relatively poor charge transfer compared to QD- BiVO_4/rGO , which indicates the rGO layer increases charge separation efficiency. The transient photocurrents showed a similar trend in Figure 6.12a, as QD- BiVO_4/rGO exhibited the highest photocurrent rGO is a good photogenerated electron acceptor as it is highly conductive⁴⁴. This agrees with the other conclusions in the chapter.

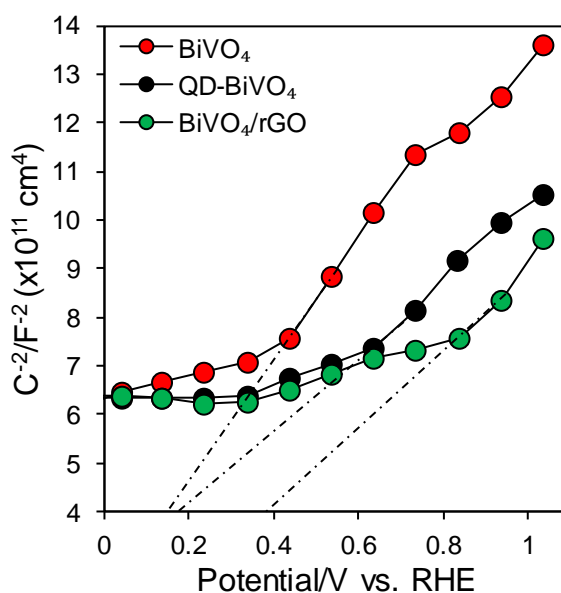


Figure 6.13 Mott Schottky plot of BiVO_4 and QD- BiVO_4 with QD- BiVO_4/rGO .

6.6.1. Photoelectrochemical stability

The stability of bare BiVO_4 and QD- BiVO_4/rGO was tested (Figure 6.14) by transient photocurrent response in a 20 minute on-off illumination cycle, which is used in literature⁴⁵. The photoelectrochemical stability of QD- BiVO_4/rGO was excellent with a slight reduction

in photoresponse in the second and third illumination cycle, by 0.1 μA and 0.16 μA respectively. In contrast, BiVO_4 had a much faster decrease in photocurrent, with a reduction of 0.29 μA in the second illumination cycle and 0.44 μA in the third cycle. The strong photoelectrochemical stability of QD- BiVO_4/rGO is attributed to uniform dispersion of QDs on the rGO layer⁴⁶.

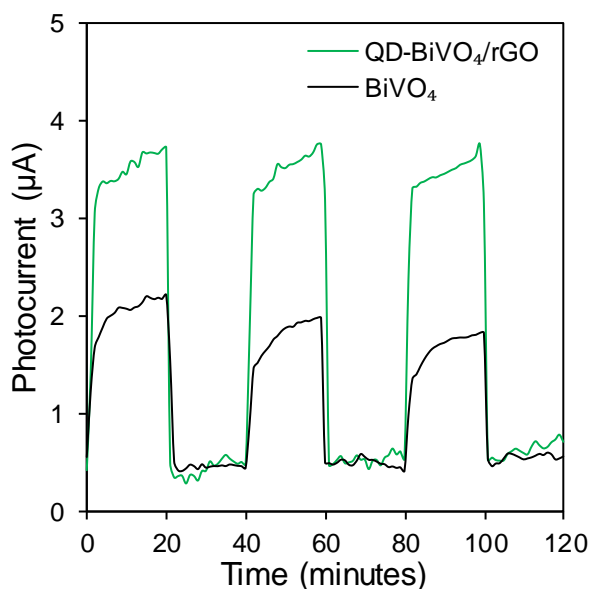


Figure 6.14 Photoelectrochemical stability of BiVO_4 and QD- BiVO_4/rGO at 1 V vs. RHE with chopped illumination cycles of 20 minutes.

6.7. Conclusions

In conclusion, QD- BiVO_4/rGO was fabricated by a one-pot solution phased hydrothermal approach. QD- BiVO_4/rGO exhibited higher photocatalytic activity than BiVO_4 and QD- BiVO_4 in visible light towards BPA photodecomposition and H_2 evolution. This was because the rGO layer act as electron acceptors and mediators, which can trap photoinduced electrons to enhance visible light activity on the catalyst surface. Moreover, H_2 production was indicative of the nanocomposite's high surface area and enhanced light absorption.

The superior photoelectrochemical performance of QD-BiVO₄/rGO suggested the rGO layer increased the photoresponse by more efficient separation of photogenerated electron-hole pairs from BiVO₄. In addition, QD-BiVO₄/rGO has excellent photostability after testing in photodecomposition and transient photocurrent cycles. This research may provide insight to future nanocomposite photocatalysts with differently sized nanostructures.

6.8. References

1. Seabold, J. A.; Choi, K.S. *J. Amer. Chem. Soc.* **2012**, *134*, 2186.
2. McDonald, K. J.; Choi, K.S. *Ener. & Environ. Sci.* **2012**, *5*, 8553.
3. Hou, J.; Yang, C.; Wang, Z.; Jiao, S.; Zhu, H. *App. Catal. B-Environ.* **2013**, *129*, 333.
4. Ge, L.; Zuo, F.; Liu, J.; Ma, Q.; Wang, C.; Sun, D.; Bartels, L.; Feng, P. *J. Phys. Chem. C.* **2012**, *116*, 13708.
5. Gao, W.; Wang, M.; Ran, C.; Li, L. *Chem. Commun.* **2015**, *51*, 1709.
6. Yu, L.; Huang, Y.; Xiao, G.; Li, D. *J. Mater. Chem. A.* **2013**, *1*, 9637.
7. Sun, S.; Wang, W.; Li, D.; Zhang, L.; Jiang, D. *ACS Catal.* **2014**, *4*, 3498.
8. Wu, X.; Zhao, J.; Guo, S.; Wang, L.; Shi, W.; Huang, H.; Liu, Y.; Kang, Z. *Nanoscale.* **2016**, *8*, 17314.
9. Deng, D.; Novoselov, K.S.; Fu, Q.; Zheng, N.; Tian, Z.; Bao, X. *Nature Nanotechnology.* **2016**, *11*, 218.
10. Hou, Y.; Zuo, F.; Dagg, A.; Feng, P. *Nano Letters.* **2012**, *12*, 6464.
11. Quanjun, X.; Bei, C.; Jianguo, Y. *Angew. Chem.Int. Ed.* **2015**, *54*, 11350.
12. Yang, D.; Velamakanni, A.; Bozoklu, G.; Park, S.; Stoller, M.; Piner, R.D.; Stankovich, S.; Jung, I.; Field, D.A.; Ventrice Jr.; C.A.; Ruoff, R.S. *Carbon.* **2009**, *47*, 1.
13. Xie, M.; Zhang, Z.; Han, W.; Cheng, X.; Li, X.; Xie, E. *J. of Mater.s Chem. A.* **2017**, *5*, 10338.
14. Li, Y.; Sun, Z.; Zhu, S.; Liao, Y.; Chen, Z.; Zhang, D. *Carbon.* **2015**, *94*, 599.
15. Li, H.; Yu, K.; Lei, X.; Guo, B.; Fu, H.; Zhu, Z. *J. of Phys. Chem. C.* **2015**, *119*, 22681.
16. Kakihana, M. *J. Sol-Gel Sci. & Tech.* **1996**, *6*, 7.
17. Ge, M.; Liu, L.; Chen, W.; Zhou, Z. *Cryst.Eng.Comm.* **2012**, *14*, 1038.
18. Zhao, Y.; Li, R, Mu, L.; Li, C. *Crys. Grow. & Des.* **2017**, *17*, 2923.
19. Jo, W. J.; Kang, H. J.; Kong, K.J.; Lee, Y. S.; Park, H.; Lee, Y.; Buonassisi, T.; Gleason, K. K.; Lee, J. S. *Proc. Nat. Acad. of Sci.* **2015**, *112*, 13774.
20. Yu, J.; Kudo, A. *Adv. Func. Mater.* **2006**, *16*, 2163.
21. Townsend, T. K.; Browning, N. D.; Osterloh, F. E. *ACS Nano.* **2012**, *6*, 7420.
22. Sun, J.; Li, X.; Zhao, Q.; Tadé, M, O.; Liu, S. *J. Mater. Chem. A.* **2015**, *3*, 21655.
23. Karim, M. R.; Shinoda, H.; Nakai, M.; Hatakeyama, K.; Kamihata, H.; Matsui, T.; Taniguchi, T.; Koinuma, M.; Kuroiwa, K.; Kurmoo, M. *Adv.Func. Mater.* **2013**, *23*, 323.
24. Stankovich, S.; Dikin, D.A.; iner, R.D.; Kohlhaas, K.A.; Kleinhammes, A.; Jia, Y.; Wu, Y.; Nguyen, S.T.; Ruoff, R.S. *Carbon.* **2007**, *45*.
25. Nethravathi, C.; Rajamathi, C, R.; Rajamathi, M.; Gautam, U, K.; Wang, X.; Golberg, D.; Bando, Y. *ACS app. Mat. & Int.* **2013**, *5*, 2708.
26. Nagabhushana, G.; Nagaraju, G.; Chandrappa, G. *J. Mater. Chem. A.* **2013**, *1*, 388.
27. Ng, Y.H; Iwase, A.; Kudo, A.; Amal, R. *J. Phys. Chem.Lett.* **2010**, *1*, 2607.
28. Barbero, N.; Vione, D. *Environmental Science & Technology*, **2016**, *50*, 2130.
29. Shang, M.; Wang, W.; Ren, J.; Sun, S.; Zhang, L. *CrystEngComm*, **2010**, *12*, 1754.
30. Long, M.; Cai, W.; Cai, J.; Zhou, B.; Chai, X .; Wu, Y. *J. Phys.Chem. B.* **2006**, *110*, 20211.
31. Ge, L. *Mater. Chem. & Phys.* **2008**, *107*, 465.
32. Madhusudan, P.; Ran, J.; Zhang, J.; Yu, J.; Liu, G. *App Catal. B-Environ.* **2011**, *110*, 286.

33. Hagfeldt ,A.; Graetzel, M. *Chemical Reviews*. **1995**, *95*, 49.
34. Wang, H.; Zhang, L.; Chen, Z.; Hu, J.; Li, S.; Wang, Z.; Liu, J.; Wang, X. *Chem. Soc. Rev.* **2014**, *43*, 5234.
35. Yuanhua, S.; Zhenhuan, Z.; Jian, T.; Pin, H.; Huaidong, J.; Hong, L. *Small*. **2014**, *10*, 3775.
36. Gao, W.; Wang, M.; Ran, C.; Li, L. *Chem, Commun.* **2015**, *51*, 1709.
37. Xiao, F,W.; Miao, J.; Liu, B. *J. Am. Chem. Soc.* **2014**, *136*, 4.
38. Ning, F.; Shao, M.; Xu, S.; Fu, Y.; Zhang, R.; Wei, M.; Evans, D, G.; Duan, X. *En. & Environ. Sci.* **2016**, *9*, 2633.
39. Xiaoqiang, A.; Kimfung, L.; Junwang, T. *ChemSusChem*. **2014**, *7*, 1086.
40. Wang, Y.; Wang, W.; Mao, H.; Lu, Y.; Lu, J.; Huang, J.; Ye, Z. Lu, B. *ACS App.Mater. & Inter.* **2014**, *6*, 12698.
41. Wang, T.; Li, C.; Ji, J.; Wei, Y.; Zhang, P.; Wang, S.; Fan, X. Gong, J. *ACS Sus. Chem. & En.* **2014**, *2*, 2253
42. Luo, W.; Yang, Z.; Li, Z.; Zhang, J.; Liu, J.; Zhao, Z.; Wang, Z.; Yan, S.; Yu, T. Zou, Z. *En. & Environ. Sci.* **2011**, *4*, 4046.
43. Ye, K, H.; Yu, X,.; Qiu, Z.; Zhu, Y.; Lu, X.; Zhang, Y, *RSC. Adv.* **2015**, *5*, 34152.
44. Sang, Y.; Zhao, Z.; Tian, J.; Hao, P.; Jiang, H.; Liu, H.; Claverie, J. P. *Small*. **2014**, *10*, 3775.
45. Tran, P.D.; Batabyal, K. S.; Pramana, S. S.; Barber, J.; Wong, L, H.; Loo, S.C.J. *Nanoscale*, **2012**, *4*.
46. Tong, L.; Qiu, F.; Zeng, T.; Long, J.; Yang, J.; Wang, R.; Zhang, J.; Wang, C.; Sun, T.; Yang, Y. *RSC Adv.* **2017**, *7*, 47999.

Chapter 7

Conclusions and future work

7.1. Conclusions

An introduction and literature review were carried out to study the type of catalysts that were fabricated in research. There were key areas in the field where research has not progressed rapidly, such as enhancing visible light activity, interparticle charge transfer, chemical and structural ability in catalysts for photocatalytic applications.

Firstly, there was a strategy to construct a visible light active photocatalyst using 0D carbon nanostructures on already-successful semiconductors. The aim of the strategy was to synthesis carbon quantum dots (CQDs) and decorate them on 1D TiO₂. TiO₂/CQDs were fabricated by a facile two-step procedure of steam hydration (to form TiO₂) followed by hydrothermal treatment. The main two methods used to test the photocatalytic activity of this catalyst were photodecomposition of dyes and transient photocurrent responses. The increase in photocatalytic activity of TiO₂/CQDs was presumed to be caused by upconversion properties of CQDs. But after only slight increases in photocurrent response in the visible light spectrum, there was no further study on this catalyst.

The thesis then examines the use of 1D carbon nanostructures, which have reported to possess high surface area and have efficient separation efficiency of electron-hole pairs. C-NW/TiO₂ NF/Cu₂O was synthesised by a multi-step process using hydrothermal and subsequent wet chemical synthesis. The photocatalyst was characterised and there were indications of strong interactions between C-NWs and TiO₂ NF/Cu₂O nanocomposite. Furthermore, the integration of C-NWs caused an increase in surface area and absorption, so it may act as an electron anchor by having improved electron mobility and transportation at higher wavelengths. The interparticle charge transfer was examined, and the increase in transient photocurrent of C-NW/TiO₂ NF/Cu₂O compared to TiO₂ NF/Cu₂O suggests the C-NWs have a bigger influence on electron transfer in the nanocomposite. The I-V and chopped I-V curves showed an increase in photocurrent density, which is indicative of high interparticle charge transfer and separation efficiency of C-NWs in C-NW/TiO₂ NF/Cu₂O. Electrochemical impedance spectroscopy (EIS) studies took place and Nyquist plot illustrated C-NW/TiO₂ NF/Cu₂O exhibited the lowest charge transfer resistance due to the

fast transport of charge carriers between C-NWs and the semiconductors. However, the photoelectrochemical stability did not show a distinct difference between C-NW/TiO₂ NF/Cu₂O and TiO₂ NF/Cu₂O so this was something that could be looked at further.

After having some concerns with photostability as photocorrosion is prevalent in some semiconductors such as Cu₂O, the next phase to fabricating low dimensional carbon materials was graphene. Reduced graphene oxide (rGO) has caused extreme interest over the last few years as they have favourable properties, such as high surface area, tuneable band gap and strong electron mobility. Therefore, Chapter 5 explored the photocatalytic activity of Pom-pom Dahlia-like Cu₂O/rGO, which was synthesised by a one-pot facile wet chemical method. The hydrogen evolution rates confirmed the hybridisation of Cu₂O with rGO nanosheets almost doubles the specific activity. The photocatalytic stability of Cu₂O/rGO was explored in five cycles and the photocatalyst was still 85% efficient after 5 hours, compared to only 73% decomposition of 4-CP with Cu₂O after 5 cycles, which indicated that rGO enhanced the catalyst photostability. The photoelectrochemical stability was tested by recording transient photocurrents with chopped illumination every 20 minutes. Cu₂O/rGO had a reduction in photocurrent by 3% on the second illumination cycle and only 5% after an hour of photocurrent responses. This exemplifies the excellent photostability of Cu₂O/rGO.

Some of the ideas in the first chapter were brought back in the final chapter, but now having a lot more knowledge on constructing carbon nanostructures with high charge transfer and photostability. The final chapter examined quantum dot BiVO₄ (instead of CQDs) dispersed on rGO, by a one-pot solution phase approach. TEM images confirmed high dispersion of 2D graphene sheets. The hydrogen evolution rate of QD-BiVO₄/rGO was over 300 times higher than BiVO₄. rGO was suspected to act as electron acceptors and mediators, which can trap photoinduced electrons to enhance visible light activity on the catalyst surface. This time bisphenol A was used as the model pollutant. The enhanced photocatalytic oxidation of QD-BiVO₄/rGO compared to BiVO₄ and QD-BiVO₄ is attributed to the driving force of electron transport between the rGO support and highly dispersed quantum dot BiVO₄. The photocatalytic stability of BiVO₄/rGO was tested by decomposing methylene blue (MB) dye for 5 continuous cycles (one hour per cycle), and only decreased 7% in decomposition efficiency after 450 minutes. In contrast, BiVO₄ had a significantly lower efficiency to degrade MB dye (62%) after the 5 cycles. The stability of rGO is attributed to the large surface area and high dispersion of QD-BiVO₄ on the

graphene layer. The photoelectrochemical stability of QD-BiVO₄/rGO was excellent with a slight reduction in photoresponse in the second and third illumination cycle, by 0.1 μ A and 0.16 μ A respectively compared to the loss of 0.29 μ A and 0.44 μ A using bare BiVO₄.

7.2. Future work

The main objectives of the thesis were achieved by fabricating various low dimensional carbon nanostructures and enhancing semiconductors. Nevertheless, the manufactured catalysts are novel so there will always be aspects of research to improve on.

Chapter 3 detailed an attempt to construct a visible light active photocatalyst using carbon quantum dots (CQDs) and 1D TiO₂ NF. However, the lack of improved visible light activity with the integration of CQDs in the photodecomposition of pollutants and photocurrent responses as well as the UV-Vis spectra showing minimal absorbance above 435 nm provided enough evidence to stop studying the photocatalyst. Therefore, it is necessary to go back to empirical research of carbon quantum dots and further investigate the photoluminescence of the fabricated catalyst.

In Chapter 4, a detailed photoelectrochemical study took place to analyse the interparticle charge transfer of C-NW/TiO₂ NF/Cu₂O. However, more characterisation studies are needed to understand the photophysical properties of the catalyst, such as x-ray photoelectron spectroscopy (XPS). Furthermore, an important part of learning more about the photocatalyst would be to examine the photocatalytic activity of C-NW/TiO₂ NF/Cu₂O by hydrogen evolution reactions and photodecomposition of a model pollutant. In addition, the photoelectrochemical stability experiments showed the catalyst was not very stable so it would be wise to study other methods of treating semiconductors to increase stability.

Chapter 5 and 6 successfully illustrated the increase in chemical and structural stability with the addition of 2D rGO in photocatalytic applications. However, rGO is not only used in photocatalysis, but its unique properties have caused interested in energy storage devices, sensors, electronics and even nanomedicine. Therefore, it would be interesting to see if the same catalyst can be effective in other applications, such as lithium ion batteries, supercapacitors, biosensors in biomedicine and in antibacterial activity.